

# Chapter 5

## Sample Delivery Techniques for Serial Crystallography



Raymond G. Sierra, Uwe Weierstall, Dominik Oberthuer,  
Michihiro Sugahara, Eriko Nango, So Iwata, and Alke Meents

### 5.1 Overview

In serial femtosecond crystallography (SFX), protein microcrystals and nanocrystals are introduced into the focus of an X-ray free electron laser (FEL) beam, ideally, one-by-one in a serial fashion. The high photon density in each pulse is the double-edged sword that necessitates the serial nature of the experiments. The high photon count focused spatially and temporally leads to a *diffraction-before-destruction* snapshot, but this single snapshot is not enough for a high-resolution three-dimensional structural reconstruction. To recover the structure, more snapshots are required to sample all of reciprocal space from randomly oriented crystal diffraction, and in practice, some redundancy is necessary in these measurements. Please see Chap. 8 for more details.

---

R. G. Sierra (✉)

Hard X-Ray Department, LCLS, SLAC National Accelerator Laboratory, Menlo Park, CA, USA  
e-mail: [rsierra@slac.stanford.edu](mailto:rsierra@slac.stanford.edu)

U. Weierstall (✉)

Department of Physics, Arizona State University, Tempe, AZ, USA  
e-mail: [weier@asu.edu](mailto:weier@asu.edu)

D. Oberthuer · A. Meents

Center for Free-Electron Laser Science, German Electron Synchrotron DESY, Hamburg, Germany  
e-mail: [dominik.oberthuer@desy.de](mailto:dominik.oberthuer@desy.de); [Alke.Meents@desy.de](mailto:Alke.Meents@desy.de)

M. Sugahara · E. Nango · S. Iwata

RIKEN SPring-8 Center, Sayo-gun, Hyogo, Japan

Department of Cell Biology, Graduate School of Medicine, Kyoto University, Sakyo-ku, Kyoto, Japan

e-mail: [msuga@spring8.or.jp](mailto:msuga@spring8.or.jp); [nango@spring8.or.jp](mailto:nango@spring8.or.jp); [s.iwata@spring8.or.jp](mailto:s.iwata@spring8.or.jp)

Fixed targets were initially used to verify the *diffract-before-destruction* idea central to biological imaging with X-ray FELs and specifically serial femtosecond crystallography (SFX) experiments [1]. In most traditional optical imaging experiments, the sample is mounted onto a glass slide, goniometer pin, electron microscopy grid, or some other substrate; therefore, fixed targets seem a logical first step for X-ray FEL sample delivery. However, the repetition rate of the FEL pulses combined with their destructive power made the efficient use of fixed targets difficult. At the time of the first X-ray FEL experiments, fixed targets could neither be replenished at the X-ray repetition rate nor could they be properly protected from the adverse effects of the vacuum environment without drastically increasing background scattering. This drove the desire and need to use flowing liquid sample delivery methods. Later in the chapter, the idea of fixed targets for in-vacuum and ambient experiments is revisited.

Biological samples, which are by nature sensitive to damage by X-rays, should be replenished, at the minimum, with the X-ray FEL repetition rate, which has, until recently, ranged up to 120 Hz at X-ray facilities that have operated for a few years. If synchronized with a 120 Hz source, every sample, most commonly a crystal of a particular biological molecule, that is hit by a focused X-ray pulse is destroyed after the pulse has passed through; within 8.3 ms the debris must be cleared out and a new crystal is ideally supplied for the next pulse. With the advent of superconducting accelerators, an average repetition rate of 27 kHz (4.5 MHz peak) and up to 1 MHz will be available with the opening of the European XFEL and the LCLS-II upgrade, respectively. To make use of the peak repetition rates at these facilities, samples must be replaced every 220 ns or 1  $\mu$ s, respectively. Figures 5.1 and 5.2 show the effects of the intense incident X-ray pulses on a solid substrate and a liquid water jet in vacuum.

The first structural biology experiments at an X-ray FEL were performed at soft X-ray energies [3, 4]. At these lower energies ( $<2$  keV), X-rays interact more strongly with electrons than at the higher energies typical for X-ray crystallography ( $>6$  keV). Due to the low photon energy, the first experiments were performed

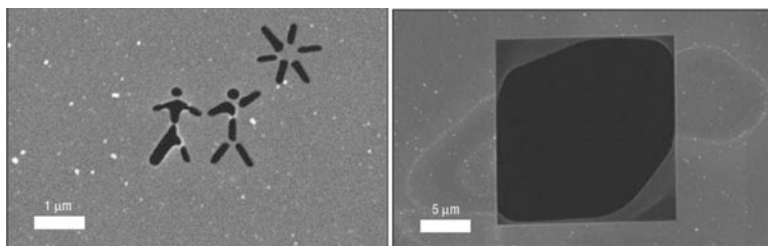


**Fig. 5.1** SEM images of a pattern etched with a focused ion beam into a 20 nm silicon nitride membrane, before (*left*) and after (*right*) of an incident FEL pulse. The damage is evident, yet the authors were able to reconstruct the original structure, thus verifying the *diffraction-before-destruction* concept. The right image demonstrates the destructive power of the incident X-rays which affect the interaction region (central 20  $\mu$ m) as well as the adjacent area [1]. Reproduced with permission from Chapman et al. [1]

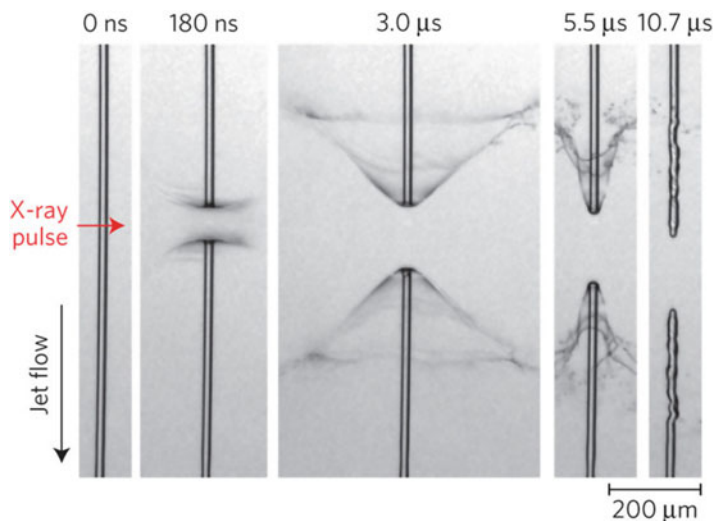


**Fig. 5.2** A Rayleigh jet of water (20- $\mu\text{m}$ -diameter) injected into vacuum, imaged stroboscopically, to view the effects of the incident X-ray FEL pulse on the stream of liquid. Varying time delays after the incident X-ray pulses ( $0.75 \pm 0.08$  mJ, 8.2 keV, 120 Hz) are shown. A gap forms after the X-ray pulse vaporizes the liquid explosively. Liquid from the jet forms thin conical films of water, which later collapse onto the jet, while the liquid continues to flow (downwards in the image). Reproduced with permission from Stan et al. [2]

in vacuum to prevent strong interactions between ambient gas molecules and soft X-rays. Additionally, the samples had to consist of nanometer sized crystals or single particles to prevent excessive X-rays absorption by the sample. The hydration layer around the sample had to be small, to minimize absorption from surrounding water molecules, and to minimize background scatter in the case of single particles.

Flowing liquid delivery systems were thought to be able to both sufficiently replenish the samples and keep them protected in vacuum. For single particles (e.g., viruses, whole cells), Seibert et al. [4] used an aerodynamic lens stack, similar to that shown in Fig. 5.3, in which an aerosolized sample passes through a series of chambers at decreasing pressure, separated by apertures. The pressure gradient from atmosphere to vacuum through each section acts as a focusing lens. As the aerosolized particles accelerate with the gas passing through the focusing apertures, the particles' inertia keeps them closer to the centerline while the carrier gas quickly expands, creating a focused particle beam, while simultaneously evaporating a volatile solvent. Ultimately, the particles arrive at the X-ray interaction region with minimized hydration shell, ensuring low background scattering critical to imaging single particles while still protecting the particle from the detrimental effects of vacuum. Transmission inefficiencies and low particle densities at the interaction region make the aerodynamic lens less than ideal [for SFX experiments], and aerosol injection for single particle imaging experiments is still an area of ongoing research [6–8].

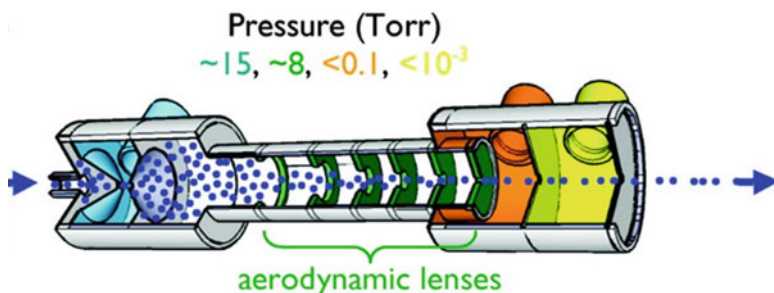


**Fig. 5.3** Cross-sectional schematic of an aerodynamic lens stack. Aerosolized particles are generated (*left*) from an electro spray, for example (*not shown*), and focused through an aerodynamic lens stack towards the interaction region (to the right). Differential pumping regions are serially decreasing in pressure from left to right towards the interaction region, [with typical pressure values corresponding to the colored chambers]. Modified with permission from Bogan et al. [5]

For crystallographic applications, an increased water layer around the sample is more tolerable due to the increased scattering intensity at the Bragg peak locations. Therefore, liquid sample delivery directly into the beam is more commonly used. The most familiar liquid jet is a Rayleigh jet. Seen in faucets, garden hoses and fountains, a Rayleigh jet is formed when there is sufficient flow rate to overcome the resistive properties intrinsic in a fluid, such as its viscosity and/or surface tension. Rayleigh was able to describe the eventual breakup of the jet into droplets from small surface perturbations [9, 10]. Faubel et al. [11] and later, for the purpose of SFX, Weierstall et al. [12] demonstrated that liquid streams could be created and delivered into vacuum. Rayleigh jets use large quantities of sample, on the order of 100–1000s of  $\mu\text{L}/\text{min}$ . Small jet diameters with reduced flow rate and improved stability compared to Rayleigh jets were made possible by the gas dynamic virtual nozzle (GDVN) [13]. In the next section, the fluid mechanics that governs liquid injection devices is introduced and discussed. These concepts set up the boundary conditions of sample delivery for SFX and allow the reader to appreciate the nuances of the subsequent, seemingly similar, sample delivery methods.

SFX takes advantage of some of the unique capabilities of X-ray FELs by keeping protein crystals in a solvated state and close to room temperature. The crystal concentration should ideally be adjusted so that, on average, only one crystal is in the interaction region during a given X-ray pulse. For a 1–10  $\mu\text{m}$  X-ray focus, typical concentrations are  $10^7$ – $10^{10}$  particles per milliliter and are optimized during the experiment.

The requirements for SFX sample delivery are therefore:

- Replenish the protein crystals at the X-ray interaction region as efficiently as possible
- The delivery method should be compatible with the experimental environment (e.g., vacuum, helium, air)

- No sample damage due to the injection process (compatible carrier media/support and sample, no undue shear forces, charging, etc.)
- Minimal background scattering from the carrier media or support
- Reliable operation for hours

Sample delivery for SFX experiments can be nuanced and complicated for crystallographers looking to perform an experiment for the first—or  $n$ -th time. The following section will serve as a primer of the underlying fluid mechanics that govern sample delivery. The problem of delivering a slurry of crystals to the incident X-ray beam in the most efficient way is not trivial and is at the crux of a successful experiment. It can be the difference between hours of frustrating, fruitless data collection and a successful experiment. By the end of this chapter, the reader should have an appreciation for the status quo of the numerous sample delivery techniques available to interface with the myriad crystallization conditions possible, while being able to identify the pros and cons of each technique and how a specific sample delivery approach might mate with their particular crystal system.

In this chapter, several different methods are presented which have been used to deliver microcrystals to an X-ray FEL beam. In Sect. 5.2 the gas dynamic virtual nozzle (GDVN) is introduced, which has been the workhorse for many SFX experiments since the start of user operations at the first hard X-ray FEL. These are, historically, handmade nozzles which help minimize clogging by the crystal solution or foreign objects, since they produce a micron sized jet ( $<10\ \mu\text{m}$ ) from a larger aperture; passing the same crystal slurry through a micron sized orifice is quite impractical due to clogging issues. To make them more reproducibly, high-resolution 3D printing is currently being employed and first results are shown. GDVNs have a relatively high flow rate and jet speed, which leads to considerable sample waste when used at low repetition rate X-ray FELs such as the Linac Coherent Light Source (LCLS) and the SPring8 Angstrom Compact free electron LASER (SACLA). High viscosity injectors, such as the lipidic cubic phase (LCP) injector, which were initially developed due to their compatibility with membrane protein crystal growth, and later were adapted for multiple sample types to reduced sample waste, are introduced in Sect. 5.3. These allow a reduction of the sample flow rate by a factor of 100 as long as the media has a high viscosity similar to LCP, a high viscosity growth medium for many membrane proteins. In Sect. 5.4 the microfluidic electrokinetic sample holder (MESH) and its variant, the concentric MESH (coMESH), is introduced, which borrows methods from electrospray and electrospinning to move the sample in a charged stream through the X-ray focus. Sample flow rates with this technique are lower than with the GDVN and can be as low as with the high viscosity injectors, therefore filling the gap between these two techniques in terms of sample consumption.

Section 5.4 introduces two variants of the GDVN, double flow focusing nozzles and mixing nozzles. Mixing nozzles are currently of great interest when studying enzyme reactions in a time-resolved fashion. Double flow focusing nozzles are more reliable than regular GDVNs since clogging events are largely avoided due to the use of an outer focusing liquid and they also allow a reduction of the

sample consumption, since the sample flow can be pinched off by the outer liquid flow. Section 5.5 introduces other viscous carrier media that can be used for SFX with the high viscosity injector. In addition, it presents a drop-on-demand system synchronized with the X-ray FEL pulses for SFX, which has been developed at SACLA. The in-helium atmosphere at SACLA has different considerations for sample delivery as compared to the in-vacuum techniques initially developed to interface with LCLS. An example of a fixed target sample holder is presented in Sect. 5.7. With fixed target sample holders, thousands of microcrystals are mounted on a solid support and scanned through the X-ray beam. One microcrystal is exposed to an X-ray pulse, then the support is moved to the next crystal. The sample support has to be moved from crystal to crystal at the repetition rate of the X-ray laser. Fixed target sample delivery results in very high hit fractions since ideally every X-ray pulse hits a crystal. The chapter closes with an outlook on what is next in the field of sample delivery as mixing experiments and high repetition rate sources start to become the new norm for SFX.

### 5.1.1 *Fluid Mechanics for Crystallographers*

Any crystallographer knows the delicate balance needed between the protein and its surrounding *mother liquor*—the fluid composition that coaxes the protein out of solution and into a crystalline lattice. Finding the right conditions for crystals to grow can take years, and even optimizing them for cryo-conditions or improved resolution can take a whole career. By the end of this chapter you will appreciate that it is ultimately the protein crystals and their mother liquor that govern the performance, and thus success, of an SFX experiment using liquid sample delivery. The fluid properties of the mother liquor alone can vary from low surface tension detergents to high viscosity polymers and lipids or simple salt and water brines, and these differences can be felt as early as during pipetting in the lab. The addition of suspended protein crystals increases the apparent viscosity and introduces complexities to the experiment, such as potentially disrupting any meniscus exposed from a capillary opening, causing clogs at junctions and throughout liquid lines when transporting the sample through liquid lines, and sedimentation in reservoirs. If performing the experiment in vacuum, the evaporation of the exposed meniscus modifies the local chemistry and can cause precipitation of salts and dehydration of the sample and severely impede the experiment; the chemicals that cause your proteins to precipitate into crystals can also cause salts to precipitate once exposed to vacuum, for example. The following section will give a brief overview of some fundamental fluid mechanics that govern the different sample delivery methods and setup the physical constraints which might answer the crystallographers first question when [planning for sample delivery] for an SFX experiment: “Why do we have to do that?” A successful SFX crystallographer will be familiar with these concepts and work closely with the sample injection team to get the crystals through one of the major SFX bottlenecks.

To understand the constraints of sample injection, and thus the need for different sample delivery techniques, pressure-driven fluid flow in a pipe should be understood; more simply the Hagen–Poiseuille [14] flow equation:

$$Q = \frac{\pi \Delta P r^4}{8\mu L} = \frac{\Delta P}{R} \quad (5.1)$$

where the flow rate  $Q$ , of a fluid with dynamic viscosity  $\mu$ , is driven by a pressure gradient  $\Delta P$ , over a length of tubing  $L$ , with radius  $r$ . The dynamic viscosity (or simply viscosity) here, in SI units of Pa·s, is indicative of the fluid's resistance to shear stresses. This is the parameter we intuit when we say that honey is *thicker* than water; that is, honey has a higher dynamic viscosity than water. The dynamic viscosity is different from the kinematic viscosity,  $\nu = \mu/\rho$ , with SI units of m<sup>2</sup>/s. The kinematic viscosity represents the ratio of the fluid's viscous force to the inertial force and indicates how fast momentum is diffused throughout the fluid. For example, the viscosity of air and water at standard atmospheric conditions are approximately 0.02 and 1 mPa·s respectively, which agrees with our expectation that water is *thicker* than air. The kinematic viscosities, however, are  $1 \times 10^{-5}$  m<sup>2</sup>/s and  $1 \times 10^{-6}$  m<sup>2</sup>/s, respectively, implying that momentum diffuses through air faster than in water. The kinematic viscosity is important when discussing velocity profiles within the fluid, as well as mass diffusion. An ion of hydrogen has a diffusivity of  $10^{-10}$ – $10^{-9}$  m<sup>2</sup>/s in water, meaning that momentum information of the bulk water diffuses 3–4 orders of magnitude faster than the mass diffusion of hydrogen ions; for example, the parabolic velocity profile of flowing water in a pipe is established sooner than a uniform pH.

A fluid deforms continuously as a shear stress is applied to it, whereas a solid object resists this applied force. Both liquids and gases are fluids and can exhibit similar behaviors. Most of the basic fluid mechanics concepts discussed here will assume Newtonian fluids. A Newtonian fluid, such as water and oil, is one whose viscosity is a property of the fluid's state and is not affected by the applied shear rate. In contrast, toothpaste, ketchup, blood, polymer solutions, or colloidal suspensions like mayonnaise and paint, are non-Newtonian fluids. Here an increased shear rate can cause the fluid to move easier or more difficultly depending on the specific flow properties of the fluid. It is likely that certain protein crystallization conditions might lead to fluids which exhibit these complex behaviors, but the basic principles discussed here will focus on a Newtonian fluid assumption. In later sections some injection methods will be discussed where non-Newtonian viscous media, such as lipidic cubic phase of monoolein (LCP), agarose, or high molecular polymer solutions, are used as carrier media for sample delivery. See White [14] or other fluid mechanics texts for more details on shear thinning, shear thickening, Bingham plastic, or thixotropic fluids.

The fluid properties of a crystal's mother liquor might dictate the viscosity and thus cannot be readily changed. Under many circumstances, the size of the protein crystals itself begins to limit the geometries suitable for the SFX experiment. In most fluid mechanics calculations applicable to SFX, the fluid is treated as a continuum

and species inside of the fluid are treated as dilute, solvated species, not causing changes in the bulk properties of the fluid. This assumption cannot be maintained when dealing with a suspension of solid protein crystals on the order of 100s of nanometers to dozens of micrometers in dimension. The crystals themselves have solvent channels that can interact with the fluid but this is beyond the scope of this discussion. The idea should be clear, though, that a crystal slurry and the same fluid without crystals will invariably behave differently, whether it be different effective viscosities, or non-Newtonian behaviors, much like the way particles suspended in water prevent ketchup from moving until a sufficiently high shear rate is applied.

Although not always physically accurate, a useful heuristic in understanding basic fluid flows is to use an electric circuitry analogy. The terms in the pipe flow equation above can be grouped to define a hydrodynamic resistance  $R$ . Much like an element in an electronic circuit has some resistance to the flow of current from an applied voltage (Ohm's law), a capillary of fluid will restrict volumetric flow with the application of a volumetric potential (i.e., the pressure ( $\Delta P$ )). Ignoring the effects of evaporative cooling possible at a vacuum orifice, if water is placed inside a 50  $\mu\text{m}$  inner diameter capillary tube, 1 m in length, with atmospheric pressure applied to one end and vacuum applied to the other, the water will flow at approximately 1  $\mu\text{L}/\text{min}$ . This fluid flow is so low that the ensuing fluid meniscus on the vacuum side will freeze due to evaporative cooling in vacuum. Changing the fluid's properties or driving the flow much faster (creating a Rayleigh jet), would be the only way to prevent that meniscus from freezing. However, the high flow rate of a Rayleigh jet ( $>100 \mu\text{L}/\text{min}$ ) can be prohibitive for most protein crystal slurries. The Hagen–Poiseuille equation indicates that the only ways to reduce the sample consumption through the capillary tube are to decrease the pressure difference, increase the length of the tube, decrease the tube diameter, or to increase the viscosity. We will briefly discuss the implications of a change in these parameters.

*Pressure Gradient* Although serial crystallography experiments do not necessarily require in-vacuum injection, many have been and continue to be done in vacuum. In the case of vacuum injection, a way to reduce the pressure gradient below one atmosphere is to apply vacuum upstream of the sample reservoir. This can lead to outgassing of the solution in the capillary, which can lead to cavitation and bubble formation and can severely limit or interrupt the jetting ability, and thus the data collection. This might also affect the stability of the suspended protein crystals as the solution chemistry is potentially affected through dehydration. At the vacuum end, differential pumping schemes can be employed to keep the exposed meniscus nearer to atmospheric pressures, thus diminishing the pressure gradient. In non-vacuum experiments, the pressure gradient is arbitrary and bounded by the injection method rather than the vacuum conditions.

*Tubing Inner Diameter* One of the most powerful relationships for fluid flow in a pipe is the fourth-power dependence on the inner diameter of the tube. Going from a 50- $\mu\text{m}$  diameter tube to a 100- $\mu\text{m}$  tube can give a 16-fold increase in flow rate or a 16-fold decrease in pressure to run the same flow rate. In practice, to maintain the same liquid jet, the pressure will stay and the flow rate will have to compensate. A

gross simplification of the process of ejecting liquid streams from a liquid's surface would be to imagine that sufficient kinetic energy must be imparted onto the fluid by some sort of potential energy well, be it pneumatic, hydraulic, electrostatic, or other. Once the applied potential energy is enough to fight resistive forces in the bulk fluid and the exposed meniscus, mainly the viscosity and surface tension, then the remaining energy is used to flow the jet. In order to further focus the meniscus of the fluid into a small stream, one must add some excess kinetic energy to the system [to accelerate the flow], and herein lies one of the fundamental challenges to sample delivery. The atmosphere pressure difference, in our hypothetical system above, dictates a minimum flow rate of  $1 \mu\text{L}/\text{min}$ , as most SFX experiments have historically occurred within a vacuum. Adding energy might increase this flow rate, as seen with either the GDVN, where flow rates on the order of tens of microliters per minute are necessary to make a thin stable jet, or the thicker Rayleigh jet with hundreds of microliters per minute. See Eggers and Villermaux's review on the physics of liquid jets for more details [15].

As appealing as it seems to then reduce the capillary diameter, modifications to the tubing diameter quickly come at odds with the necessary driving pressure. For example, to run at  $10 \mu\text{L}/\text{min}$  (similar to flows of a nominal GDVN) through a 1 m-long capillary with an inner diameter of  $25 \mu\text{m}$ , a driving pressure of over 2500 psi ( $\sim 170$  bar) is needed, as opposed to 160 psi ( $\sim 11$  bar) needed for the same flow rate through a  $50 \mu\text{m}$  inner diameter capillary with the same length. These values assume the capillary meniscus is in air and does not take into account whether the flow creates a liquid jet or not. The pressure values would likely change if modified to create a jet, however, the relative pressure differential between the two capillary diameters will remain. Such a large operating pressure approaches safety limits of common fluid handling and microfluidic equipment and might cause failures, and although not prohibitive, this quickly becomes non-ideal.

The smaller the tubing diameter gets, the easier it can clog with the protein slurries as well as any foreign particulates. A general heuristic is that the largest crystal dimension should not exceed  $2/5$  of the inner diameter of the tubing. The more concentrated the crystal slurry gets, the higher the likelihood that even small nanocrystals can clog a  $50 \mu\text{m}$  opening. A macroscopic analogy would be a crowd of people exiting a doorway. Although one person fits easily through the doorway, moving many people through quickly can cause "clogging." Unfortunately, capillary diameters are not a readily tunable parameter for sample delivery, even though a narrow range of sizes are typically employed: 30, 40, 50, 75, and  $100 \mu\text{m}$  inner diameters have been used with varying success depending on the size of the suspended crystals. Increasing the diameter to accommodate for larger crystals or to prevent clogging will quickly lead to exponentially higher sample consumption rates.

*Tube Length* The experimental geometry can quickly become complicated with vacuum chambers as large as 1 m wide to support the necessary equipment to execute the experiment. This results in capillary lengths on the order of 1 m in order to have the sample injector close to the interaction region while reaching relevant sample injection equipment outside of the vacuum chamber. Making the capillaries longer is not as problematic; however, increases in length cause increases

in the necessary driving pressure. Keep in mind that minor modifications in tubing diameters can give similar results to increases in tubing length; for example, going from 100 to 50  $\mu\text{m}$  inner diameter has the same effect on the necessary pressure as increasing the larger tube's length from 1 to 16 m.

*Viscosity* The mother liquor's viscosity can be one of the most important differentiators between applicable SFX jet techniques. Of the four parameters outlined to diminish the flow rate, it is the only one intrinsic to the system, while the others are externally applied parameters. The viscosity of a protein crystal slurry is not readily modified due to the effects that a change in electrochemistry might have on the quality of the crystals. Modifications of the viscosity—if possible—can lead to reductions in sample consumption. The viscosity of a solution can be quickly increased by simply adding long polymer chains of large molecular weight and glycerol [16, 17].

As previously outlined, the viscosity of the fluid is one of the key parameters that capture how a fluid will resist the transfer of momentum required to make a liquid jet. As the viscosity of a fluid is increased by either dissolving additives or suspending high-density particulates, there is a need to supply more potential energy (e.g., pressure) to overcome the added resistance and drive the flow. Einstein theorized [18] and Hiemenz [14] and references therein later verified experimentally, that the viscosity of a *dilute* solution will increase by  $1 + 2.5\phi$ , where  $\phi$  is the volume fraction of the suspended particles (no greater than 0.02). These are empirical approximations and have since been further modeled. Probst [19] notes that volume fractions as high as 0.1 have been used in the past. For reference, Fig. 5.4b) shows typical volume fractions of protein crystals, which are generally around 0.2 but can be higher [20]. Assuming the largest volume fraction in the dilute assumption ( $\phi = 0.1$ ) the viscosity increases 25% thus affecting the flow conditions accordingly.

As an example, running a typical 50  $\mu\text{m}$  inner diameter GDVN with water will give typically a minimum flow rate of 3–4  $\mu\text{L}/\text{min}$  with a driving pressure of approximately 400 psi. Running a suspension of lysozyme crystals (similar to those in Fig. 5.4 with >10% volume fraction), with mother liquor of water, salt, and acetic acid through the same nozzle, causes the minimum flow rates to increase by dozens of microliters per minute and causes the driving pressure to increase as well. This increase is much more than the 25% increase we previously approximated from the dilute suspension assumption (<10% volume fraction). The slurry's properties create different conditions at the meniscus and in the bulk fluid, resulting in higher driving pressures to overcome the resistance from the small solid crystal chunks, which periodically pass through the capillary and meniscus. The resulting liquid jet length is now significantly shorter before breaking up. The driving pressure can increase by no more than fivefold, as many of the fittings and tubings might fail past 2000 psi. This implies that a standard 50- $\mu\text{m}$  inner diameter GDVN is well suited for injection of liquids with viscosity similar to water, but might struggle as soon as viscous additives and high concentrations of crystals are added.

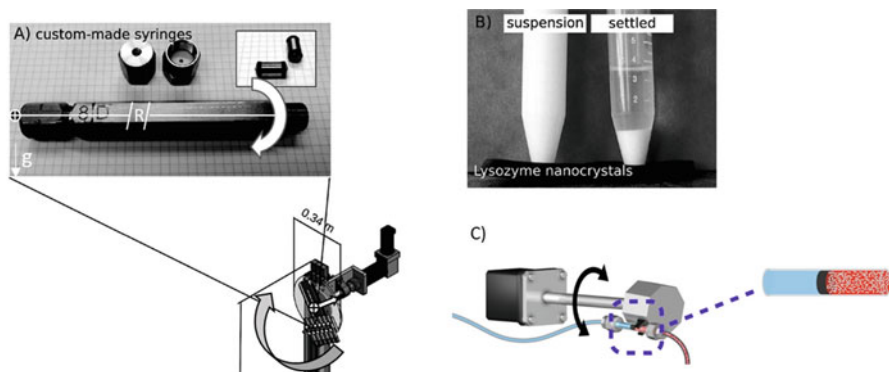


**Fig. 5.4** Custom-made syringes (a) mounted on an anti-settling device near the sample chamber. The gravity vector,  $g$ , points down in all images; the syringe oscillates about a fixed radius of rotation,  $R$ , about the central black and white cross  $0.17\text{ m}$  away (not to scale). The centerline of the syringe is parallel to the radial vector (perpendicular to the axis of rotation). Reproduced with permission of the International Union of Crystallography [20]. Lysozyme crystals in high concentration (b). The crystals on the left were resuspended just before the picture was taken, while those on the right were allowed to settle (minutes to hours); Reproduced with permission from Lomb et al. [20]. An alternative anti-settling device (c), where the centerline of the syringe is perpendicular to the radial vector (parallel to the axis of rotation). From the anti-settling device, the sample is brought into the interaction region, in vacuum, by means of a liquid jet; Reproduced with permission from Sierra et al. [21]

High pressure steel fittings (withstanding up to  $10,000\text{ psi}$ ) are common commercially; however, throughout many of the injection schemes we will discuss, fused silica capillaries are common, which interface with polymer fittings and polymer tubing sleeves, which might not withstand the high pressures. Also, common pressurized gas cylinders only go up to  $\sim 2000\text{ psi}$  meaning that HPLC pumps running at constant flow are the only option to drive the flow. The issue of high pressure is not insurmountable; it just requires additional design restrictions that might not be tolerable in some cases. The section on high viscosity extrusions shows how a pressure amplifier can achieve these high pressures to extrude viscous media through small fused silica capillaries. Although Johansson et al. [22] showed that more viscous media, such as lipidic sponge phase, can pass through a GDVN, this has proven quite difficult to reproduce. Therefore the GDVN can be used with lower water-like viscosities, and the High Viscosity Extrusion (HVE) method can handle higher viscosities, leaving a wide range of viscosities in between. (The MESH and double flow focusing nozzle (DFFN) sections will address this.)

An added complication with gas focused jets and viscosity is that the boundary condition necessary to focus the liquid meniscus with the gas sheath must have matching shear rates, a condition dependent on each fluid's viscosity. The more viscous the liquid meniscus, the higher shear rate the gas must apply, again running into an upper limit of applicable gas pressure values. A normal GDVN gas sheath mass flow rate is  $20\text{ mg/min}$  which requires a gas pressure of about  $400\text{ psi}$  when

using a 2 m long gas tubing with 100  $\mu\text{m}$  inner diameter. A 5–6 times increase is tolerable (assuming a full gas cylinder of  $\sim 2500$  psig), with a higher probability of some connection failure happening before that point. The increased gas load on the vacuum chamber from the helium sheath gas might present issues for the turbo pumps or sensitive electronic equipment. This helps explain why more viscous substances will have difficulty injecting through a GDVN nozzle and why the helium sheath gas in a HVE does not focus the media and simply helps straighten the extruded media and prevent the sample from curling upon itself and the nozzle. Note that recently, a concentric flow GDVN, the dual flow focusing nozzle (DFFN) injector, was developed as a way to handle different media through a gas focused injector by focusing an intermediate fluid, such as ethanol, which in turn focuses the central fluid containing the sample [23] (as well as Sect. 5.5). A useful metric is to calculate the hydrodynamic resistance of the system,  $R$ , as defined in Eq. (5.1) in order to determine the liquid injection method best suited for a given sample. Estimate your system's resistance and compare it to a published injection methods estimated resistance and see if your system might be compatible.

One important restriction made on the geometry by the crystals is a minimum inner diameter to accommodate the protein crystal dimensions. The 2/5 approximation seems to hold for crystals with morphologies of low aspect ratios, such as cubes, blocks, diamond, etc. as evidenced by a 20  $\mu\text{m}$  filter being used on 50  $\mu\text{m}$  inner diameter GDVN geometries. High aspect ratio crystals might not obey this approximation, since the long dimension might flow align and not cause the same concern. However, this should be tested prior to the experiment to ensure there are no issues of clogging. Of course, smaller, uniform crystal sizes are better for sample injection in all sample delivery methods and lead to injection more similar to flow conditions without suspended crystals. Unfortunately, crystal size and uniformity are not always controllable parameters.

### 5.1.1.1 Suspended Solids

Much of the work used to describe fluid flows typically considers the bulk flow with the properties of the fluid being a continuum. Typically dissolved salts and other soluble objects are assumed dilute enough to not disturb the continuum characteristics of the properties [19]. In the case of sample injection for SFX, it is inherently a two-phase flow, with solid crystals subject to the continuous fluid they are suspended in. The best crystalline suspension is one that is uniform in size and monodisperse, making the fluid behavior less erratic due to variations in size, as well as aiding in the X-ray data collection.

The Reynolds number ( $Re$ ) is an important dimensionless parameter in fluid mechanics. It represents the ratio of inertial forces to viscous forces in the media. It is calculated as  $Re = \rho UD/\mu$  where the mass density  $\rho$ , the characteristic bulk velocity  $U$ , the characteristic length  $D$ , and dynamic viscosity  $\mu$ , are properties of the fluid and the relevant physical parameters. To describe flow through a tube, the characteristic length that dictates the flow phenomena is the wetted diameter;

flow over a flat plate would have the length of the plate as the characteristic length; flow around a small object suspended in a semi-infinite fluid would have the largest particle dimension as its characteristic length. Fluid flows in tubes with Reynolds numbers less than 2300 empirically move in laminar sheets and lack any turbulent effects [19] (and references therein). In the case of small particles suspended in solutions, they are typically at  $Re < 1$  and are in a regime called *creep* (or Stoke's) flow, where inertial forces are completely negligible and viscous or other forces might dominate. In this flow regime, particles can readily sediment, and they will sediment at different rates, based on their morphology, size, and their alignment with the gravitational field [14]. A particle in a parabolic flow field, typical in fully developed pipe flow, will stay on a streamline unless it diffuses out due to Brownian motion (Taylor dispersion) or some external force, such as gravity [14, 19, 24]. For reference, water flowing at 10 mm/s through a 50  $\mu\text{m}$  orifice has  $Re = 0.5$  ( $Q$ , the volumetric flow rate  $\sim 2 \mu\text{L}/\text{min}$ ); slower flows and more viscous flows will have even lower  $Re$  values. Unlike inertially dominated flows, two bodies suspended in creep flow can affect each other's flow fields significantly; for example, two identical particles 5 diameter-lengths apart can still feel the others' presence, whereas inertially dominated flows around a particle would return to the bulk velocity at such distances. Creep flow fields never have an increase in velocity as opposed to inertial flow fields, meaning nearby objects slow each other down; for example, objects sedimenting in creep flow near a wall settle more slowly than those away from the wall.

*Unions and Filters* High viscosity and MESH injectors typically have no more than one union connecting the capillary tip at the interaction region to the sample reservoir. GDVN and DFFN injections more commonly use tubing unions. Unions rarely connect two tubings of the same inner diameter; rather it is most common to go from larger inner diameters and interface down to smaller inner diameters, such as the final size in the liquid injector. Even when connecting two of the same capillaries, the union itself has an inner diameter which might not match (e.g., common tubing unions have a 250 or 500  $\mu\text{m}$  inner diameter, connecting two capillaries of 50  $\mu\text{m}$  inner diameters will go from the original capillary dimension to one 5–10 times larger, and back down to the original dimension). The crystals flowing near the periphery of the larger diameter tube cannot easily cross streamlines to get into the next smaller inner diameter line, thus causing a buildup at the union interface, which quickly culminates into clogging. Taneda showed how streamlines around a corner in low Reynolds number flow can create a vortex in the corner, where particles remain trapped [25]. The interface between capillaries and unions of differing inner diameters effectively create corners for crystals to become trapped and eventually interfere with the flow of incoming crystals, and should be minimized where possible.

In order to ensure the crystal slurry does not clog the capillary it is sometimes necessary to filter the larger crystals from the slurry. Off-the-shelf stainless steel and PEEK filtration frits are common in chromatography applications to filter out particulates of different sizes, such as 2 or 20  $\mu\text{m}$  cutoffs. These filters are effective

for biological fluids with objects typically much smaller and more flexible able to pass through unharmed while filtering foreign particulates. However, crystals are more rigid and might not pass through these filters. Testing should be done to understand how the crystals interact with the filtration method or devise new gentler filtration methods compatible with the crystals.

*Sedimentation* Except for the high viscosity injection methods, settling is one of the most prevalent problems throughout all injection techniques—given sufficient time crystals can even sediment in high viscosity media. For  $\mu\text{m}$ -sized crystals, it is more a matter of when, not if, the crystals will sediment. Placing a cylindrical reservoir vertically with the sample exit at the bottom seems ideal, but it will lead to an eventual clog. Most crystal slurries are in the creep flow regime, where viscous forces are left to balance the gravitational forces. Particles the size of the protein crystals reach their terminal velocity quite readily. Balancing the Stoke's drag of a particle moving at its terminal velocity with its buoyant forces results in an equation for the particle velocity

$$\vec{U} = \frac{2\rho_0 a^2}{9\mu} \left( \frac{\rho}{\rho_0} - 1 \right) \vec{g}$$

of a particle with radius  $a$ , and the particle's mass density  $\rho$ , suspended in a fluid with viscosity and mass density  $\mu$  and  $\rho_0$ , respectively. The velocity of sedimentation helps determine when the particles have sufficiently sedimented and will likely no longer flow through appropriate flow paths. As the particle concentration at the bottom of the reservoir continues to increase, the connected capillary will ultimately clog, despite the crystal sizes being smaller than the capillary diameter. Placing the reservoir horizontally with the exit to the side avoids the issue of clogging from sedimentation, but now the sample sediments past the streamlines that will guide the crystals into the capillary entrance towards the interaction region. A standard SFX reservoir inner diameter is approximately 5 mm and it would take approximately 90 min for 1  $\mu\text{m}$  sized objects to settle past the capillary entrance (at the reservoir's midline) if it were suspended in water; 20 min for 2  $\mu\text{m}$  objects (assuming an object with density similar to that of a protein  $\sim 1.2 \text{ g/cm}^3$ ).

The most commonly used method to prevent sedimentation in the sample reservoirs is to rotate the reservoirs in order to modify the direction of the gravity vector. Lomb et al. [20] has shown an approach where the sample is loaded into syringe-like reservoirs and rotated. There have been some modifications made to the technique, but the basic idea of rotating the sample slowly back and forth has been used frequently in SFX experiments. It is not an infallible approach and should be tested prior to the experiment to ensure the crystal morphologies and the properties of the fluids are properly matched to the rotation speeds and frequencies of the sample shaker. Recall, it is a device to slow the sedimentation and not resuspend it. Once the particles are settled, the properties of the creep flow regime make it difficult to resuspend them by shaking or moving the plunger back and forth. Properties of

laminar flow mean that the particles will flow back and forth to the same position along the same streamlines and require turbulence or mixing or some other external force to homogeneously redistribute them. This is the same physical phenomena that explains why microscopic spermatazoa swim with cork screw tail motions instead of the back and forth motion typical in humans and fish swimming at the macroscale [26].

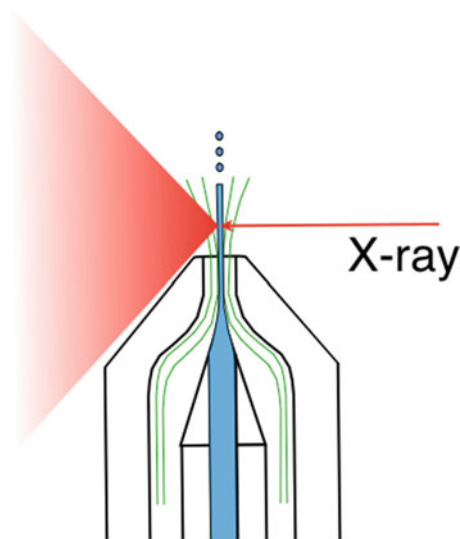
### Key Takeaways

- The crystal slurry dominates the flow physics
  - Particle size sets minimum capillary diameters ( $<2/5$  capillary diameter)
  - Fourth order dependence on transport tube inner diameter can increase flow rates too much, setting upper and lower size limits
  - The viscosity of the mother liquor combined with the increased viscosity caused by the suspended particles means sample fluids in capillaries are more viscous than expected
- Flows are typically laminar and dominated by viscous forces rather than inertial; diffusion and viscosity limited, no turbulence.
- Settling affects numerous sample delivery methods and can be a detriment to experiments.
- In vacuum experiments have an intrinsic minimum pressure gradient not present at ambient pressure.
- Although not discussed in the chapter, proper microfluidic hygiene is important
  - Smooth perpendicular cuts to tubes and capillaries
  - Minimize flow impedances
    - Prime bubbles out of the lines, as trapped gasses can be large flow capacitances
    - Resistances such as too many unions, or small flow restrictions should be minimized
    - Minimize swept, or dead, volumes to conserve sample.
- There is no substitute for testing and characterizing the experiment as faithfully as possible, that is, injection tests with the actual crystalline samples, if possible, in the actual vacuum chamber in front of an X-ray source will minimize surprises during the beam time. Successfully delivering just the mother liquor in air or rough vacuum is a good start but can be misleading compared to [the actual] sample slurry.

## 5.2 Standard Liquid Injectors

In Serial Femtosecond Crystallography, every nanocrystal that is hit by an X-ray pulse is destroyed by the interaction that deposits a lot of energy in a small volume. Most of the requirements on SFX sample delivery listed in the overview can be fulfilled with a liquid jet injector. A microscopic liquid jet can be obtained in the

**Fig. 5.5** Schematic view of GDVN. The end of the nozzle is beveled to allow diffracted X-rays (the red cone) to reach the detector. Green lines are gas streamlines, which accelerate and compress the liquid to produce a small jet from a larger orifice. Blue is the liquid containing protein microcrystals. The X-ray FEL pulses hit the liquid jet before it breaks up into droplets



simplest way by discharging a liquid through an orifice at high liquid pressure. A continuous liquid jet emerges, with a diameter identical to the orifice diameter (Rayleigh jet) [27], which breaks up into droplets due to capillary forces. The droplets have a diameter of about twice the jet diameter and an average spacing of 4.5 times the orifice diameter [28]. In X-ray FEL experiments with liquid jets, the X-ray pulses hit the liquid stream ideally before it breaks up into droplets to assure a high efficiency (every X-ray pulse hits the liquid). However, Rayleigh jets have a few disadvantages: high flow rate (0.4–7 mL/min) and high jet speed (100 m/s), large jet diameter (10–100  $\mu\text{m}$ ), susceptibility to clogging for smaller orifice diameter (especially when the liquid contains protein crystals) and susceptibility to freezing in vacuum when the flow is interrupted. The liquid jet diameter for serial femtosecond crystallography should ideally be similar to the X-ray beam diameter, which is between 10  $\mu\text{m}$  and 0.1  $\mu\text{m}$  at LCLS for example. Liquid jets of such diameter cannot be obtained with a Rayleigh jet nozzle due to clogging issues.

These issues have been solved with the Gas Dynamic Virtual Nozzle (GDVN). This nozzle was developed based on the observation that shear and pressure forces of a sheath gas can reduce the diameter of a liquid jet to a value smaller than the orifice diameter [13, 29]. GDVN nozzles generate a liquid stream of micron to submicron diameter with flow speeds of 10–100 m/s at flow rates of 1–20  $\mu\text{L}/\text{min}$ . They consist of an inner sample capillary with typically 40–75  $\mu\text{m}$  inner diameter, and an outer gas capillary that provides a co-flowing gas stream that accelerates the liquid and thereby reduces the diameter of the stream (see Fig. 5.5).

The acceleration and reduction in jet diameter occurs over a very short distance at the exit aperture of the nozzle. The liquid microjet breaks eventually up into droplets due to the Rayleigh–Plateau instability [27]. The diameter of the liquid jet is reduced by a factor of 10–50 compared to the inner diameter of the sample

capillary. Any particle which is smaller than the sample capillary inner diameter but larger than the jet diameter (e.g., a large crystal) will simply pass through the system and only momentarily disrupt the jet, that is, the nozzle does not clog as easily as a physical nozzle of a size similar to the GDVN jet size. The inner sample capillary is centered in the outer gas tube by laser-cut Kapton spacers. The mass flow rate of the co-flowing gas stream is 20–30 mg/min and the sheath gas used is typically Helium or Nitrogen, where the use of Helium usually results in a more reliable jet. Due to the low viscosity of the mother liquor used to grow most protein crystals, microcrystals settle in the liquid due to gravity, and therefore an anti-settling device [30], as discussed in the previous section, is required for SFX to slowly rotate the sample reservoir and prevent settling.

The X-ray beam is focused onto the contiguous part of the jet, before the droplet breakup, usually 100–200  $\mu\text{m}$  away from the nozzle exit. The background scattering from the contiguous jet is lower than from the droplets, since the droplets have about twice the diameter of the jet. Scattering from the cylindrical shape of the jet leads to a streak in the diffraction pattern at low spatial frequencies if the X-ray beam is not significantly smaller than the jet.

The outside of the GDVN is beveled at the end to avoid shadowing of the diffracted X-rays. The gas focusing aperture is formed by flame polishing and variations in shape and size between different nozzles are almost unavoidable. For the liquid jet to emerge aligned with the axis of the GDVN, the sample capillary must be accurately centered on the axis of the gas-focusing aperture. To make centering easier, a square outer glass tube may be used [31] for automatic centering of the round sample capillary. But even in this case, the flame polishing procedure may not result in a gas aperture hole which is exactly on the center axis of the square glass tube. These manufacturing difficulties led to the introduction of 3D printed GDVN nozzles [32]. A high resolution two-photon 3D printer is used to print the critical GDVN endpiece with high precision at a resolution of 500 nm, and a liquid and gas capillary are glued into the 3D printed part (see Fig. 5.6 and Fig. 5.7). A key advantage of 3D printing technology is that more complicated shapes can be printed (e.g., mixing nozzles [33] or double flow focusing nozzles [23]) as will be discussed further in this chapter.

GDVN jets can be used at atmospheric pressure and in a vacuum environment. Using the GDVN in a vacuum environment can create challenges: High vacuum can be easily maintained in the presence of a microscopic liquid Rayleigh jet [11], but the focusing gas introduced into the vacuum raises the base pressure of the experimental chamber. Therefore, a differential pumping system is used, for example, at the Coherent X-ray Imaging (CXI) endstation at LCLS to protect the high vacuum system and the beamline optics and X-ray detector. The GDVN is mounted on a nozzle rod in a differential pumping shroud, which contains several openings for cameras and pump lasers for pump probe experiments. The nozzle rod can be retracted behind a gate valve and removed from the vacuum system for nozzle changes. Several motorized stages allow alignment of the nozzle relative to the X-ray beam [34]. An initially installed in-vacuum microscope for nozzle observation [34] has since been replaced by an optical system (microscope

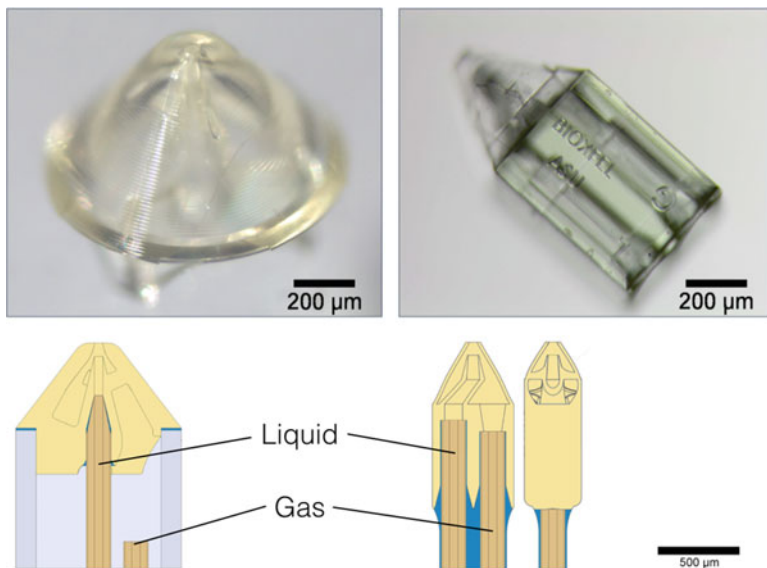
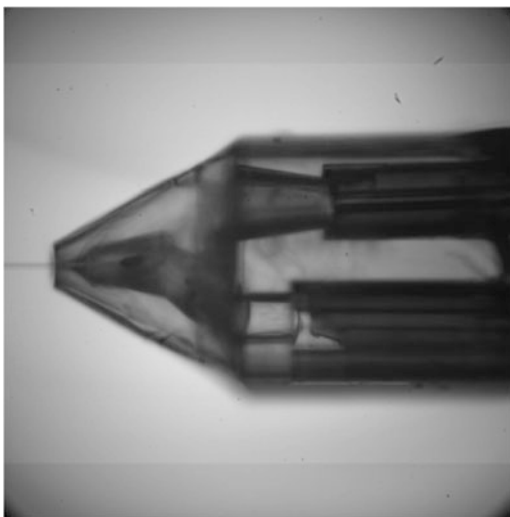


**Fig. 5.6** 3D printed nozzles: left: this design requires a micromanipulator and mounting stage to glue the capillary into the printed nozzle tip. Right: the new design is easier to attach to the gas and liquid capillaries. Grey: Steel or Glass, light brown: printed material, dark brown: polyimide-coated glass capillary, blue: epoxy

**Fig. 5.7** 3D printed nozzle in operation. Liquid line on bottom, gas line on top



objective and transfer lens in vacuum), which allows the use of more sophisticated cameras outside the vacuum chamber. This allowed the use of high-speed cameras or stroboscopic recording modes to visualize the damage inflicted onto the jet during X-ray exposures [2].

GDVNs have been successfully used in many SFX and Wide Angle X-ray Scattering (WAXS) experiments at LCLS and SACLA, as well as in electroflow-focusing mode to aerosolize single particle samples in an aerodynamic lens system (as shown in Fig. 5.3) [35]. The flow rate and jet speed of the GDVN is not optimized for the X-ray pulse repetition rates of SACLA or LCLS: at 120 Hz repetition rate and 10 m/s jet speed, the distance that the jet travels between two pulses is about 8 cm. This means most of the sample goes to waste in between pulses. This is unacceptable for many membrane proteins which can only be expressed in small quantities. Therefore, other injection methods have been explored which consume less sample, as will be described in the following chapters. For future high repetition rate X-ray FELs, sample waste with the GDVN is not expected to be a problem. At the European XFEL with bunch trains arriving at 10 Hz, where the pulse repetition rate within each bunch is 4.5 MHz, it remains to be seen if the GDVN jet speed is even fast enough to keep up with the high repetition rate pulses. This is especially a problem if shock waves from the sample explosion travel upstream in the jet and cause additional damage [2]. At LCLS-II, with a sustained repetition rate of 1 MHz, the jet speed seems to be perfectly matched to make use of the entire sample with minimal waste. This however presents a new challenge with sample debris. Currently, for a GDVN, most of the sample collects in a catcher away from the interaction region. With a high intensity, high repetition rate X-ray FEL beam, most of the sample will be vaporized by the beam, no longer collecting in a catcher away from the interaction region but rather rapidly coating every surface close to the interaction region, including the nozzle tip. The extent to which debris will be a problem with high repetition rate machines remains to be seen. Sample consumption with the GDVN can be reduced by a factor of about eight by using a double flow focusing nozzle [23], where the sample flow can be reduced by a second focusing liquid, before gas focusing occurs (see Sect. 5.5).

### 5.3 High Viscosity Injectors

In recent years, protein crystallization in lipidic cubic phase (LCP) has led to structures of many important human membrane proteins, which are highly important and the subject of Chaps. 4 and 11 of this book. The desire to stream protein crystals in LCP into the X-ray FEL beam for SFX led to the development of the high viscosity injector. LCP has a viscosity comparable to car grease or tooth paste (dynamic viscosity of  $\sim 48.3$  Pa·s [36] compared to water at  $8.9 \times 10^{-4}$  Pa·s and Ethanol at  $1.1 \times 10^{-3}$  Pa·s) and thus cannot be used with a GDVN, since the long sample capillary with an inner diameter of tens of microns would require impractically high pressures to make the liquid flow. Therefore, a new injector had to be designed that uses only a very short sample capillary and a hydraulic stage to achieve the high pressure needed to drive the sample through this capillary. Figure 5.8 shows a schematic of one version of an LCP or high viscosity injector.

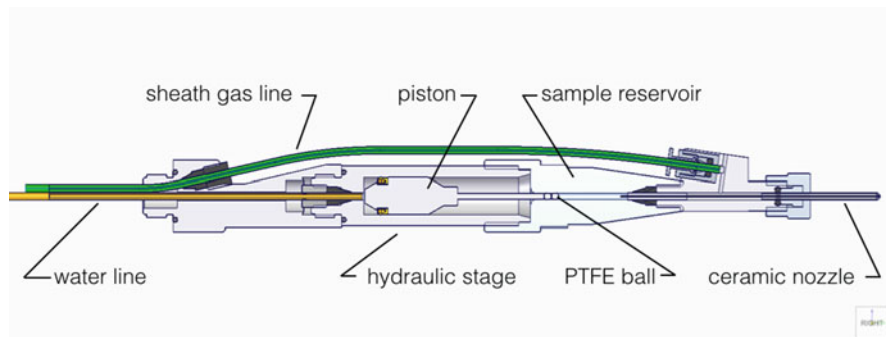
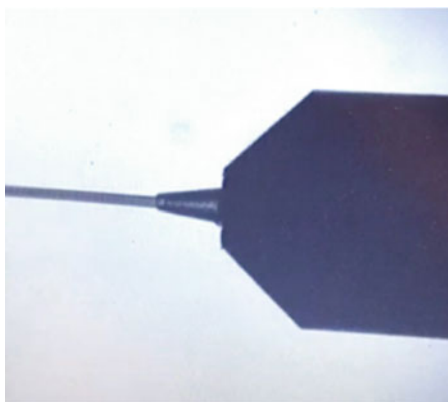


**Fig. 5.8** High viscosity injector. It consists of a hydraulic stage, which is pressurized by an HPLC pump. The piston pressurizes the sample in the reservoir and drives it through the capillary. The ceramic nozzle ensures that sheath gas surrounds the extruded high viscosity material and keeps the flow on axis

**Fig. 5.9** LCP stream extruded through a  $50\ \mu\text{m}$  inner diameter capillary; the stream has the same diameter as the capillary inner diameter. The large shadow on the right is the ceramic gas aperture



An HPLC pump supplies water at constant flow rate and moves a plunger in a syringe body. The plunger has a large diameter on the water side and a smaller diameter on the sample side, where it applies pressure on a Teflon ball. The ratio of the two plunger diameters equals the pressure amplification of the hydraulic stage. The Teflon ball acts as a secondary plunger, it is sitting in the reservoir bore, which has a slightly smaller inner diameter than the ball diameter, thus forming a tight seal against pressures up to 15,000 psi. The LCP sample is pushed by the Teflon ball from the reservoir into a capillary with a diameter of 20 to  $50\ \mu\text{m}$ , selected depending on crystal size. An LCP stream emerges at the distal end of the capillary (Fig. 5.9). Different reservoir sizes can be made, for example: 25, 40 and  $120\ \mu\text{L}$ .

The diameter of the extruded stream is identical to the capillary inner diameter. To keep the stream straight and on axis, a co-flowing gas is surrounding the stream. The distal end of the capillary is ground in a conical shape and protrudes out of the gas aperture, which has a square inner diameter and opening to allow a path for the sheath gas (see Fig. 5.10). A ceramic injection molded gas aperture is used,

**Fig. 5.10** Injection molded ceramic gas aperture with protruding coned sample capillary (50  $\mu\text{m}$  inner diameter). The gas aperture hole in the ceramic part has a square shape to allow sheath gas to exit and surround the sample stream

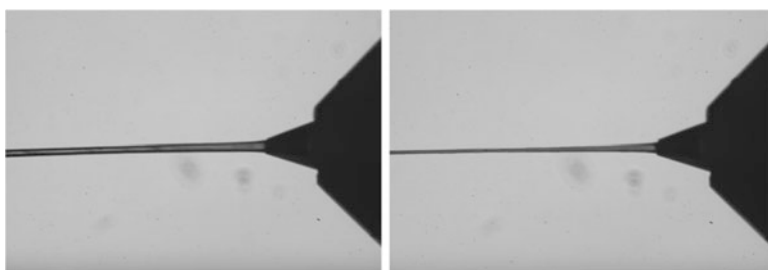
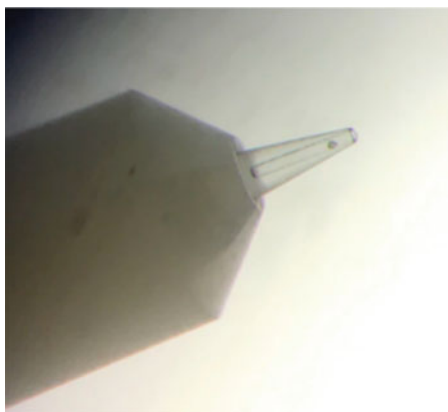


**Fig. 5.11** PEO extrusion with high viscosity injector into ambient pressure. Nitrogen sheath gas exits the nozzle surrounding the capillary cone, which is protruding out of the ceramic gas aperture. Left: mass flow rate of sheath gas (Nitrogen): 5 mg/min. Right: mass flow rate of sheath gas (Nitrogen): 15 mg/min. Same liquid flow rate in both images: 90 nL/min

which has a more reproducible shape and longer life than the previously used hand melted glass tubes [37]. The high viscosity of LCP prevents crystal settling due to gravity on the time scales of a measurement. The sample flow rate can be adjusted and optimized for the X-ray FEL pulse repetition rate, so that the stream advances only the distance needed to replenish the damaged material from the last pulse.

Unlike in the GDVN, the LCP stream cannot be focused down to a smaller diameter by the sheath gas. However, another high viscosity medium does allow a reduction of the stream diameter by shear forces from the sheath gas, as seen in Fig. 5.11 for PEO, a gel polymer of high-molecular-weight poly(ethylene oxide). The PEO stream, which shows already reduced background scattering compared to LCP [38] (by a factor of about 1.5 in the diffuse ring region), can be reduced in diameter from initially 50  $\mu\text{m}$  to about 20  $\mu\text{m}$ , which reduces scattering background further. PEO extrusion works best at ambient pressure, for example at the MFX beamline at LCLS or the DAPHNIS endstation at SACLA [39] and at Synchrotrons. It is particularly hard to start a stream of PEO with the high viscosity injector, since PEO is very sticky and tends to ball up at the end of the nozzle. Once started, though, the PEO stream runs very reliably if the sample does not contain any gas bubbles.

Injection of short bursts of isopropanol into the gas line with a switching valve to remove PEO accumulation at the nozzle tip makes starting the stream much easier. Using a mass flow meter in the gas line also helps to find the correct gas flow for proper operation.

Other high viscosity media for crystal embedding have been developed (e.g., hydrophobic media like grease [40] and Vaseline [41]) which form emulsions with crystals in small droplets of mother liquor. These carrier media however produce high background scattering and are often incompatible with membrane proteins. Hydrophilic viscous carrier media do not have these disadvantages, and several have been described: agarose [42], hyaluronic acid [43], and two hydrophilic gelling polymers [44].

The high viscosity injector uses sample much more economically: the flow rate of the microjet from a GDVN is usually 10–30  $\mu\text{L}/\text{min}$ , whereas the sample flow rate with the high viscosity injector can be adjusted from 0.01 to 2  $\mu\text{L}/\text{min}$ . This means that sample consumption is greatly reduced compared to GDVN injection. This is highly desirable for samples like G-Protein Coupled Receptors (GPCRs) which can only be expressed in small quantities. There is an increase in stream diameter compared to the GDVN, but the drastic reduction in flow speed from 10 m/s with the GDVN to  $\sim 2$  mm/s with the LCP injector leads nevertheless to a large reduction in sample consumption.

Several GPCR crystal structures have been solved by SFX in LCP using the high viscosity injector, for example the human Smoothed (SMO) receptor in complex with cycloamine [45], the angiotensin receptor [46], the human  $\delta$ -opioid receptor [47] and rhodopsin bound to arrestin [48] and the human glucagon receptor. Pump probe experiments with bacteriorhodopsin crystals in an LCP stream have been performed [49] as well as native phasing measurements on human A2A adenosine receptor, which after phase extension lead to a 1.9 Å structure [50]. Microcrystals of soluble proteins have been mixed into LCP and used with the high viscosity injector for structure solutions [51]. For LCP SFX experiments in vacuum, as at the LCLS CXI instrument, extra measures must be taken to prevent a phase change of monolein LCP into a lamellar phase due to water loss by desiccation and temperature reduction due to evaporative cooling. This would lead to strong diffraction rings which mask weak Bragg reflections. To that end, a shorter chain length lipid can be added to the LCP post crystallization [45] which lowers the phase transition temperature.

Serial crystallography experiments with high viscosity micro streams can also be done at synchrotron sources, albeit without the dramatic reduction in radiation damage possible at XFELs. Fast detectors allow shutterless data collection from a stream of microcrystals in its LCP growth medium with 20–100 ms exposure times. The extrusion speed of the sample and exposure time can be adjusted depending on the flux of the beamline to allow for full exposure of each crystal to the damage limit at room temperature. Serial Millisecond Crystallography has been demonstrated successfully at the Advanced Photon Source [38], the Swiss Light Source [41] and the European Synchrotron Radiation Facility [52].

## 5.4 The Microfluidic Electrokinetic Sample Holder

Mating the protein crystal suspension with a type of sample delivery method is one of the most critical aspects to successfully execute an experiment at an X-ray FEL. A major concern in SFX is sample consumption, since many proteins cannot be readily crystallized in arbitrary quantities. In 2009, Chapman and Seibert et al.'s [3, 4] first biological experiments at an X-ray FEL were limited to soft X-rays (<2 keV) and thus required a vacuum sample environment and the low solvent background and sample replenishment of a thin liquid jet or a solvent-less aerosol injector. To address the issue of higher sample consumptions, the microfluidic electrokinetic sample holding (MESH) technique was developed in 2011, where instead of accelerating the meniscus with aerodynamic or hydrodynamic forces, electrokinetic forces are employed. A room temperature structure of thermolysin was originally solved to better than 4 Å [53], demonstrating the MESH technique, but as better data analysis algorithms were developed, the same data could be used to extend the resolution to 2.1 Å [54]. The MESH was successfully used to solve room temperature structures of photosystem II [55–57], demonstrate minimal electronic structure changes caused by high intensity X-ray FEL pulses by collecting simultaneous X-ray emission spectra and diffraction [58, 59], collect X-ray emission spectra in the soft X-ray regime [60–62], and collect novel structures on nanocrystals [63]. In all of these experiments, the mother liquor was doped in order for the crystals to survive the vacuum injection. The capillary geometries varied from 50 to 100 μm, with the flow rate not exceeding 3 μL/min, and in good running conditions, having flow rates in the sub-microliter per minute regime.

The following sections will explain how to use the MESH technique to deliver sample for in-vacuum SFX experiments. After discussing the MESH, a new method involving a concentric flow that keeps the low flow rate and allows the MESH technique to be applied to a broader range of fluid conditions will be discussed. The chapter concludes with a discussion on how a technique like the MESH and its variants fit into the grander scheme of a suite of sample delivery techniques available for SFX.

### 5.4.1 The Microfluidic Electrokinetic Sample Holder

The main difference between the MESH injection and other SFX injection methods is the way it supplies energy to the microfluidic system: an applied voltage rather than applied pressures. The microfluidic electrokinetic sample holder (MESH) technique is physically identical to electrospraying or electrospinning techniques [64]; however, the MESH technique is interested in the thin liquid jet created after the Taylor cone but before the eponymous spray or spun filaments typical of the other techniques. The applied voltage causes any free charge in the solution, typically solvated ions, to migrate towards or away from the voltage source, subject to the polarities. A net excess charge builds at the exposed meniscus, which

continues to repel from the like-charged voltage source. Once the applied voltage potential is high enough to overcome the opposing surface tension and viscous forces, fluid is ejected from the meniscus. A balance in flow rate and applied potential will then cause the meniscus to achieve different states, such as a dripping mode, the cone-jet mode, or the multiple jet modes (listed in order of increasing voltage, for a fixed flow rate).

The ability to eject charged particles is the real power of the MESH technique. Most biological fluids have free ions in solution and will respond to an externally applied voltage. The range of tubing and fluid properties typical in SFX experiments leads to currents at, and typically below, the  $\mu\text{A}$  range. Considering Faraday's constant ( $\sim 96,485\text{ C/mol}$ ), a fluid with 100 mM ionic strength operating in MESH conditions at  $1\ \mu\text{A}$  is ejecting 1 pmol of charged particles per second or consuming approximately 6 nL/min. Therefore, once a flow rate and voltage are found to stably create a cone-jet Taylor cone, there is minimal additional cost in sample consumption by the electrokinetics. The applied voltage focuses the meniscus and creates a thin liquid stream, but it minimally affects the fluid's flow rate, or the sample consumption.

The GDVN partially mitigates freezing in vacuum by always running a sheath gas, which accelerates the meniscus to make a jet and keeps the fluid at ambient temperature [13, 65]. To run the MESH in vacuum, the crystal slurry must be doped with a *cryoprotectant*, such as 40% glycerol [53]. The addition of glycerol interferes with the fluid's properties such that it will not evaporate and freeze or precipitate in vacuum. Typical—not all—additives tend to also increase the viscosity and alter other fluid properties, such as density and surface tension, which aid in reducing the flow speed as well as maintaining a homogeneous protein crystal suspension for longer.

#### 5.4.1.1 Charging the System

To create a MESH injection from the free surface of a liquid drop at the end of a capillary, an electric field must be present across the meniscus. The free ions in the solution will begin to accumulate and will slowly begin to be repelled from one another, because of their like charges, until they can overcome the surface tension and viscous forces holding them together as a liquid meniscus. Eventually, the meniscus will go from a hanging drop to the more familiar Taylor cone shape. A stable cone-jet mode passing protein crystals from the reservoir, through the capillary to the thin jet filament, and finally probed by photons is essentially the MESH technique.

In order to create this electric field, the meniscus can be placed between two charged electrodes, or a charged and grounded electrode. In the case of the MESH injector, the fluid is charged at its reservoir. This is intentionally done to avoid unwanted voltage arcs to discharge from charged metal towards sensitive scientific equipment in the sample chamber (e.g., detectors or motors). The difference between charging at the tip and creating an external electric field, versus charging

within the fluid and having the meniscus create the electric field, are subtle but very important to understanding the operation of the MESH technique and its shortcomings.

#### 5.4.1.2 Creating the Driving Electric Field

The charged fluid in the capillary acts like a conductive wire, where the fluid is poorly conducting and the fused silica and polyamide coating of the outer capillary walls insulate the charge. In order for the MESH technique to work properly, all charge must be contained in the capillary and reservoir and allowed only to escape through the meniscus via the *leaky capacitor* of the cone-jet physics.

At the meniscus, it should be the charge buildup that ejects charge via the cone-jet physics. If charge is taken away from the meniscus by the local atmosphere, this will prevent sufficient charge to buildup and MESH jetting will not be observed. MESH operation has been observed in air at ambient pressure, but below ( $\sim 200$  Torr) ceased to operate until the vacuum pressure was sufficiently low ( $< 5 \times 10^{-2}$  Torr), where it would begin to form a cone-jet again [53].

When the meniscus is the source of the electric field, any changes in the electrical properties of the meniscus create a varying electric field as non-conductive phases, such as the protein crystals, pass by. The ionizing X-rays can also affect the field if shot too deep in the meniscus. Even the vacuum dehydrating the meniscus can play a role in disrupting the local electrokinetics of the meniscus. A shortcoming of charging the reservoir is that any bubbles trapped in the sample capillary line, even small bubbles that do not fill the full diameter, severely hinder or completely stop the transfer of charge. The air bubble can act like an infinite resistor and will prevent the Taylor cone from forming, while the vacuum continues to draw in fluid as a large droplet; so crystal slurries should be bubble free for best injection.

#### 5.4.1.3 A Poorly Conducting Wire

The fluid-filled capillary can be treated as a wire with a known resistance that increases linearly with length, and inversely with both the cross sectional area and the conductivity. For commonly used fluid conductivities, through a meter-long, 50  $\mu\text{m}$  capillary, resistances [typically] vary from 0.1 to 10 G $\Omega$ . The flow of ions typically have the MESH operating in the 100s of nA regime. These values indicate that no more than a few hundred volts can be dropped across the length of the capillary; however, if higher viscosity fluids are used, which diminish the conductivity as charge cannot easily move, then higher driving voltages might be needed to account for the high resistance of the line. Currents much higher than this are indicative of a charge leak, which can severely diminish the functionality of the MESH injection.

Since the crystal solution is conductive, there can be no internal electric fields, as the free ions will quickly move to shield any unbalanced charge. The

structures determined using MESH thus far have not shown any differences between their MESH and conventionally-determined structures. Voltage-sensitive structures would potentially be affected by the electrokinetics of the MESH; recent [unpublished] data has suggested further studies are necessary. To date, there are no apparent adverse effects on structures by applying voltages typical of the MESH technique.

To properly MESH, a non-conductive tubing, such as fused silica capillary or polymer tubing, and a counter electrode is needed. The droplet exiting the capillary will wet upwards along the outside of the capillary if the closest grounding sources are the polymer fittings and mounting material holding the capillary into vacuum. The capillary should protrude at least 1 mm away from these to minimize external wetting. Note that if the capillary is protruding too much, the capillary starts to oscillate from the downstream spinning process. Everything in the MESH geometry should be a polymer or a non-conducting material except for the charging material. Any excess buildup of liquid, or fluids that wet backwards towards the sleeves and fittings can disrupt the field or cause a current leak.

The next sections will discuss counter electrode designs that will draw the charged meniscus in the correct direction for the experiment.

#### 5.4.1.4 Counter Electrode Design

Counter electrode (CE) design and function are very important to the MESH injection. Aside from the need to dope the fluid for vacuum injection, the counter electrode design considerations differentiate MESH injection from standard electrospray and electrospin techniques. A counter electrode close to the meniscus will give a high driving electric field, but it might interfere with the diffraction data. The shape should promote a homogeneous electric field like those between two parallel plates, yet precipitates from the sample can buildup and interfere with the electric field and ultimately grow back into the interaction region.

Typically, MESH injection charges the fluid and leaves the counter electrode at earth ground. However, the counter electrode can be charged and the fluid left grounded and the familiar Taylor cone will form (likely at different voltages). The ions in the fluid will collect at the meniscus and mirror the charges at the counter electrode. Eventually they will build up enough charge to begin to repel themselves and begin the Taylor cone phenomenon again. However, it is strongly recommended that the counter electrode be simply connected to earth ground rather than charged via a bias voltage because it is more dangerous to electrify the counter electrode the higher density of “free” electrons in metals. Copper, assuming one free electron per copper atom, has a [charge] density of over 13,000 C/mL whereas a fluid with 100 mM ionic strength has barely 10 C of ions per mL. Consequently, the metal in vacuum can readily discharge three orders of magnitude more charges than a typical MESH fluid of the same volume but this is not a concern when the counter electrode is properly grounded instead.

### 5.4.1.5 Counter Electrode Geometries

An ideal geometry for the counter electrode is one that creates straight electric field lines from the meniscus to the counter electrode, much like those between two plates in a parallel plate capacitor, but is impractical to implement. Instead, a counter electrode with a hole to allow the ejected, non-ionized mass through with proper spacing to create a sufficient electric field while not shadowing the diffraction detector is necessary. The distance of the counter electrode for the MESH injection is typically at least 5 mm, depending on the radius of the counter electrode. The counter electrode should be the closest conductive object to the capillary tip. A smaller hole is ideal for straight field lines from the meniscus (ideally a point source of charge), but the small opening can quickly build up debris and strengthen the field towards mass buildup, leading to injection failure. Nominally, the opening size in the CE is of the same order as the spacing from the capillary tip, typically 5–10 mm. Figure 5.12 shows different iterations of CE geometries used in atmospheric and vacuum conditions.

### 5.4.1.6 Sample Reservoirs

The preferred reservoir for MESH injection is a pressure-driven vessel. This method was described in Sierra et al. [53] and can be seen in Fig. 5.13. Here an open centrifuge vial is loaded with the 0.1–1 mL of sample and into an acrylic pressure vessel. The vessel is pressurized with an inert gas ( $< \sim 100$  psig), such as compressed air or nitrogen, while the capillary and a charging wire are submerged into the fluids like straws. The advantage of this technique is the simplicity of the sample loading as it uses common centrifuge vials. The plastic acrylic housing is adapted from an electrospray aerosol generator (Model 3480, TSI) and easily screws open to hold the reservoir and interface the capillary and wire. A steel nut on the lid of the acrylic housing has a platinum wire soldered to the bottom that is long enough to reach the bottom of the vial; the high voltage is connected to the outside of the nut, which in turn charges the submerged wire and the fluid. With the capillary submerged to the bottom of the vial, there is less concern with settling and clogging, as the sample is drawn in, as opposed to being forced in with other reservoirs. In this setup, there is a possibility for the sample to settle and become so concentrated that the fluid may continue to enter the capillary while the crystals aggregate and form a filter-like structure that prevent further crystals from entering.

It's important to recall that many fundamental fluid mechanics equations assume a homogenous fluid or dilute solutions. In the case of SFX sample delivery, homogeneity is not always a luxury. Growing the crystals in large batches rarely produces identical crystals. Even if the crystals are identical in size and morphology they are suspended in the solution as opposed to solvated in a solution. This contrast from a solid object to a liquid media makes a difference in injection behavior. The solid objects passing through a meniscus provide enough disruption that the Rayleigh breakup of the liquid jet comes sooner than the breakup of a pure liquid jet.

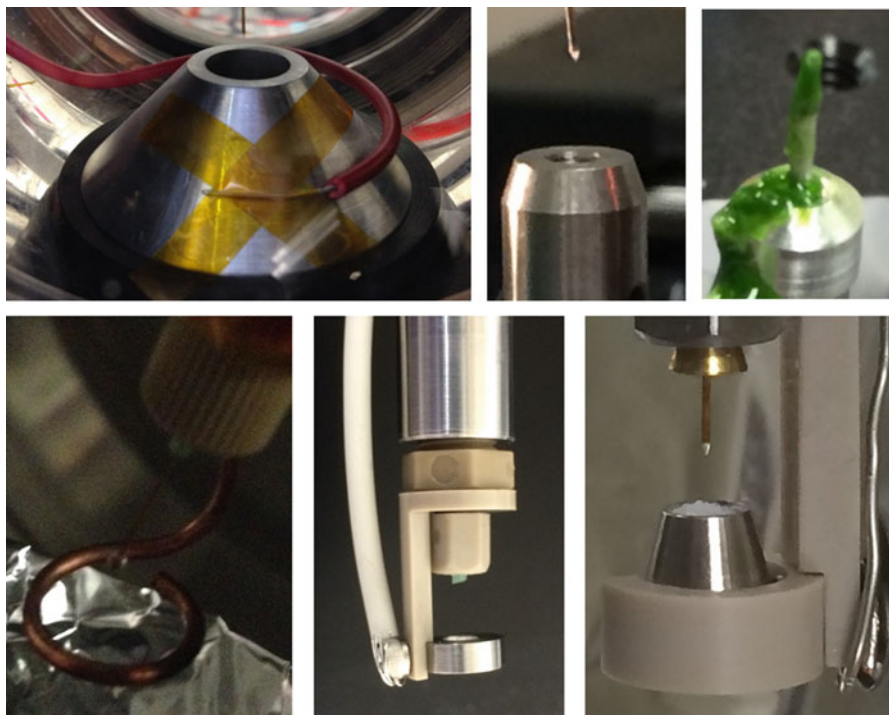


**Fig. 5.12** Different counter electrode geometries used for MESH injections. (clockwise) conical with flat and large hole (capillary visible above the hole); flat surface with hole (stainless steel optical post; capillary above hole); 2 mm pointed stainless steel pin (protein debris deposited on electrode after injection); thin-walled conical stainless steel with hole (deposited polymer and protein debris buildup visible); flat stainless steel with hole (MESH-on-a-stick geometry); copper wire loop. For scale, capillaries are 360  $\mu\text{m}$  outer diameter, standard PEEK fittings are for 1/16" OD tubing, optical post hole is tapped 1/4"-20 (in top middle image)

It is important to recognize these potential differences and understand that testing simply the mother liquor without suspended crystals is not enough to guarantee a jetting success as the bulk fluid slurry will behave like a more viscous media and need typically higher parameters to create an equivalent jet of pure fluid. Homogeneity is also a problem with viscous injection methods where insufficient mixing to create the media can create pockets of low and high viscosity causing running instabilities and erratic sample consumption. Many times the difference between a jet running mother liquor and a slurry carrying protein crystals can be evident from optical imaging; however, the jet behavior can be more telling. If the jet's behavior at the interaction region begins to stabilize and improve it is likely too good to be true: the crystals are no longer flowing and obstructing the meniscus. A later section discusses the effects these suspended solids had on the design of the MESH injection method.

**Fig. 5.13** A schematic of the modified pressure reservoir used for typical MESH injections, with actual picture inset. The pink centrifuge vial holds the sample and is held in place by the bottom of the acrylic housing. A Swagelok adapter with appropriate polymer tubing sleeve (green in photo) allows a capillary to be submerged into the vial, while maintaining pressure. A platinum wire electrically connected to the Swagelok fitting is also submerged into the vial

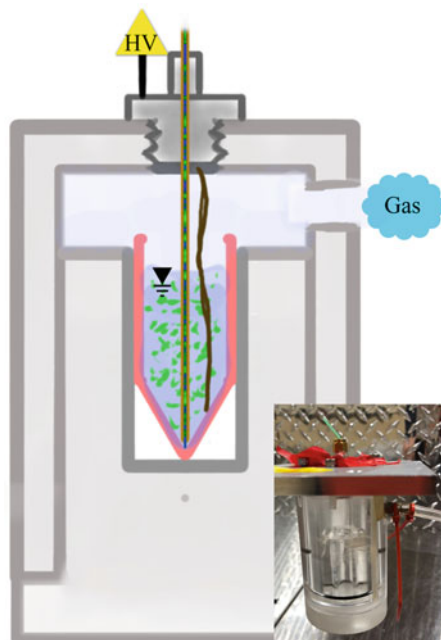
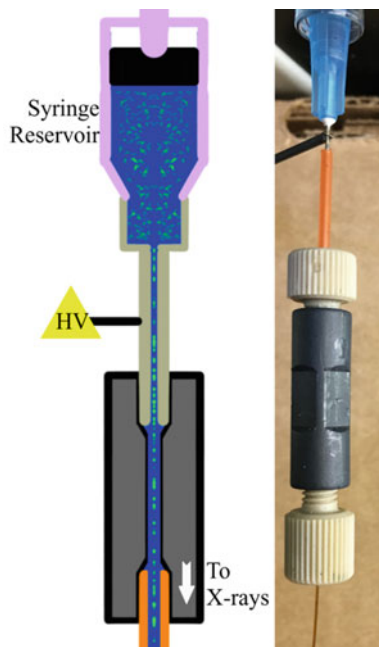


**Fig. 5.14** A common syringe with a stainless steel needle as a conduit between the fluid and the applied high voltage (HV). The outer diameter of the needle is fitted with standard polymer sleeves and microfluidic fittings to interface with the capillary of the MESH injection



The second preferred reservoir for MESH injection is to use a syringe and syringe pump as shown in Fig. 5.14. This setup is most amenable to quick and modular

deployments of MESH injection; it is especially ideal if compressible gases are not immediately available or an appropriate pressure vessel is not available. Any variety of plastic or glass syringes can be used as a sample reservoir. The needle must be conductive and must have an appropriate outer diameter that can interface with standard microfluidic fittings, such as 1/32" OD gaged needles. As the slurry advances from the syringe to the union, it wets the inner metal surface of the needle, which is charged externally, thus creating the voltage connection needed to perform a MESH injection.

Best suited for crystal slurry injection are glass gas-tight syringes, such as Hamilton's series of syringes. Volumes of 0.050, 0.100, 0.250, 0.500, 1, and 5 mL have all been used for MESH injection. The preferred syringe end is the removable needle variety, as it can handle higher pushing forces while still maintaining some modularity. The glass syringes can be tricky to keep electrically isolated. Most glass syringes have a metal plunger and a Teflon head to create the seal. When loading the syringe it is sometimes possible to have fluid get trapped between the Teflon and the glass wall. If this remains, it will create an electrical contact with the fluid and the metal plunger body, ultimately with the syringe pump. Although most devices are safely grounded, this current leak prevents the MESH injection from properly working.

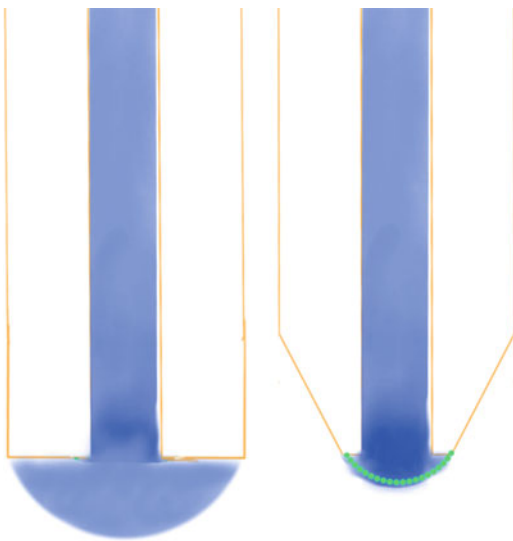
#### **5.4.1.7 The Effects of Low Reynold's Number Flow**

*Capillary Selection* Fused silica capillaries are commonly used for sample injection in SFX. The appropriate diameter size and the electrical insulation of the fused silica and polyamide coating make it an ideal tubing material for MESH injection. It is worth mentioning that other tubing materials are compatible with the MESH, such as borosilicate glass, quartz, and polymer tubing, such as PEEK.

One of the most important parameters in capillary selection is the inner diameter. As previously discussed, pipe flow is still applicable in  $\mu\text{m}$ -sized capillary flows and a useful metric is the hydrodynamic resistance of the system. Much like an element in an electronic circuit has some resistance to the flow of current from an applied voltage, a capillary of fluid will restrict volumetric flow with the application of a volumetric potential, that is, the pressure. The capillary diameter, length and fluid viscosity dictate the resistance to flow and can then be used to estimate the effect of changing these parameters.

Another restriction on the capillary geometry selection is from the sample itself. Again, the fluid properties from a crystal's mother liquor might dictate the viscosity and thus cannot be readily changed; however, the size of the protein crystals themselves begin to limit the geometries suitable for the SFX experiment. In most fluid mechanics calculations applicable to SFX, the fluid is treated as a continuum and species inside of the fluid are treated as dilute, solvated species not causing changes in the bulk properties of the fluid. This assumption cannot be maintained when dealing with a suspension of solid protein crystals on the order of 100s of nanometers to dozens of micrometers in dimension.

**Fig. 5.15** Schematic of a non-tapered capillary (left) with meniscus wetting the exposed flat surface out towards the outer diameter. By comparison, a tapered capillary (right) with the same outer diameter allows for a smaller meniscus and therefore smaller Taylor cone geometry



Tapering or polishing the capillary tip is not a necessity for MESH injections; however, it creates a smaller meniscus and subsequently smaller Taylor cones, thin filaments and progeny droplets. Figure 5.15 shows a schematic of the tapered versus non-tapered geometry. Crystal dimensions on the order of the meniscus size can cause jetting instabilities; for example, 25  $\mu\text{m}$  crystals passing through a 75  $\mu\text{m}$  tapered capillary face will be much more unstable than the same crystals through a non-tapered capillary with a 360  $\mu\text{m}$  capillary face.

The MESH injector flow rates vary from the 100s of nL/min for 50  $\mu\text{m}$  capillaries to almost 3  $\mu\text{L}/\text{min}$  for a 100  $\mu\text{m}$  capillary—assuming moderately viscous fluid additives (e.g., 5 mPa-s; water is  $\sim 1$  mPa-s). Figure 5.16 shows a plot of flow rates at different inner diameters for a MESH-compatible fluid. If the doped fluid has a viscosity different than  $\sim 5$  mPa-s, then the flow rate will scale inversely; for example, doubling the viscosity will halve the flow rate.

*Typical Fluid Properties for MESH* In crystallography, the fluid selection is typically governed by the protein crystallization conditions. Changing the properties of the mother liquor once the crystal is grown can lead from mild to severe degradation of the crystals [71] if not done properly; sometimes it is necessary for the experiment to succeed [72] and it can also improve the crystal quality [73]. As mentioned before, to work in vacuum, the MESH must contain some kind of cryoprotectant-like additive that allows it to stay liquid despite evaporation once in vacuum.

*Ionic Strength* The most basic of requirements for creating MESH injection is the free ions in solution. The free ions build up at the meniscus until a Taylor cone is formed (see previous sections; Gañán-Calvo and Montanero [74] and references within). A typical ionic strength for the fluid is on the order of 100 mM with

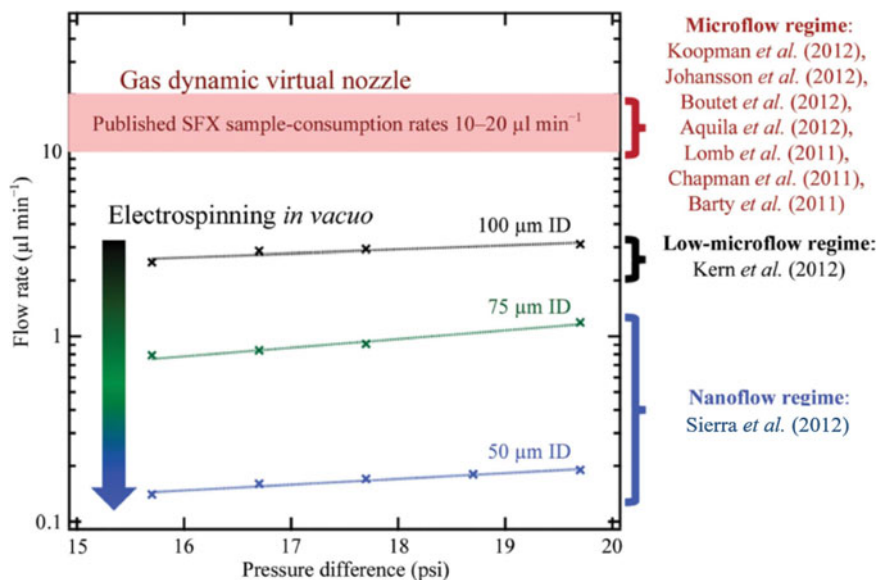


**Fig. 5.16** Reproduced with permission of the International Union of Crystallography [53] The figure shows the average flow rate versus the overall pressure difference (sample reservoir pressure to nominally 0 psi in vacuum) for different capillary inner diameters on the MESH. The rate was measured by weighing the volume of sample before and after an elapsed injection time. The fluid is a crystal-free solution composed of a common mother liquor: 30% w/v glycerol, 10% w/v PEG2000, 100 mM MES pH 6.5 and 5 mM CaCl<sub>2</sub>. The solution viscosity is approximately 5 cP. The compared flow rates are from the cited references [3, 22, 55, 66–70]

conductivities approximately 1 mS/cm; however, these values can vary above or below this point.

**pH Buffer** The free ions can be easily solvated ions, such as the divalent, cationic magnesium ions and the monovalent, anionic chloride ions of a magnesium chloride solution. The free ions can also come from a weak acid, such as anionic acetate ions and cationic sodium ions from a properly titrated acetate buffer solution. Either of these sets of free ions will create a MESH. The flow of ions is irreversible as the fluid leaves the meniscus towards the counter electrode and will thus change the electrochemistry. Without a proper pH buffer the solution can change pH and can adversely affect the protein crystal.

**Cryoprotectant** Some additives that have successfully created a MESH injection in vacuum have been: 30% glycerol + 10% PEG2000, 40% glycerol, 40% ethylene glycol, 1.4 M sucrose, 40% PEG400, 40% ethanol, 1:1 DMF:THF, 40% MPD. Ionic strengths (pH buffer and salts) of 100 mM are good starting points, with values ranging lower and higher; for example, 15 mM MnCl<sub>2</sub> solution has been the only free ions in a successful in-vacuum MESH injection for soft X-ray emission studies. Higher salt values are not prohibitive for the electrokinetics but can be

problematic in vacuum; for example, 2.5 M ammonium sulfate injects with the MESH in atmospheric conditions but does not survive the vacuum injection well due to precipitation. A benefit to the cryoprotectant additives is that they can potentially increase the fluid's viscosity, thus reducing the flow rate. It is possible that either the viscosity and/or density can also change favorably to help prevent any sedimentation of the suspended crystals.

*Capillary Length* At the CXI instrument of LCLS [75], nozzle rods over 1 m long set a minimum capillary length. Some additional length is typically necessary to get from the sample reservoirs to the interaction region. Capillary lengths of 1.5–2 m are therefore typically sufficient for MESH injection. If the fluid is too viscous it is likely that the meniscus will not focus unless higher voltages are applied, the diameter is increased or the capillary is shortened, that is, the effective conductivity is increased.

The MESH injection typically does not use sample shakers to prevent settling. In most cases, the increased viscosity aids in deterring the rate of sedimentation, or as discussed in the reservoirs section, the submerged capillary in the pressure-driven vial reservoir is less subject to the adverse effects of sedimentation. The other reservoir, the syringe-pump-driven approach, is more difficult to rock back and forth. Although early versions of sample shakers for SFX essentially rotated a syringe pump, and smaller syringe pumps [20, 21] have been mounted on oscillation motors to mitigate sedimentation during MESH injection, the settling problem is still prevalent and ultimately not worth the additional complication introduced to the system. In the case of the MESH, many times larger crystals are used since the MESH can accommodate larger inner diameter capillaries, which lead to much faster sedimentation times. If this is inevitable, finding more viscous or dense media might be necessary. Also, priming the capillary with sample slurry as it is freshly suspended will buy some time before the sedimentation in the reservoir prevents the sample from entering the sample capillary. A useful method to monitor settling during the experiment is to bring a 1 mL vial of sample, load 500  $\mu\text{L}$  into the reservoir and keep the other 500  $\mu\text{L}$  in the vial, vertical on a bench in the lab. Once the crystals in the vial have settled a few millimeters below the top fluid surface, it might have settled more than the half of the syringe reservoir's diameter and it is likely time to intervene in order to increase the data collection rate.

### 5.4.2 Concentric MESH

In order to find a way to increase the effectiveness of the MESH, a concentric design was developed that leverages the laminar flow properties of fluids at that scale and allows a protective outer fluid to flow around and shield the sample-carrying inner fluid from the adverse effects of the vacuum. The idea of concentric fluid flows is not novel, even in the field of SFX—the GDVN uses an outer fluid of helium gas to focus the inner sample-containing fluid. The next logical step is to use another

liquid instead of a gas to flow around an inner fluid. The application of this idea to the GDVN is presented in Sect. 5.5. At these low Reynold's numbers the interface between the fluids will be subject mostly to viscous, diffusive forces, rather than inertial, convective forces and mixing on short length scales can be neglected. The diffusion time is low, that is, the fluids remain separate and continue in their typical laminar flow, where the outer fluid only applies a shear rate to the internal meniscus while protecting it from any ambient environment.

MESH is limited to the subset of protein crystal slurries that could tolerate the doping with  $\sim 40\%$  cryoprotectant. Not all crystals can handle this change in their mother liquor and thus the need for a new method was developed the coMESH [21]. In the case of the ribosome and Photosystem II (PSII) structures [21], the MESH and coMESH were ideal to limit the sample consumption; however, the large unit cell of the ribosome made it very sensitive to changes to the mother liquor and necessitated the coMESH. For PSII, the coMESH aided the data collection by protecting the mother liquor from the dehydration of the meniscus [21, 57].

#### 5.4.2.1 coMESH Geometries

Figure 5.17 shows a schematic of the coMESH setup. Commonly, a  $100 \times 160 \mu\text{m}$  inner sample line approximately 2 m in length will run uninterrupted from the sample reservoir to the interaction region. The capillary is thin enough that it will pass through common microfluidic tees, such as those from IDEX Health Science (P-727-01) or Labsmith (seen in Fig. 5.17). The inner diameter of the tees is typically 500 or 250  $\mu\text{m}$ , respectively, allowing for fluid to pass around the outside of the inner sample capillary. At the reservoir end of the tee, an appropriate sleeve (e.g., IDEX F-246 for 150 and 160  $\mu\text{m}$  OD tubing and F-240 blue for 200  $\mu\text{m}$  OD) will seal off the outer diameter of the sample capillary. The parallel port on the tee will have the concentric outer capillary and will seal with the appropriate sleeve (IDEX F-242 for 360  $\mu\text{m}$  OD tubing). The length of this tubing is dictated by the experimental geometry. In some cases, the experimental geometry can permit a larger injector mounting surface and thus allowed the Labsmith piece to be near the interaction region [21]. This afforded a shorter concentric capillary approximately five centimeters in length; the short distance, resulted in a centered inner capillary. Since, a MESH-on-a stick [63] geometry has been employed (seen in Fig. 5.12), requiring the off-the-shelf tees to sit outside of vacuum, meaning that the concentric line must now be approximately 1.2 m in length in order to safely sit outside of the vacuum chamber, while sufficiently long to connect the reservoir to the interaction region.

The outer flowing liquid is chosen similarly to the MESH, where a 40% additive helps prevent freezing and can inadvertently increase the viscosity of the fluid. This should be carefully considered and tested prior to the experiment. The inner line carrying the mother liquor and crystals can have much less fluidic resistance than a 10–50  $\mu\text{m}$  annulus, meaning that the fluid that should not be exposed to vacuum

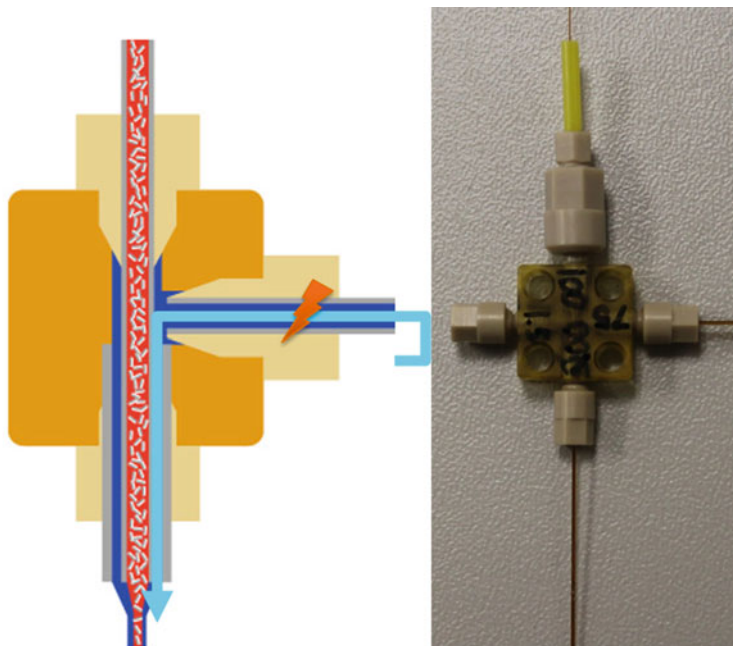


**Fig. 5.17** A picture and schematic of the concentric assembly enabling the coMESH. The Labsmith cross has a  $100 \times 160 \mu\text{m}$  fused capillary passing through uninterrupted (top channel through bottom); this is the sample line carrying the crystals in mother liquor (red). A concentric line  $180, 200,$  or  $250 \times 360 \mu\text{m}$  is connected to the bottom channel of the cross. The length depends on the overall experiments geometry; the inner and outer lines are typically left coterminous. The right channel is of arbitrary geometry sufficient to connect the accompanying sister liquor reservoir and charge conduit to the concentric annulus (blues). Appropriate Labsmith fittings and polymer sleeves are used to interface the capillaries to the cross

to avoid freezing can readily get to the interaction region with potentially no *sister liquor* there to protect it.

This is not to say that the other annulus geometries could not work, rather it suggests that they will require higher driving pressures to ensure sufficient fluid delivery. As discussed in prior sections, the reservoir of the MESH needs to be electrically isolated, which results in the use of plastic pressurized vessels or plastic or glass syringes pushed by a syringe pump. These methods typically are not high pressure applications, with plastic pressure reservoirs only capable of safely holding hundreds of psi ( $<70$  bar) and common syringe pumps having linear forces of approximately 89 N (it is possible to have a syringe pump with a higher linear force). If a commonly-used 1 mL plastic syringe (bore diameter of  $\sim 4.5$  mm) is used to drive the 160, 180 combination of capillaries it would struggle to achieve the 55 bar (800 psi) required to drive the flow. The syringe plunger might also fail before the syringe pump fails and cause charged liquid to leak behind the plunger

and undesired current leaks. This can get worse if the inner fluid is low viscosity and flows faster than a more viscous outer fluid.

The third and final line, attached to the perpendicular section of the tee junction (right of the tee schematic and picture of Fig. 5.17), is somewhat arbitrary, and should likely be a large bore polymer tube or capillary. This tube will interface back to a syringe filled with the appropriate sister liquor and will be connected to allow for charging, as explained in the previous MESH section. This line is essentially acting as a wire connecting the charge to the system. See the prior sections on discussions about making the tube sufficiently short for high viscosity, poor conducting media. A 1-m tube with an ID  $>250\ \mu\text{m}$  is typically sufficient to deliver charge to the concentric portion.

### 5.4.3 Conclusion

The MESH and coMESH are two electrokinetic techniques that are used to deliver fluids with a wide range of viscosity to SFX experiments. The power of the applied voltage allows the sample consumption to remain low, ranging from hundreds of nanoliters per minute in a  $50\ \mu\text{m}$  ID capillary through  $3\ \mu\text{L}/\text{min}$  in a larger  $100\ \mu\text{m}$  capillary, compared to pressure-driven flows. The MESH and coMESH techniques can tolerate a wide range of flow viscosities, from volatile solvents like ethanol, dimethylformamide (DMF), and tetrahydrofuran (THF) [60–62] to high molecular weight PEGs and possibly more [21, 53, 55, 57, 59, 63]. The electrokinetic injection methods fill a large gap between the other liquid injection methods like the GDVN and LCP (or high viscosity extrusion) methods, which work well for water-like slurries and highly viscous media, respectively.

## 5.5 Double Flow Focusing and Mixing Nozzles

### 5.5.1 Challenges in Liquid Jet Sample Injection

Despite tremendous progress in sample delivery for serial crystallography [76] in the past years, there are still many obstacles to overcome in order to make SFX as efficient as traditional macromolecular crystallography. This subchapter will focus on liquid jet technologies and their challenges and possible improvements, whereas other methods to introduce sample into the X-ray focus are discussed in the rest of this chapter. As discussed in Sect. 5.2, the first SFX experiments [3, 68, 77] at LCLS [78] were conducted using GDVN [13] for sample delivery because of the reduced risk of nozzle clogging and the ability to produce jets with flow rates and diameters compatible with the initial serial crystallography experiments. In these initial experiments detector geometries and challenges in data analysis were the

limiting factors. With these challenges addressed it became more and more clear that there are certain disadvantages [21, 23, 79] of the GDVN mode of injection:

- (a) The low probability of an X-ray pulse interacting with a crystal
- (b) Very high sample consumption compared to traditional crystallography
- (c) Short runtime of a nozzle
- (d) Danger of debris and ice formation (in vacuum) on nozzle tip
- (e) Danger of debris and ice growth (in vacuum) from the sample catcher back to the nozzle
- (f) The low reproducibility of the GDVN; each GDVN is one of a kind.

Given all these disadvantages that may prevent the success of a serial crystallography experiment, one would expect a shift away from GDVN, or liquid jet injection in general, towards other methods of sample delivery. However there are a number of advantages of liquid jet sample delivery that inspired the community to address the challenges rather than to abandon the technique. Liquid jet injection is ideally suited for fast sample replenishment, the X-ray background is small because most of the time crystals are of similar size to the jet diameter or are even larger, which is apparent in the missing “water-ring” in many diffraction images, and liquid jets can easily be used in vacuum. Most importantly, protein crystals can be injected in their native buffer and the injection method is compatible with light and/or oxygen-sensitive samples. Moreover liquid jet injection can relatively easily be combined relatively easily with all kinds of triggering methods for time-resolved crystallography, including light activation of native chromophores [80–83], mixing [84, 85] and light activation of photo-caged compounds. Double-flow focusing nozzles (DFFN) [23] tackle almost all the abovementioned disadvantages of the GDVN while retaining most, if not all, of the advantages.

## 5.5.2 Double-Flow Focusing Nozzles

### 5.5.2.1 Principle of DFFN

A double-flow focusing nozzle (DFFN) is a GDVN (see Fig. 5.18a) with an additional capillary inserted into the liquid capillary. The sample—in most cases a slurry of protein microcrystals—is flowing in the additional innermost capillary and is injected into the liquid stream from the manifold capillary, into which the innermost capillary is inserted, as shown in Fig. 5.18b. This combined liquid jet in turn is focused by helium gas, just as in a normal GDVN, which results in a liquid cone with the sample at its core (see Fig. 5.18b), as described by Gañán-Calvo et al. [86]. The flow conditions to form a jet [87–89] at a certain nozzle geometry [89] only need to be obeyed by the outer liquid and thus (a) the sample flow rate can be changed almost without interfering with the properties of the jet, which means that (b) one can change between samples on the innermost line without the need to interrupt the jet. Both points are very important, since the amount of

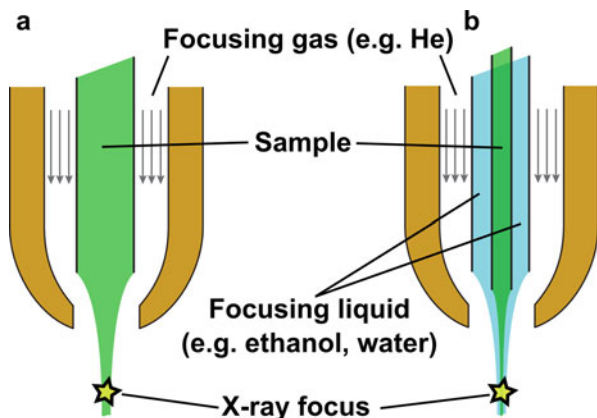


**Fig. 5.18** Comparison of GDVN (a) with a DFFN (b). The sample (usually suspensions of protein nanocrystals or microcrystals in crystallization buffer) is shown in green, the focusing/sheath liquid in blue. In a DFFN (b) the sample is injected into an accelerated focusing liquid jet. To achieve this the innermost capillary that delivers the sample protrudes out of the capillary that delivers the focusing liquid. (Figure by Dominik Oberthuer and licensed under a Creative Commons Attribution 4.0 International License)

sample is often limited and one strives to reduce the flow rate as much as possible under the counteracting constraint to retain a stable jet. In a normal GDVN, stable jetting conditions [87–89] are dependent on the flow rate of the sample at the given viscosity and surface tension, and are further affected by the high content of solids within the samples (crystals). Therefore the sample flow rate cannot be changed independently of the sample composition when using a GDVN. Moreover, changes between samples or between sample and buffer/water always require a short interruption of the jet. Jet interruptions can be highly undesirable, since it increases the risk of nozzle clogging in general but especially in vacuum. Using a DFFN instead of a GDVN thus results in a decreased clogging risk and a decrease in sample consumption, both making experiments more efficient.

It should be noted though that for both GDVN and DFFN, air bubbles in a not properly loaded sample can cause severe problems. These air bubbles are compressed in the pressurized sample delivery system and expand once the pressure drops at the outlet of the nozzle, resulting in jet interruption and splash-back of sample to the nozzle tip. The sheath liquid of the DFFN cannot prevent this from happening and it is thus of extreme importance to load the sample properly and as gas free as possible, even when using a DFFN. The outer/sheath liquid of a DFFN can be almost freely chosen, as long as it is miscible with the sample buffer. Liquids immiscible with the sample buffer lead to severe jet instabilities and thus impair successful serial crystallography experiments [23]. For all liquids miscible with the aqueous buffers used for crystallization of biological macromolecules, one has to consider their viscosity and surface tension, since—at a given nozzle geometry—these two parameters are most important for determining jetting conditions [87–89].

The focusing liquids should be non-toxic, contain no impurities and be available at low cost and large quantities. For X-ray background considerations they should consist of mostly low-Z atoms. Ideal in this respect are short alcohols, such as ethanol or 2-propanol. In some cases interference of the sheath liquid with the buffer upon slow diffusive mixing of the two co-flowing liquids poses a problem. This has been seen recently in the case of high concentrations (>500 mM) of sulfate-anions in the buffer where the immediate formation of salt crystals at the contact area to the alcohol sheath leads to clogging of the nozzle. In those cases other sheath liquids such as ultrapure water can be used. Sheath flow rates for a stable jet are slightly higher for pure water than for ethanol or 2-propanol, due to different viscosities and surface tensions, thus using water as a sheath liquid results in higher X-ray background due to a larger jet diameter. At the same sheath liquid flow rates, ethanol yields a slightly higher hit-fraction (fraction of X-ray pulses that interact with a protein crystal) than water [23]. Moreover for the case of injection into vacuum, the lower freezing point of the short alcohols compared to water effectively prevents the freezing and icing problems—both from the nozzle tip and from the sample catcher. Since the formation of ice in vicinity of the X-ray interaction point poses a big risk for the detectors (death by Bragg-reflection), the use of a DFFN with sheath liquids, primarily alcohols, can increase the lifetime of the very expensive detectors. Furthermore, the use of DFFN essentially eliminates ice or solidified desiccated sample growing from the catcher or the shroud used to contain the sample, which in most cases requires venting of the chamber, leading to interruptions of the experiment and less efficient use of the beamtime available.

### 5.5.2.2 Development of DFFN

Double flow focusing in combination with gas dynamic virtual nozzles (GDVN) was first reported by Gañán-Calvo et al. [86] in 2007. In this paper they investigated double flow focusing using simple (non-biological) liquids, in which the sheath liquid was immiscible with the central liquid. The goal of their research was the development of ultra-thin (sub-micron diameter) jets for biotechnology and medical applications. They achieved double flow focusing by placing a capillary within a manifold capillary and positioned the inner capillary such that its tip extended out of the manifold capillary by about one capillary diameter. The sheath flow was gas focused through a round orifice within a plate [86]. This nozzle design cannot be used for serial crystallography, since the aperture plate would be too close to the X-ray interaction point and it would block the scattered X-rays on the way to the detector. In a second approach, Wang et al. [33] adapted this design and integrated it within a GDVN design typically used for serial crystallography experiments to create a nozzle for mix-and-diffuse [90] time-resolved experiments. To achieve mixing they made a nozzle with a retracted inner capillary in order to inject the sample into an outer flow containing a ligand. Due to the retracted inner nozzle, the sample is injected into the unfocused outer flow. The sample solution is focused to a smaller diameter by the sheath liquid, which flows at a higher speed. The focused

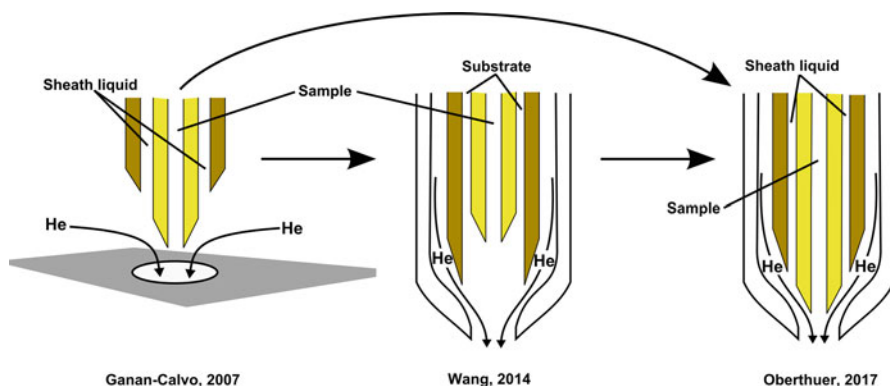


**Fig. 5.19** Evolution of double flow focusing nozzles. The first double flow focusing GDVN, presented by Gañán-Calvo et al. in 2007, had no outer glass capillary for the focusing gas. In 2014 Wang et al. repurposed the double flow focusing idea to make a microfluidic mixer for time-resolved crystallography. The DFFN successfully tested and used for serial femtosecond crystallography experiments at LCLS [23] combined the protruding innermost capillary introduced by Gañán-Calvo with the outer glass capillary from the design by Wang. (Figure by Dominik Oberthuer and licensed under a Creative Commons Attribution 4.0 International License)

sample and sheath liquid flow co-axially and mix through laminar-flow diffusive mixing. The homogenized mixture of sample and ligand would then be focused and accelerated together into a single jet, with crystals ideally being aligned in the center, to get a large hit fraction and a homogenous time delay. It has been shown with fluorescence imaging that mixing can be achieved with such a nozzle. However the parameters for successful mixing (ratio of flow rate<sub>ligand</sub>–flow rate<sub>sample</sub>) again impaired [91] its use for serial crystallography experiments. For the DFFN, both approaches have been combined (see Fig. 5.19 for a comparison) where a similar gas-focusing layout is used as in Wang et al. [33] and a capillary arrangement with the inner capillary protruding out of the outer capillary as in Gañán-Calvo et al. [86]. This design avoids diffusive mixing and creates a stable double focused jet. Initially sheath liquids immiscible with the aqueous buffers were used. With sheath liquids such as n-decane, n-hexane, and ethyl acetate, double flow focusing at low flow rates could be achieved and detected with fluorescence imaging.

### 5.5.2.3 Use of DFFN at LCLS

A challenge for any experiment at X-ray FELs is the interface of the sample delivery device with the experimental chamber (if) under vacuum. For liquid jets this can be facilitated by a load lock through which nozzles that are attached to a long pipe (nozzle rod) can be exchanged without the need to vent the vacuum chamber (see Sect. 5.2). There have been approaches to decouple nozzle exchange from the use of the nozzle rod, but this requires hardware to be installed within the

experimental chamber [92] and is challenging for short beamtimes such as Protein Crystal Screening (PCS) experiments. The biggest disadvantage of the nozzle rod is its narrow inner diameter. All liquid and gas lines have to go through this rod and have to be connected in such a way that it is compatible with the vacuum environment within the experimental chamber. For normal GDVN this is not a problem: liquid line and gas connection are put in place in a small metal tube using epoxy-glue and sealed with standard HPLC-fittings [79] to a connector to the nozzle rod. For the double flow focusing nozzle, the central sample capillary must be embedded into the sheath liquid line. In the proof-of concept experiments, embedding of the capillary was achieved using a standard HPLC T-connector. The diameter of this connector however is too large for the typically used nozzle rod. Therefore, an injector was designed that is compatible with the experimental setup. The injector connects directly to the lower end of the nozzle rod and all fluid lines are arranged to form a DFFN. The design was mostly restrained by the diameter of the differential pumping tube in use at the time, through which the nozzle rod is inserted into the load lock and vacuum chamber. The first custom built DFFN injector used at LCLS can be seen in Fig. 5.20a, b. It was subsequently improved, slightly miniaturized and its production automated through metal 3D-printing (sintering) techniques (Fig. 5.20c). These DFFN were successfully tested at CXI/LCLS and it could be demonstrated that (a) much lower sample flow rates are possible (5 vs 30  $\mu\text{L}/\text{min}$ ), (b) the jet is very stable and the X-ray background is lower than for jets from a GDVN, (c) sample change is possible without stopping the jet, (d) no ice formation/debris formed on the nozzle tip, (e) no ice/debris grows back from sample shroud/catcher and (f) the nozzles run a long time without clogging. Almost all of the challenges described above for GDVNs could be addressed with the use of a DFFN, and it was now possible for the first time to obtain enough diffraction data to solve the room temperature structures of RNA polymerase II and a dioxygenase [23].

### 5.5.3 From Art to Science: 3D Printed Nozzles

One challenge not tackled by the DFFN design described above was the low reproducibility of the handmade nozzles, that is, the quality of the assembly of capillaries and outer glass piece strongly depends on technical experience and craftsmanship. Ideally the nozzles would be mass-produced and all nozzles would have the same jetting properties. Moreover, there should be a certain flexibility of design to accommodate the diversity of possible experiments and sample buffers. Both requirements are met by rapid-prototyping technologies, and early attempts used PDMS-based soft lithography [93]. However, even with the use of microfluidic device fabrication technology, the nozzle quality still strongly depends on the capabilities of the technician and again not every nozzle of one batch is the same. Recently 3D-printing technology [94] with submicron-accuracy was introduced, and such accuracy enables the design, rapid prototyping and production of nozzles

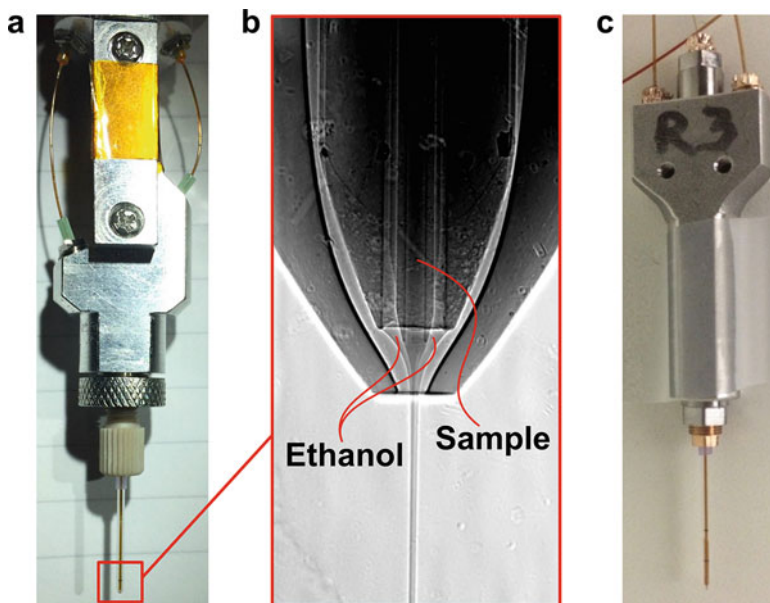


**Fig. 5.20** Double flow focusing nozzles used at LCLS. During the first successful experiments with DFFN at LCLS a nozzle body as shown in (a) was used. It was machined from pieces of bronze and steel. In (b) an X-ray radiograph (beamline P05/PETRAIII, Deutsches Elektronen-Synchrotron, DESY and Helmholtz-Zentrum Geesthacht, HZG) reveals a detailed view of a DFFN. 4 M potassium iodine solution (“sample”) is focused by ethanol, which is being focused to a jet by helium gas. A second generation DFFN, produced by metal 3D-sintering is shown in (c). All injectors consist of inner line for sample, sheath liquid line, and focusing gas line. They can be mounted to the standard “nozzle rod” at the CXI endstation of LCLS using an adaptor piece or easily in other atmospheric pressure instruments at existing X-ray FELs. The second generation can be operated without this adaptor piece when mounted to other instrumentation such as a goniometer. The position of the inner capillary relative to the gas orifice of the nozzle and the end of the sheath-liquid capillary can be adjusted by a screw, to optimize jetting conditions. (Figure was adapted from Oberthuer, D. et al. Double-flow focused liquid injector for efficient serial femtosecond crystallography. *Sci Rep* 7, 44628 (2017) and is licensed under a Creative Commons Attribution 4.0 International License)

for serial crystallography. Nelson et al. reported the first 3D-printed GDVN and its use in serial crystallography experiments at LCLS [32]. The nozzles were designed using a CAD-program and printed with a Photonic Professional GT (Nanoscribe, Germany). One disadvantage of this technology is that the high resolution of printing comes at the price that only small volumes can be printed within a reasonable time frame. While the actual nozzle tip and the fluidic channels are small enough, the fluid connections to the sample reservoir and the lines for the focusing gas pose a challenge. In the future there might be possibilities to directly print the nozzle tip onto connecting lines. However Nelson et al. used a different approach in their work [32]. They printed the nozzle wide enough such that a sharpened fused glass capillary could be glued to the sample channel and the whole nozzle-

capillary assembly was then glued to a larger glass capillary, which in turn forms the connection to the gas line. This still requires a certain set of manufacturing skills, but the critical parts for jetting, the geometry of the nozzle tip (gas orifice diameter, distance of capillary tip to orifice, angle of outer capillary) are 3D-printed and thus independent of the manufacturer. Each nozzle design can now be printed, processed using developed protocols and tested. The feedback from testing is in turn used to evolutionarily optimize the nozzle design.

### ***5.5.4 Development of Mixing Injectors for Time-Resolved Studies***

Liquid jet injection can be combined with a variety of triggering methods for time-resolved serial crystallography [95–98] (see Chaps. 11 and 12). For light-activated processes [66, 82, 83, 99], GDVN and DFFN nozzles can be used as is, or slightly modified with an opaque coating on the liquid lines to avoid pre-activation through stray light. For the study of chemically activated processes (e.g., enzyme-catalyzed reactions) the nozzle needs to be combined with a mixing device (mix-and-diffuse approach [90]). In the mixer the sample under investigation is mixed with a chemical compound that binds to the sample and triggers a response in the sample. Mixing should occur fast and in a controlled way throughout the whole crystal, which requires crystals smaller than 10  $\mu\text{m}$ , since reduced size decreases the diffusion time of the substrate into the crystal. Over the years various microfluidic mixing technologies have been developed for studies with proteins in solution [100–104]. For serial crystallography these need to be adapted to the special case of a thick microcrystalline slurry at high salt content and at times high viscosity. Wang et al. [33] reported a first mixing nozzle (see Fig. 5.19) for serial crystallography that was not suited for actual serial crystallography experiments due to the required high dilution factor of the sample, which would lead to very low hit rates. Another approach by Trebbin et al. [93] is based on PDMS soft lithography and has the mixer integrated with the nozzle in a double-flow architecture similar to that of Wang et al. A clear advantage is the design flexibility of PDMS in comparison to the limitations of a manifold of fused silica fibers. Thus it should be possible to achieve sufficiently short time delays for many enzyme reactions at acceptable hit-fraction using PDMS based mixing nozzles. In the first two successful mix-and-diffuse experiments at LCLS [84, 85] longer time delays were probed and thus a simple T-mixer introduced into the sample line more than 1 m upstream of the X-ray interaction point could be used. Calvey et al. [91] presented a more sophisticated mixing nozzle for shorter and more defined mixing time points (see Fig. 5.21). The glass-based nozzle with integrated mixer is inspired by the double-flow design of Wang et al. [33] and is improved such that fast mixing can be achieved at a better ratio of ligand–sample (from 2000:1 to 30:1) [91]. This dilution of sample can still be tolerated in respect of the expected hit-fraction during an experiment at LCLS or SACLA. The resulting

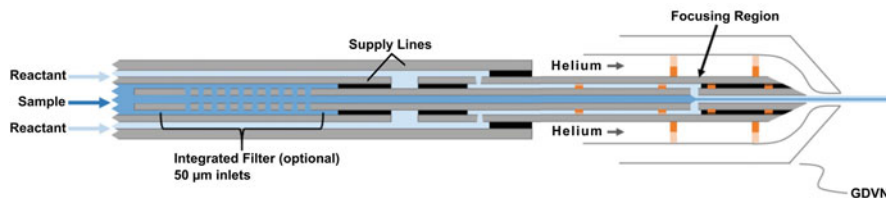


**Fig. 5.21** Advanced flow focusing mixing nozzle. In the focusing region sample and reactant mix through laminar flow diffusive mixing. The reacting mixture is then accelerated by Helium, just as in a normal GDVN. The distance between the focusing region and the acceleration region and the flow rates of sample and reactant define the time-delay to be probed. (Figure was adapted from Calvey, G.D., Katz, A.M., Schaffer, C.B. & Pollack, L. Mixing injector enables time-resolved crystallography with high hit rate at X-ray free electron lasers. *Structural Dynamics* 3, 054301 (2016) and is licensed under a Creative Commons Attribution 4.0 International License)

reduction in hit-fraction is even less than  $1/30$ , if it is considered that the design leads to a focusing of the sample stream and that most crystals (if sufficiently small) can be expected to align with the flow, in a narrow channel near the middle of the jet.

### 5.5.5 Outlook

Many of the challenges in liquid jet injection have been addressed in the past years and a clear trend has emerged in moving away from manual assembly of nozzles towards automation. The inherent precision, accuracy, reproducibility and three-dimensional flexibility of modern 2-photon polymerization direct laser writing (2PP-DLW) techniques is—at least for now—the superior way to make GDVN. And there is no reason why the same techniques should not be employed to make DFFN and mixing nozzles. A combination of a 3D-printed DFFN with a mixer printed close to the nozzle tip should yield an excellent injection device for long sought time-resolved crystallography experiments at high spatial and temporal resolution of enzymatic reactions. These nozzles would be highly reproducible, they could be produced in large numbers in an automated fashion and they could easily be adapted to different experimental parameters. A combination of experimental evolutionary rapid prototyping and fluid dynamic simulations (as already described for the double-flow focusing nozzles [23] and recently for GDVN [105]) would yield the ideal nozzle for every sample and ligand-solution composition and desired time delays. Fluid-dynamic simulations, fluorescence imaging and UV-VIS-spectroscopy could be used to investigate the properties of the mixers and to optimize the mixing process, building up on years of experience with microfluidic mixers in other fields of science. The next step is now to develop methods for automated sample exchange to further reduce sample consumption and to integrate the sample reservoir close to the nozzle. A possible future operation mode of LCLS-II for hard X-rays at repetition rates of  $\gg 1000$  Hz, and the recently operational European XFEL, will

enable the collection of full data-sets (one static structure, one time point) in about a minute, in principle. Mass produced 3D-printed nozzles and automated sample exchange will need to be able to cope with this data-collection speed and will enable high-throughput and high-output structural biology of fascinating targets.

## 5.6 Highly Viscous Carrier Media and Droplet Injector

We describe two methods, a matrix carrier technique and droplet injection, for serial sample delivery at SACLA using X-ray free-electron lasers. The first is a high viscosity micro-extrusion injector, extruding viscous samples such as lipidic cubic phase (LCP), which has been installed at SACLA. The micro-extrusion technique was also employed with other highly viscous matrices as a crystal carrier, such as grease and oil-free hydrogel medium, for serial sample delivery, which allows the structure determination of a wide variety of proteins with low sample consumption, typically less than 1 mg. In the second method, a piezo-driven droplet injector that delivers single drops containing crystals to synchronize with individual X-ray pulses was developed.

### 5.6.1 Serial Sample Delivery at SACLA

Serial femtosecond crystallography (SFX) [3, 67, 76, 78, 106] using XFELs has the potential for structure determination by collecting diffraction signals up to a few angstroms in resolution, even from submicrometer-size crystals. This has greatly improved the understanding of the room temperature structures of proteins [22, 40, 46, 48, 77, 107–110], and offers new opportunities for time-resolved studies of light-driven structural changes and chemical dynamics [80, 83, 111–114]. A single-pulse X-ray exposure will completely destroy small individual crystals; therefore, fresh specimens must be supplied for subsequent X-ray pulses to continue data acquisition. Liquid jet injection of small protein crystals using a gas dynamic virtual nozzle (GDVN) is often exploited for serial sample delivery [13]. The GDVN can provide fundamental and crucial insights in double-focusing mixing jet (liquid mixing jet) experiments in SFX to study the real-time enzyme-substrate interactions as well as reactions [33, 85, 91]. In the SFX research at SACLA (the SPring-8 Angstrom Compact Free Electron Laser), a liquid jet injector was installed into the experimental instruments of the DAPHNIS (Diverse Application Platform for Hard X-ray Diffraction in SACLA) system, which basically consists of a sample chamber, fluid injectors and a two-dimensional detector [39]. Continuous flow at a relatively high speed ( $\sim 10$  m/s) and high flow rate results in 10–100 mg of protein used, that is, the amount of sample consumption for structure determination is significant. Moreover, due to the high speed of the jet, the liquid-jet injectors may not be ideal for X-ray FELs with low repetition rates (e.g., 30 or 60 Hz at SACLA), because

most of the sample is wasted between X-ray pulses. In addition, the implementation is complicated by a variety of factors, including difficulties imposed by viscous solutions and unpredictable trajectories of drops that contain crystals of varied shapes and sizes. For membrane proteins, a lipidic cubic phase (LCP) injector with a low flow rate was developed by Uwe Weierstall and coworkers at Arizona State University [45]. However, a more universal method for serial sample delivery that is applicable to a wide variety of soluble and membrane proteins is essential to firmly establish the SFX method, because the LCP micro-extrusion technique is generally limited to membrane proteins crystallized in LCP or crystals that do not dissolve when mixed with LCP. We have since introduced mineral oil-based grease as a protein carrier in SFX [40]. We originally developed an LCP injector consisting of a hydraulic cylinder, a removable sample reservoir, and a nozzle using the same basic concept of the LCP injector as reported by Weierstall et al. Using the LCP injector, the sample injection method with viscous media is technically simple. Micro-extrusion of specimens using a viscous media such as LCP [45], grease [40, 115, 116], Vaseline (petroleum jelly) [41], agarose [42], hyaluronic acid [115], or hydroxyethyl cellulose [116] can maintain a stable stream at a low flow rate of 0.02–0.5  $\mu\text{L}/\text{min}$ , which helps to reduce sample consumption to less than  $\sim 1$  mg. At SACLA the sample injection method with viscous media is mainly used for SFX as well as LCP-SFX. In addition, a piezo-driven droplet injector, that delivers single drops containing crystals to individual X-ray pulses, was developed for viscous-medium sensitive proteins [109]. We describe these two approaches for serial sample delivery here.

## 5.6.2 *Highly Viscous Carrier Media*

### 5.6.2.1 Grease Matrix

In protein X-ray crystallography, mineral oil is used as a cryoprotectant [117]. The mineral-oil based grease [40] provides protection against cracking and dissolution of protein crystals. The grease-matrix based approach is applicable to structure determination for a wide range of proteins at room temperature requiring less than 1 mg of the sample. The sample preparation in this technique can be performed by simply mixing crystals with a matrix medium (details described below in the Sect. 5.6.2.3). We have also introduced Super Lube synthetic grease (synthetic grease) [115] and Super Lube nuclear grade approved grease (nuclear grease) [116] to SFX, to reduce background scattering commonly observed with mineral-oil based grease. Weaker background scattering was noted when using nuclear grease compared with other grease matrices. To date, the adaptability of grease matrices in SFX has been demonstrated at SACLA using a wide variety of soluble and membrane proteins: lysozyme, glucose isomerase, thaumatin, fatty acid-binding protein type 3 or proteinase K [40, 115, 116, 118], copper nitrite reductase [107], photosystem II (PSII) [114], luciferin-regenerating enzyme [119],

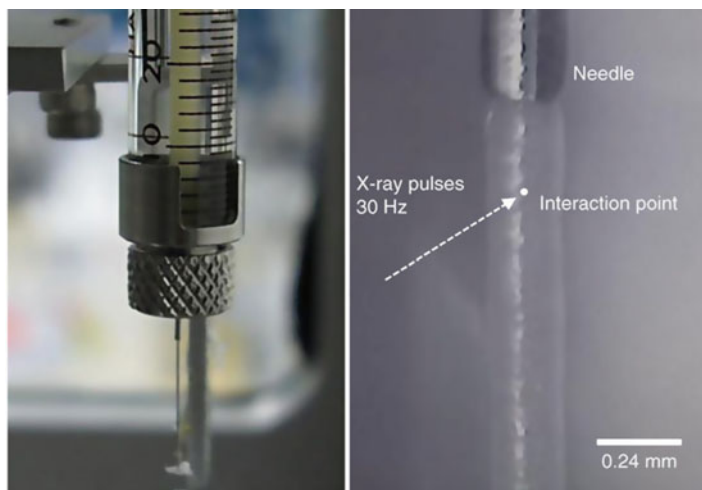


**Fig. 5.22** (left) A 100  $\mu\text{L}$  commercial glass syringe (Hamilton), is shown extruding samples mixed into a grease matrix. (right) A zoomed image of the interaction region with X-ray interaction region labeled. Modified with permissions from Sugahara et al. [40]

the photoswitchable fluorescent protein IrisFP [120], bacteriorhodopsin [121], and bacterial phytochrome [122]. These results suggest that grease has potential as a versatile matrix carrier. Figure 5.22 shows the simplicity of the extrusion, as it utilizes many commercial components and needs minimal customization.

### 5.6.2.2 Hydrogel Matrix

In spite of its versatility, dissolution of crystals in soluble and membrane protein samples in the grease matrix is occasionally observed. In addition, the grease media tends to produce stronger X-ray scattering in the resolution range of 4–5  $\text{\AA}$ , which increases the noise level. A new crystal carrier with low background scattering (e.g., agarose [42]) is essential to improve the signal-to-noise ratio. Recently, hyaluronic acid [115] and hydroxyethyl cellulose matrices [116] were introduced for SFX experiments at SACLA. The hydrogel matrices have lower background scattering compared to the diffuse scattering generated by a grease matrix in the resolution range of 4–5  $\text{\AA}$ . There are no significant differences of the background scattering between hyaluronic acid and hydroxyethyl cellulose matrices. The usability of hydrogel matrices was confirmed for all oil-sensitive crystals that were tested. The hyaluronic acid and hydroxyethyl cellulose matrices provide alternative choices for grease sensitive protein crystals. The hydroxyethyl cellulose matrix is less adhesive than the hyaluronic acid matrix and prevents clogging of the suction tube used as a sample catcher [41] and also prevents adhesion of the matrix to the injector nozzle surface. Using the hydroxyethyl cellulose matrix, the proteinase K crystal structure

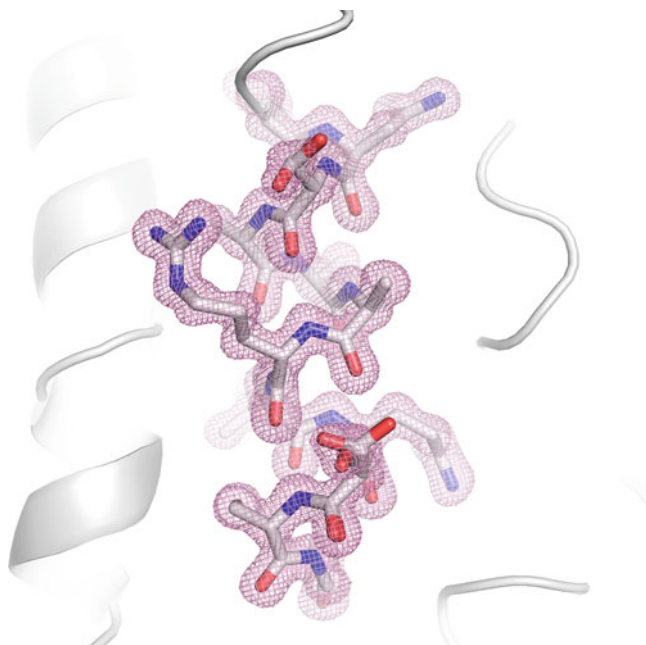


**Fig. 5.23** A close-up view of the proteinase K from *Engyodontium album* at 1.20 Å resolution with a  $2F_o - F_c$  electron-density map contoured at the  $1.5\sigma$  level. Reproduced with permissions from Masuda et al. [123]

was determined at 1.20-Å resolution (Fig. 5.23) [123]. A total of  $\sim 82,000$  indexed patterns were collected at 13 keV photon energy. This atomic resolution structure clearly allows for visualization of the hydrogen atoms forming hydrogen bonds in secondary structures.

### 5.6.2.3 Matrix Preparation

In the matrix technique using viscous media, the first step is to find a carrier for the protein crystals of interest that is suitable for data collection at room temperature. In SFX, a grease or hydrogel matrix may not always be useful, because some proteins are damaged while being mixed and soaked in these media. Viscous media tends to cause cracking and dissolution of protein crystals due to various physical or chemical events, such as osmotic shock arising from the properties of the viscous media. Grease has potential as a versatile matrix carrier, but the hydrogels, such as hydroxyethyl cellulose and hyaluronic acid matrices, would enable SFX experiments for grease-sensitive protein crystals or data collection with low background scattering. Grease and hydrogel crystal carriers are therefore complementary.

To maintain a continuous sample column, a grease matrix is typically created as a grease and crystal solution in a ratio of 9:1 (v/v). As an example, after a 100- $\mu\text{L}$  sample of crystal solution (e.g., a crystal number density of  $\sim 10^7$  crystals/mL) is centrifuged, a 90- $\mu\text{L}$  aliquot of supernatant solution is removed. A 10- $\mu\text{L}$  aliquot of the crystal solution is dispensed into 90  $\mu\text{l}$  of grease on a glass slide and then mixed.

The hydrogel concentration is ideally  $\sim 10$  to 20% (w/v). The hydrogel (hydroxyethyl cellulose or hyaluronic acid) solution is saturated with the crystal harvest solution, or the supernatant solution from the crystal suspension solution can be used for the protein crystals. As an example, after a 100- $\mu\text{L}$  sample of crystal solution is centrifuged, a 90- $\mu\text{L}$  aliquot of the supernatant solution is removed. A 10- $\mu\text{L}$  aliquot of the crystal solution is dispensed into 90  $\mu\text{L}$  of a  $\sim 16\%$  (w/v) hydroxyethyl cellulose solution on a glass slide and then mixed with a spatula. In some cases, a hydrogel aqueous solution (without buffer) acts as a matrix. However, optimizing the hydrogel solution buffer is important to avoid potential osmotic shock to the crystals after mixing with the medium.

Dehydration of protein crystals can be induced during the sample preparation process of the water-free grease matrix. The unit-cell axes of the lysozyme crystals for the grease matrix are slightly shorter than those for the hyaluronic acid matrix [115]. In such cases, a water-based hydrogel medium can be helpful for preventing the contraction of the unit cell in SFX experiments. Although the medium mixing technique using a syringe coupler may prevent crystal dehydration [42, 124], the technique may cause mechanical damage to brittle crystals by the physical contact between crystals and the interior surface of the coupler, resulting in the deterioration of diffraction quality. Simple and quick mixing with a spatula on a glass slide [40] would be better for brittle crystals.

#### 5.6.2.4 Matrix Extrusion

An increase in the hit rate can be accommodated with increased crystal number densities, which could, however, cause multiple sample hits in one shot and complicate the indexing procedures. A crystal number density of  $\sim 10^7$  and  $\sim 10^8$  crystals/mL is suitable for SFX data collection under reported experimental conditions using  $\sim 100$ - and  $\sim 50$ - $\mu\text{m}$ -i.d. nozzles, respectively. For micro extrusion of the matrix, a sample column with a smaller diameter contributes to reducing sample consumption and background noise from the matrices. The conventional grease matrices (mineral-oil based grease [40] and synthetic grease [115]) extruded through a 110- $\mu\text{m}$ -i.d. nozzle tended to produce a larger-diameter grease column (approximately  $\sim 210$   $\mu\text{m}$ ) about the size of the outer diameter (o.d.) of the nozzle. On the other hand, the nuclear grease and the  $\sim 16\%$  (w/v) hydrogel matrices are extruded as a continuous column with a diameter of  $\sim 100$   $\mu\text{m}$  through a 100- $\mu\text{m}$ -i.d. nozzle.

From  $\sim 30$   $\mu\text{L}$  of protein crystals (size 5–30  $\mu\text{m}$ , crystal number density  $\sim 10^7$  crystals/mL) dispersed in a matrix, a total of  $\sim 20,000$ – $30,000$  indexed patterns were

typically recorded (indexing success rate  $\sim 30\%$ ) within 1 h at a 30 Hz repetition rate and a flow rate of  $\sim 0.5 \mu\text{L}/\text{min}$  through a 100- $\mu\text{m}$ -i.d. nozzle. When the matrix is passed smoothly through a 50- $\mu\text{m}$ -i.d. nozzle a reduced flow rate as low as  $0.1 \mu\text{L} \text{ min}^{-1}$  is sufficient for the 30-Hz operation. We were able to substantially lower sample consumption, using only  $\sim 0.2 \text{ mg}$  of the sample instead of  $\sim 1 \text{ mg}$  with a 100- $\mu\text{m}$ -i.d. nozzle.

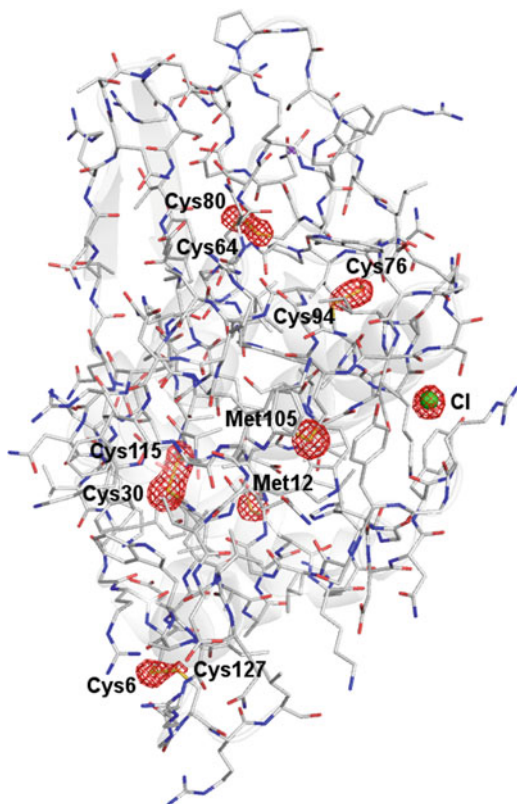
### 5.6.2.5 De Novo Phasing

For the de novo phasing of macromolecules, experimental phasing has been mainly performed on heavy-atom derivatives of protein crystals [63, 107, 116, 119, 121, 125–127]. Using the grease matrix the phasing was successfully performed by Hg-SIRAS (single isomorphous replacement with anomalous scattering) [119], Cu-SAD (single-wavelength anomalous diffraction) [107] and I-SAD [121] at SACLA. Additionally, the de novo structure determination of proteinase K from Pr-derivatized crystals was demonstrated using hydroxyethyl cellulose matrix [116]. In total, 2000 images (native/derivative: 1000/1000) were sufficient for SIR and SIRAS phasing of proteinase K, while SAD phasing required 3000 images. For SFX, native sulfur SAD phasing was also successful [50, 118, 127]. Using the grease matrix, the structure of native lysozyme was determined with SAD by utilizing the anomalous signal of sulfur and chlorine (Fig. 5.24) [118]. Native SAD phasing was successfully demonstrated using femtosecond X-ray pulses at 1.77 Å wavelength using 150,000 indexed patterns to 2.1 Å resolution. These results demonstrate that de novo phasing can now be used for SFX. However, SFX requires a higher volume of crystals and many hours of beam time for a large degree of data redundancy to effectively utilize the relatively weak anomalous signal. One of the major challenges for phasing in SFX is to improve the signal-to-noise ratio. Techniques using matrices with low background scattering noise will contribute significantly to the measuring of weak anomalous signals for de novo phasing from SFX data.

### 5.6.2.6 Other Applications

Room-temperature measurements enable time-resolved studies and eliminate the need to find a suitable cryoprotectant; however, in time-resolved experiments, the sample consumption is significant. Matrix carriers with a stable sample flow and low sample consumption should be applicable for time-resolved studies using pump–probe techniques. The structural changes of photosystem II (PSII) induced by 2-flash (2F) illumination at a resolution of 2.35 Å have been demonstrated using the grease matrix techniques and femtosecond X-ray pulses from SACLA at BL3 [114]. Matrix carriers have various applications in SFX experiments, such as femtosecond to millisecond time-resolved studies of light-driven structural changes, and chemical dynamics using pump–probe techniques.

**Fig. 5.24** Anomalous difference Fourier map (contoured at  $6.0\sigma$ ) calculated by ANODE [128], showing sulfur and chlorine atoms. Reproduced with permission of the International Union of Crystallography [118]



Synchrotron-based serial crystallography data collection at room temperature using viscous carrier media has been repeatedly demonstrated in recent years [41, 52, 129]. In the immediate future, sample delivery techniques using a viscous medium that help reduce sample consumption will become more important in serial millisecond crystallography using synchrotron radiation. It is valuable to provide a wide repertoire of carrier media for a wide variety of proteins, but a versatile carrier medium would be preferable.

### 5.6.3 Droplet Injector

#### 5.6.3.1 Introduction

The microcrystal extrusion technique using highly viscous carrier media allows the collection of a complete dataset from less than 1 mg of protein. While the technique has an advantage for sample delivery, highly viscous carrier media are prone to breaking protein crystals due to the physical shock during mixing or by chemical

damage. Some viscous media, such as grease and lipids used in LCP, produce intense X-ray scattering, resulting in high background noise that is likely to affect very weak signals such as resulting from small structural changes in a time-resolved SFX experiment.

To address these issues, another sample delivery method that utilizes pulsed liquid droplets was developed [109]. It has been noted that it is difficult to maintain synchronization of droplets loaded with microcrystals at the higher repetition rate of X-ray laser pulses such as LCLS, which fires at 120 Hz [130]. On the other hand, the X-ray FELs at SACLA fire at a maximum repetition rate of 60 Hz, so it is not necessary to continuously supply microcrystal samples to the intersection point, which allows for discontinuous sample delivery synchronized to the beam.

The experiment demonstrated protein microcrystals in a crystallization buffer ejected from a piezo-driven droplet nozzle as a pulsed liquid droplet, controlled in time and space, resulting in synchronization to XFEL pulses at 30 Hz. In this sample delivery method, microcrystals can be introduced in a pulsed manner, which reduces sample consumption compared to the continuous sample delivery. Since the method does not require additive materials such as lipids or oil, the background noise is lower than that from oil-based viscous media.

### 5.6.3.2 Droplet Injector Configuration

The droplet injector basically consists of a piezo-driven nozzle, a sample reservoir, a pressure controller (SF-100S, Microjet Inc.), and an electric pulse generator (IJK-200H, Microjet Inc.) (Fig. 5.25). The pressure controller is used to adjust the pressure on the loaded sample solution to keep the meniscus at the nozzle tip in an optimum position. The electric pulse generator provides pulsed voltages to a piezoelectric element in the nozzle at the same repetition rate as the X-ray FEL. The optimum amplitude and duration of the electric pulse (V and  $\Delta t$  in Fig. 5.25) changes depending on the samples used. Parameters of 80–100 V and 30  $\mu\text{s}$  were used for an SFX experiment with lysozyme crystals, as described below. The timing of the electric pulse for droplet ejection is controlled by a delay generator (DG645, Stanford Research Systems Inc.) that is synchronized to the X-ray FEL pulses. Droplets from the nozzle are monitored by using a CCD camera (IPX-VGA120-LMCN, Imperx Inc.) with a strobe light.

### 5.6.3.3 Example of SFX Experiment Using Droplet Injector

The capabilities of the droplet injector were demonstrated using ca. 5- $\mu\text{m}$  lysozyme crystals suspended in buffer solution (1 M sodium acetate buffer (pH 3.0) and 10% sodium chloride). The injector was installed into a chamber in DAPHNIS [39] and consists of a piezo-driven droplet nozzle with an 80- $\mu\text{m}$  aperture (IJHDS-1000, Microjet Inc.). The droplet is basically spherical but at times slightly elongated with a diameter almost the same as that of the nozzle aperture (80  $\mu\text{m}$ ). Therefore,

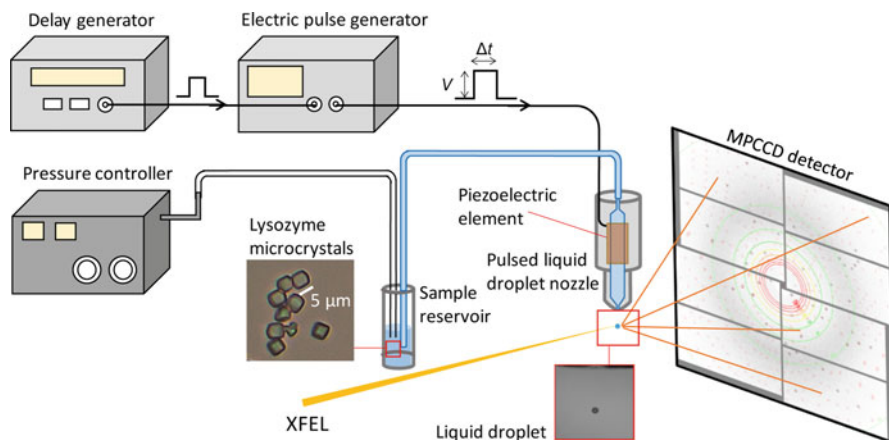


**Fig. 5.25** Experimental setup of SFX using droplet injector: pulsed liquid droplets containing microcrystals are ejected from a piezo-driven nozzle, to which a pulsed electric voltage is applied with an electric pulse generator. The droplets are introduced into a DAPHNIS chamber (not shown here), the inside of which is filled with helium. The timing and the position of the pulsed-droplet nozzle is adjusted with a delay generator and a motorized stage. Synchronization with XFEL is monitored with a CCD camera. Reproduced with permission of the International Union of Crystallography [109]

the sample flow rate was about 30  $\mu\text{L}/\text{h}$  when operated at 30 Hz. The sample solution in the reservoir was stirred vigorously to avoid any settling of the crystals due to gravity. The chamber was filled with helium gas to reduce air scattering. Also, the ambient conditions helped to prevent liquid droplets from freezing due to evaporative cooling at reduced pressure.

Fine tuning the sample delivery method in space and time is crucial for the droplets to overlap with the X-ray FEL pulses. The tuning was judged by the hit rate, which is defined as the number of images exhibiting more than 20 Bragg spots divided by the total number of images with the Cheetah software [131]. Using lysozyme crystals with  $3.2 \times 10^8$  crystals/ml, the hit rate fluctuated greatly between 14 and 93% for the first 30 min, while fine tuning of the liquid droplets in space and time was fully achieved. After that, diffraction images from the crystals decreased to 3% of the hit rate since the crystals precipitated in the tube connecting the nozzle and reservoir, due to the very slow flow speed. This issue can be solved by optimizing the configuration of the nozzle and reservoir. Also, it is possible to prevent crystals from settling by increasing the viscosity of the buffer solution. A stable injection of 5- $\mu\text{m}$  lysozyme crystals in a buffer solution with 10% polyethylene glycol 6000 was achieved, which is a relatively low concentration compared to a cryoprotectant. All combined, this allowed for structure determination of lysozyme at 2.3  $\text{\AA}$  from the SFX data obtained using the droplet injector.

Although the flow rate of 30  $\mu\text{L}/\text{h}$  was approximately 20 $\times$  lower than the typical flow rate of the liquid injector, it was still comparable with or higher than the

flow rates of the LCP injector [45] and the electrospun microjet [21]. The sample consumption of the droplet injector can be further reduced with smaller droplet size using a finer nozzle. A droplet nozzle with a 30- $\mu\text{m}$  aperture could provide droplets with a volume that is smaller by an order of magnitude, which could result in a decrease in the sample consumption, with an increased risk of clogging.

## 5.7 Acoustic Drop and Tape Drive

The previous section describes the generation of monodispersed droplet streams via piezoelectric triggers, synchronized with the SACLA FEL [109]. Roessler et al. [132] studied metalloenzymes with an Acoustic Droplet Ejector (ADE) where the drop generation was synchronized to the incident FEL pulses at 120 Hz using a pressure wave from an acoustic transducer to propel fluid away from a free liquid surface. The ADE allows the use of larger crystals (20–100  $\mu\text{m}$ ) with minimal clogging problems, since the crystals do not have to pass through a capillary with small inner diameter; however, sedimentation can be an issue, hence the inverted system seen in Fig. 5.26. The larger crystals sediment away from the free surface in the original modified commercially available Echo system from Labcyte, *up-shot*, configuration, whereas they sediment towards the free surface in the inverted, *down-shot*, configuration. The latter promotes more droplets generated with crystals inside.

While serial crystallography techniques continued to develop at X-ray FELs, many of the techniques began to return to bright synchrotron sources. Beyerlein et al. [133] performed a serial crystallography experiment at the P11 instrument of PETRA III in Hamburg, Germany. A brass chopper created 7.5 ms pulses at a frequency of 25 Hz, from the original  $10^{13}$  photons/second continuous synchrotron source. Figure 5.27 shows a slurry of crystals was sheared away from their free surface via a polyamide tape which subsequently carried them towards the X-ray focus ( $4 \times 8 \mu\text{m}$ ). The slurry of lysozyme crystals were mixed with chitotriose with 2 s and 50 s delays by varying the mixing junction geometry and position, liquid flow rates, and tape speed. The results indicate that room temperature structures of longer time point intermediates can be solved at a synchrotron using serial crystallography.

A combination of the ADE method and a belt system can provide increased versatility for pump–probe measurements. This has been demonstrated by Fuller and Gul et al. [134] in a study of the Kok cycle of photosystem II [135] with simultaneous collection of diffraction data and emission spectra from the water-splitting Mn cluster. The droplets are acoustically ejected, and deposited on a polyamide ribbon, which acts as a conveyor belt system. As the droplets progress on the tape, they pass through three laser illumination points, appropriately spaced to match the belt speed and desired timing. Finally, the belt passes close enough to the interaction region that the protruding droplet is hit by the fourth and final laser, followed by the FEL pulse; the X-ray pulse does not pass through the polyamide tape, thus not directly damaging the tape, instead it passes through the droplet parallel to the tape surface. Roughly, half of the forward scattering passes through

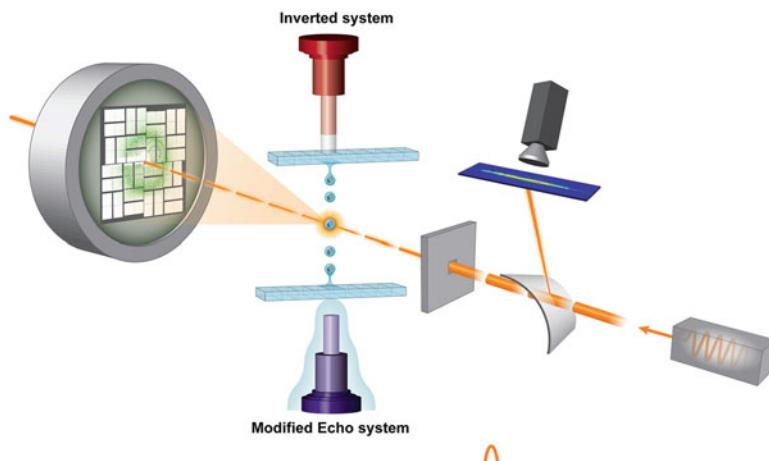


**Fig. 5.26** An acoustic transducer is coupled via an agarose plug to a sample well full of the protein slurry. The sample is ejected from the meniscus and tracked with an imaging system to receive the synchronized FEL pulse at 120 Hz at the LCLS. Two configurations are shown. The original *up-shot* configuration, modifies an Echo 555 system (Labcyte) to shoot a droplet upwards towards the X-ray focus, ideally carrying a crystal. To help create more sample-containing droplets, the inverted *down-shot* configuration is shown. Here the crystals sediment towards the liquid's free surface and are more likely to eject with the liquid. The two configurations are not concurrent and are simply overlaid into one schematic. Modified from Roessler et al. [132]

the belt, making a correction of the Bragg intensities in this area necessary. Bragg diffraction and emission data can be simultaneously measured from the sample within the droplet.

The optical pump can be replaced by a *reaction region*, seen in Fig. 5.28b. The entire Drop-On-Tape (DOT) system is in a helium enclosure to minimize air scatter. The reaction region can therefore be a smaller chamber, in which instead of pumping optically, another gas is flushed, such as oxygen, in order to study aerobic transients. The electronic structure of ribonucleotide reductase R2 was reported in the work, with and without the presence of oxygen.

The DOT system is versatile and can run up to 120 Hz, lower collection rates reported in the work were limited by the data detection devices rather than the sample or DOT's capabilities. The DOT has sample consumptions of 0.8–6 nL/shot depending on the crystal size, and thus the required sample droplets. Assuming a 120 Hz data acquisition rate, the sample consumption rates can be nontrivial: 5.8–43  $\mu\text{L}/\text{min}$ . These flow rates fall in line with common liquid injection rates used in the GDVN and DFFN.

An important distinction must be made about the droplet systems of this section when comparing them to the liquid jets of the prior sections: the synchronization is more efficient than the liquid delivery. The liquid jets travel at speeds of 10–100 m/s and thus have samples traverse the interaction region, but not necessarily when X-ray photons are present, whereas the synchronized systems have samples

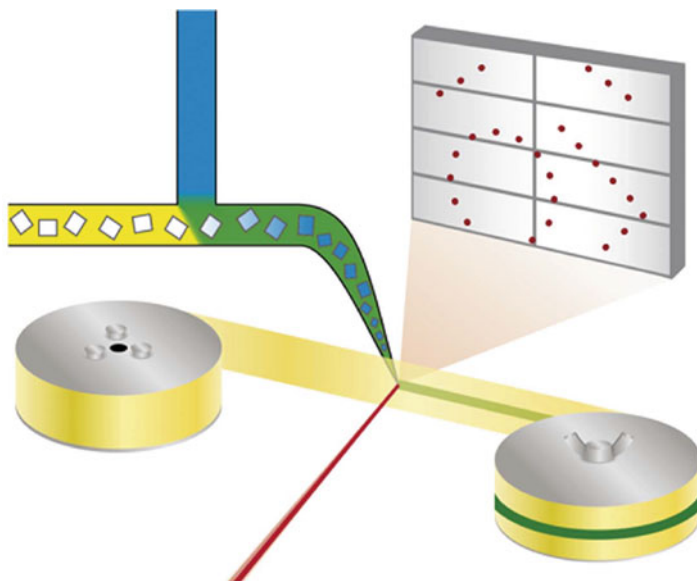


**Fig. 5.27** A polyamide tape passes in front of a chopped synchrotron beam (P11, PETRA III,  $10^{13}$  photons/s, 7.5 ms pulses every 40 ms, focused to  $4 \times 8 \mu\text{m}$ ). The X-ray photons (red) pass through the tape and sample and continue onto a beamstop (not shown) and detector. A commercial microfluidic tee-junction is used to introduce a slurry of lysozyme crystals (white blocks in yellow media) sheared onto the tape (green streak). An additional fluid containing a competitive inhibitor, chitotriose, was introduced (blue) and mixed (green media with blue soaked blocks) with 2 s and 50 s delays. Modified with permission of the International Union of Crystallography [133]

rarely present when no photons are present. Mentioned in the first section of the chapter, a successful sample delivery system will have a new sample present and an old sample removed in between incident pulses. This efficiency can be broken down further into how often the sample delivery mechanism can replenish a volume and how often is a replenished volume containing a sample, the former dictated by the delivery method while the latter is dictated more by the sample concentration. Crystals passing through a liquid jet can destabilize the liquid jet and cause the stream to fluctuate in and out of the X-ray focus, this combined with the particles concentration can lead to low data collection rates. More simply, the sample is concentrated enough but the jet is too unstable, or the jet is stable but the sample is not in high enough concentration or some combination of the two. Even when the data collection rate is *good*, the liquid jets are still wasting un-shot samples between pulses.

The synchronized nature of these droplet and tape systems [109, 132–134] mean that there is more sample delivery efficiency; for example, most of the 2 mL of sample delivered by a synchronized system will go towards the final solved structure, whereas a lower percentage of that volume is used towards the solved structure when using a liquid jet. High viscosity extrusions, for example, are more

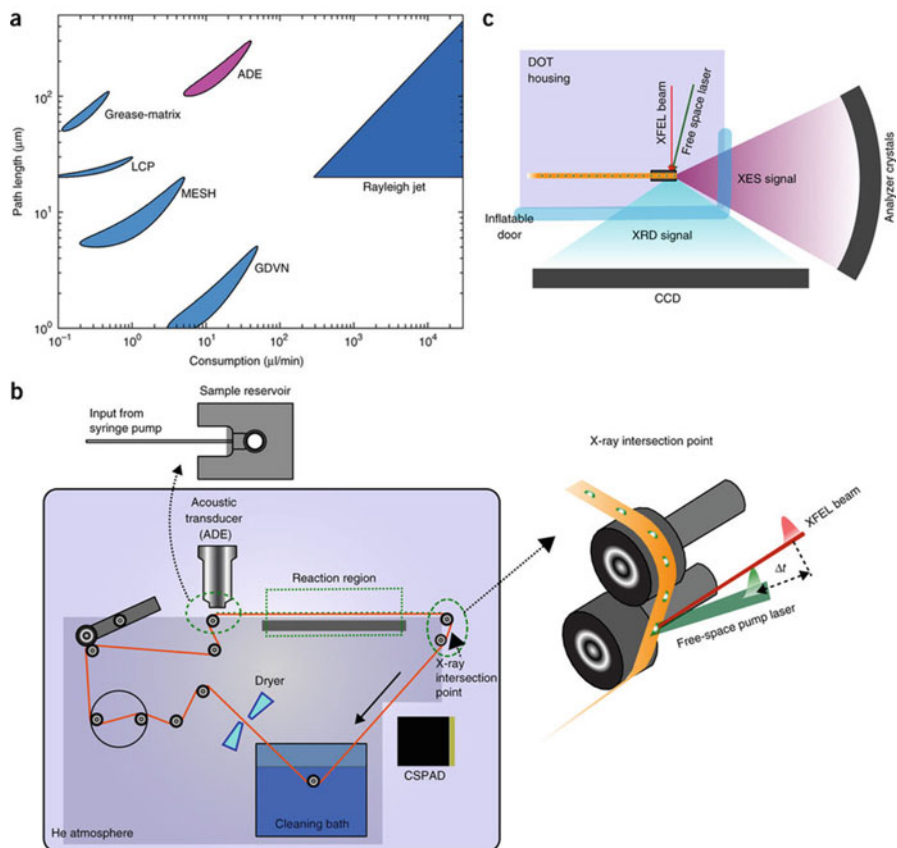


**Fig. 5.28** (a) Schematic showing the path length the X-rays typically need to traverse within a sample for different sample injection methods vs the sample consumption. Longer path length means larger crystals can be used. In the case of an ADE, the crystals can be large without having to pass through a small  $50\ \mu\text{m}$  orifice, while maintaining the sample consumption of a GDVN. (b) Schematic of a tape drive system where the drops pass through a large bore capillary towards the acoustic droplet ejector (ADE) and are deposited onto a polyamide tape. They pass through the reaction region, which can contain optically pump lasers or a liquid mixing stage, followed by the X-ray interaction region. A cleaning bath removes debris from the polyamide tape, which is then dried to be reused again. (c) The open geometry allows for simultaneous X-ray diffraction and emission spectra to be collected. Reproduced with permissions from Fuller and Gul et al. [134]

efficient than GDVN and DFFN, but still wasting un-shot sample between pulses. The tape drives rarely wastes sample between shots and mostly need to worry about particle concentration when trying to optimize one crystal per droplet. More dense slurries with larger crystals suspended, can lead to droplet instabilities and reduce the repeatable nature of the droplet streams as well as potentially lead to multiple crystals per droplet, complicating the data analysis.

These synchronized systems have only been demonstrated out of vacuum, because of their complexity to interface within vacuum, as well as the exposed liquid that would freeze in vacuum. This, however, can open the way to more complex experiments, such as time-resolved mixing with fluids and optical pumping with multiple pumps or with longer time delays than can be achieved with a jet. The sample consumption might not scale up to higher repetition rates as a droplet per pulse can be taxing at 1 MHz, but at 120 Hz repetition rate the consumption is still comparable to liquid jet methods, with the added advantage of more sample delivery efficiency and higher path length for signal starved approaches, such as X-ray emission spectroscopy.

## 5.8 Fixed Target Sample Delivery for SFX

The main idea of fixed target experiments is that samples, which are mounted on solid supports, are raster-scanned through the X-ray beam and thereby exposed to the X-ray FEL pulses as shown in Fig. 5.29. In order to achieve high hit rates, the sample support should ideally be periodically structured and present the samples at known and well-defined positions—the highest hit rate for single crystals if the sample is randomly distributed is 37% but the structured supports allow the approach to exceed the limit of the Poissonian distribution. A major challenge for fixed target experiments of biological samples is to protect the samples from drying out, which would result in a degradation of their diffraction properties.

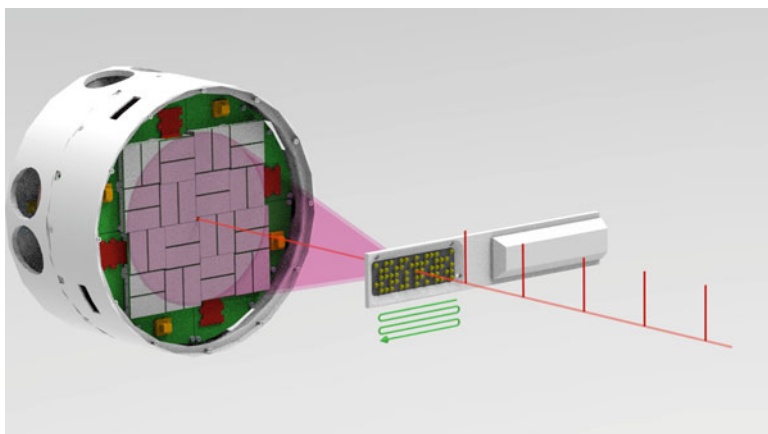


**Fig. 5.29** Scanning approach for fixed target serial crystallography experiments: The fixed target sample holder is raster-scanned through the X-ray beam and samples are exposed to the X-ray pulses at predefined positions. The resulting diffraction patterns are recorded with an integrating X-ray detector located behind the sample. The red delta functions in the above image represent the individual X-ray FEL pulses

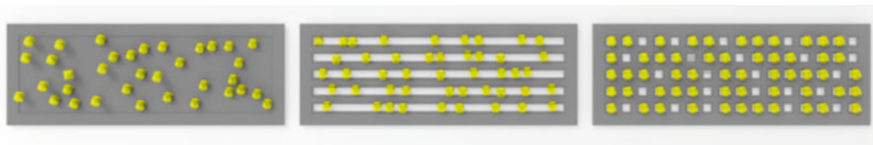


**Fig. 5.30** Three different categories of fixed target sample delivery approaches for SFX: (*left*) Samples are arbitrarily distributed on a flat membrane. (*center*) Microcrystals arrange themselves in one dimension according to the geometry of the substrate. (*right*) Micro-crystals arrange themselves in a 2 dimensional periodic fashion according the pattern of the micro-structured substrate. See Sect. 5.8.2 for more information

### 5.8.1 Types of Fixed Targets for SFX

Fixed target sample holders can be classified in three different categories as shown in Fig. 5.30: In the first approach the samples are arbitrarily distributed for example on a flat membrane [136, 137]. In the second approach the samples are arranged in a 1-dimensional periodic fashion as shown in Fig. 5.30 (*center*) which should facilitate higher hit rates compared to the first approach [138]. In the third approach samples are arranged in a 2D periodic fashion on a micro-structured sample holder, as reported by [138–141]. This approach should allow achieving the highest hit rates, as the samples are ideally all located at predefined position.

Different materials have been used as substrate materials for the solid supports, such as silicon nitride [136, 137], single crystalline silicon [140–142], and polycarbonate and other plastics [138, 139, 143, 144] (Cohen 2016).

The first fixed target SFX experiments at room temperature used a REP-24 microcrystal suspension that was mixed with Paratone-N, a mixture of hydrocarbons used as a cryoprotectant for traditional crystallography, to avoid dehydration of the sample [136]. The emulsion was applied as a thin film on thin silicon nitride membranes that spanned lithographically etched silicon crystals. The diffraction experiments were performed in the vacuum chamber of the CXI instrument at LCLS and they achieved a hit rate of 38.2% at an average data acquisition rate of 3 Hz resulting in a hit rate of about 1 hit/s. Unfortunately, the Paratone-N caused a large scattering background and the emulsion was challenging to apply to the fixed targets without damaging the supports. A similar approach was followed by Kimura et al., who performed X-ray FEL imaging experiments of living cells sandwiched between two silicon nitride windows [137].

Sample holders structured 1-dimensionally, in which the crystals are located in channels with a width of 20  $\mu\text{m}$  and a length of about 100  $\mu\text{m}$  have been used as a support. In this case the windows were etched into a 15  $\mu\text{m}$  thick photoresist layer located on top of a 150 nm silicon nitride membrane [138]. The solid supports are sealed on both sides with Kapton foil to prevent the crystals from drying out.

Sample holders structured 2-dimensionally were first used at an X-ray FEL by using larger crystals at cryogenic temperatures in a similar way to conventional

synchrotron data collection [139]. The sample holders used in their experiments provided space for about 50 crystals and were made from a low-Z polymer.

Sample holders structured in 2D with very fine structures (micro-structured) on silicon can be the basis for serial data collection and provide space for several hundreds to hundreds of thousands of crystals. They were first introduced for synchrotron experiments [141]. In this design, crystals are located in individual compartments of a silicon mesh structure ('silicon chip') with both sides of the chip sealed with Kapton foil to prevent the crystals from drying out. The chip is designed for room temperature experiments and the well sizes for the crystals vary between 45  $\mu\text{m}$  and 60  $\mu\text{m}$ . An improved version of this chip design with well sizes ranging from 30  $\mu\text{m}$  to 100  $\mu\text{m}$  has been successfully used for data collection from Myoglobin crystals at the XPP instrument at LCLS [142]. The crystal sizes used for these experiments matched the well size.

A more compact silicon chip with a size of  $4.5 \times 2.5 \text{ mm}^2$  for microcrystals with dimensions of a few micrometers was developed and first employed for synchrotron experiments at cryogenic temperatures [140]. The design was later successfully used for SFX data collection at both cryogenic and at room temperature, again at the XPP instrument of LCLS [145]. Using this chip design in combination with a specially designed goniometer, called Roadrunner I, hit rates of up to 90% at a sample scan rate of 120 Hz were achieved. This approach allowed collecting complete data sets from CPV18 and BEV2 crystals in less than 10 min each, without post-refinement, similar to the time required for liquid-jet-based SFX under smooth running conditions.

### 5.8.2 *Sample Loading*

Sample loading should be easy and sample efficient, which means all sample material loaded onto the solid supports should be accessible to the X-rays and wasting material during loading should be avoided. Different approaches have been developed for loading samples onto fixed targets. Generally microcrystals of biological macromolecules have to be kept in a humid environment in order to prevent them from drying and thereby losing their diffraction properties. So the samples are ideally handled as suspensions using micropipettes. Depending on the chip size, typical amounts for loading samples on the chip are in the range of a few microliters.

In case of non-structured fixed target sample holders such as silicon nitride membranes, a small volume of the sample suspension is typically pipetted on the sample holder and then evenly distributed using a soft tool (e.g., a nylon loop) in order to avoid destroying the membrane [136, 137]. Structured sample holders aim to harvest the sample at predefined positions. One approach to achieve this is the use of a combination of hydrophobic and hydrophilic surface coatings [138] or the use of beads with a specific surface composition, which attract the crystals out of the suspension [141].

In another approach, the fixed target sample support is equipped with pores, which extend through the entire support. In this case, the sample solution is applied from one side, for example, by using a micropipette. By attaching a piece of filter paper from the other side, the solution is flowing through the pores and all particles larger than the pore diameter are retained and organize themselves according to the pore pattern as shown in Fig. 5.31 [140, 145]. Instead of wicking, it is also possible to achieve a liquid-flow through the pores by applying suction [140, 142].

A different approach has been recently reported by Opara et al. [146], where they have crystallized their samples directly on silicon nitride membranes that were sealed afterwards for the diffraction experiments. This approach has the advantage that it avoids the sample-loading step. This is especially useful in case of very sensitive crystals or large crystals, which are difficult to handle in a suspension due to sedimentation.

### 5.8.3 Preventing Samples from Drying Out

A major challenge for fixed target experiments with biological samples, in particular if they are to be carried out in vacuum, is preventing the samples from dehydration, which typically causes them to lose their diffraction properties. In general, three approaches can be followed to maintain the hydration of the samples for the diffraction experiment: (1) flash cooling to cryogenic temperatures, (2) keeping the micro-crystals in a sealed enclosure, or (3) providing a local humid environment for the samples.

The cryogenic approach is most commonly performed in conventional X-ray crystallography at synchrotron sources. Here the water contained in the protein crystals is vitrified in a solid state and thereby protects the crystals from drying out. So-called cryo-crystallography has the further advantage that radiation damage effects are reduced by more than two orders of magnitude at cryogenic temperatures compared to room temperature [147, 148]. Fixed target protein crystallography experiments at cryogenic temperatures have been carried out at LCLS and SACLA [139, 145, 149]. An advantage of fixed target SFX at cryogenic temperatures is that radiation damage effects to crystals in neighboring compartments, which are often pre-exposed by the tails of the X-ray beam, are reduced and higher sample densities with spacing down 10  $\mu\text{m}$  between two samples can be realized. For fixed target experiments at room temperature, a spacing of at least 20  $\mu\text{m}$  is required [145]. A certain risk of fixed target experiments at cryogenic temperatures is unwanted ice formation on the sample, as the resulting very strong Bragg reflection from the ice crystals can damage the detector.

In contrast to cryogenic temperatures, performing SFX experiments at room temperature allows studying protein dynamics and enzyme reactions [84, 85, 150]. For room temperature experiments it is required to permanently keep the crystals at a specific, well-defined humidity. The most common approach is to keep a small volume of the mother liquor close to the crystals and to seal the fixed target sample support from both sides with a material that is relatively transparent for X-rays

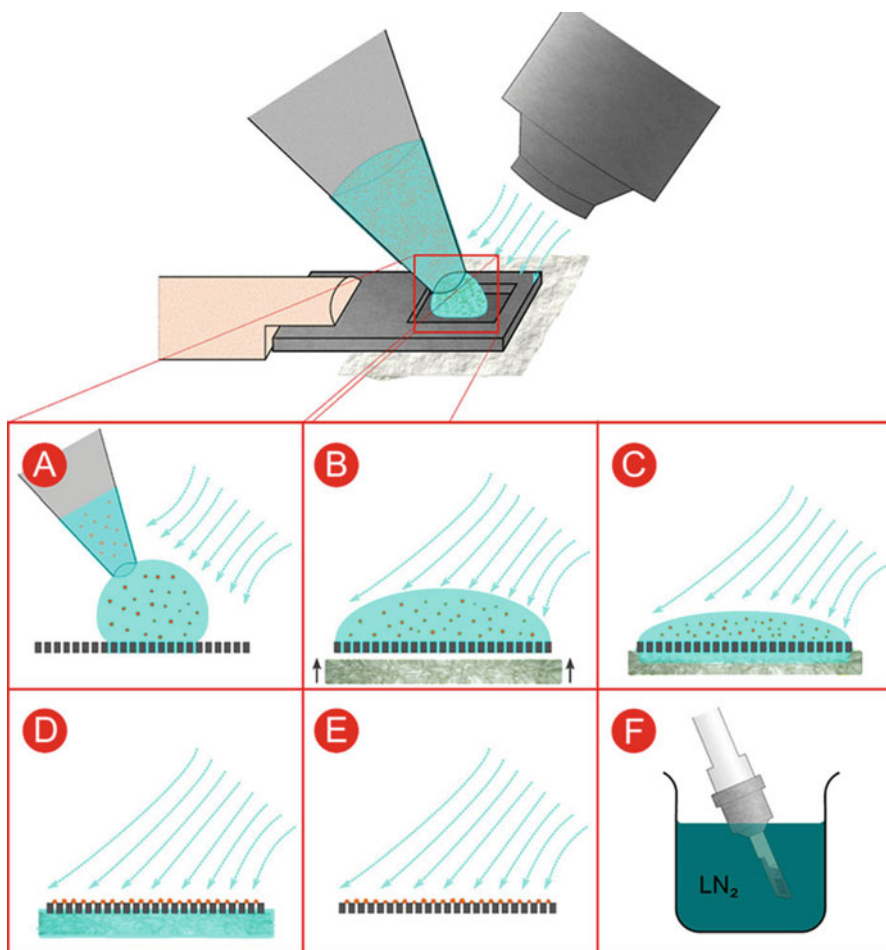


**Fig. 5.31** Loading of microcrystals on a fixed target equipped with micro-pores for holding the crystals: **(a)** A few microliters of the microcrystal suspension are pipetted onto the chip while kept in a stream of humidified air. **(b–d)** Mother liquor is soaked-off through the micro-pores by wicking with a filter paper from the lower side and inducing a liquid flow through the pores. **(e)** The microcrystals are retained by the pores and arrange themselves in a periodic fashion for effective scanning with the X-ray beam. **(f)** The chips can be plunged into liquid nitrogen in case of cryogenic data collection. Reproduced with permissions from Roedig et al. [140]

such as Silicon nitride [136, 137, 151] or Kapton or Mylar foil [141, 142] or a combination of both [138]. Graphene has been proposed as an ideal sealing material as it is extremely thin and has a very low cross section for X-rays. Due to its high fragility its application as a sealing material is challenging. Freestanding graphene can cover only very small areas of typically a few micrometers and additional sealing with Mylar foil was required in a recent application [152].

By performing the fixed target measurements in an atmosphere of controlled humidity, it is possible to avoid any sealing material. This approach has been developed for conventional synchrotron crystallography at room temperature [153, 154] and recently adapted to fixed target crystallography experiments at synchrotrons and X-ray FELs [145, 155]. Biological samples typically require relative humidity (r.h.) levels above 80%, depending on solvent content and chemical composition, and most of them require r.h. close to 100%. Avoiding any sealing of fixed target sample holders has advantages for time-resolved experiments since the samples are more or less freely accessible on the support, which will facilitate soaking or mixing experiments. Unwanted scattering and reflections by pump laser light by the sealing material are also prevented using this approach.

### 5.8.4 *Scattering Background*

For all measurements and in particular for weakly scattering samples such as very small crystals of large unit cell systems or even aperiodic objects such as individual virus particles, it is essential to keep the background scattering levels as low as possible. This is best achieved by avoiding any non-sample material to interact with the X-ray beam. In contrast to other sample delivery methods, fixed target experiments are often accompanied by significantly higher background scattering levels caused by the substrate and sealing material of the targets compared to other methods such as liquid jets. In order to minimize scattering from the sample holder, the sample holder should ideally consist of very thin membranes, such as silicon and silicon nitride that can be manufactured with thicknesses of a few tens of nanometers [136] or even better graphene mono-layers [152], which can be of sub-nanometer thicknesses. The use of a single crystalline and ideally defect free membrane material such as silicon is advantageous, since elastic scattering is limited to Bragg reflections, which occur only for specific orientations of the support material [140]. A certain limitation of this approach arises from risk of unwanted strong Bragg reflections of the support material, which can potentially damage the detector. In all cases, the thickness of the membranes should be kept thin in order to minimize inelastic scattering and X-ray fluorescence. Low-Z materials are generally preferable due to their weaker interaction with X-rays. For diffraction studies of larger objects such as microcrystals, the interaction of the support material with the X-rays can be further minimized by using a perforated supported material. Here the samples are located in micro-pores and the X-rays ideally only interact with the sample, which is larger than the pore diameter [140, 142, 145].

Further background scattering arises from interaction of the X-rays with air or gas. One approach is performing the fixed targets experiments in vacuum, which generally avoids air scattering. As a drawback this approach requires more sealing effort due to the pressure difference between the sample and the vacuum environment [136]. In addition, in-vacuum experiments provide limited access to the samples, for example, for performing time-resolved experiments. In another recent

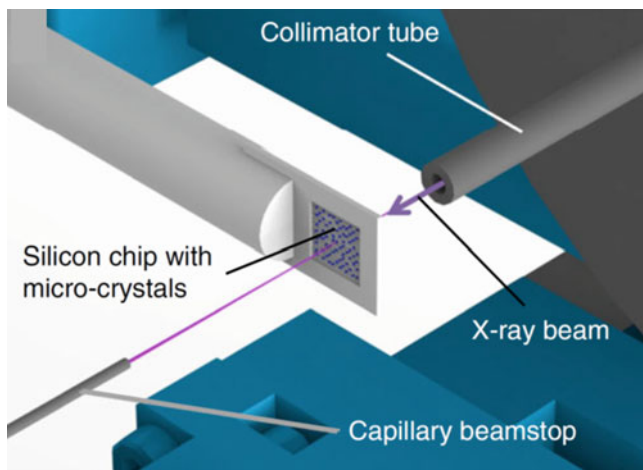


**Fig. 5.32** A CAD model of the X-ray interaction region of a Roadrunner geometry. A collimator tube upstream of the sample chip is large enough to let the X-rays pass through unobstructed. Its material and thickness are such to absorb any X-rays scattered from the air or upstream equipment. The X-rays then pass through the sample and chip and produce the desired diffraction signal; however, the spent beam which did not interact with the sample continues to interact with air downstream, thus requiring a capillary beamstop to terminate the beam. Modified with permissions from Meents et al. [156]

approach it has been possible to reduce air scattering by more than a factor of one hundred compared to conventional X-ray crystallography experiments by replacing air with by helium gas (which provides a factor of  $\sim 25$  lower cross section for X-rays) and by enclosing the direct beam shortly before and after the sample in capillary shields [156]. These upstream and downstream scatter guards, when placed close to the interaction region, can significantly reduce errant background scatter and improve the signal to noise, Fig. 5.32 shows more detail.

### 5.8.5 Scanning Approaches

For scanning of the fixed targets through the X-ray beam, either 2D or 3D scanning devices based on stepper motor translation stages [136], piezo-driven motor driven translation stages [142, 145, 157], or goniometers offering an additional rotational degree of freedom have been employed so far [139, 145].

Most of the fixed target SFX experiments have been performed in step-scanning mode. Here the sample frame is accelerated, moving to the next position, decelerated, and then stopped at the predefined position where it is then exposed to the X-ray pulse [136–139, 157]. The maximum sample exchange rate using this approach is typically limited to a few Hz. Recently, step scanning fixed target

experiments at a synchrotron were performed [158]. Faster scanning of fixed targets with sample exchange rates of the LCLS repetition rate of 120 Hz is achievable [145]. Instead of accelerating, moving, and decelerating the chip, a so-called fly-scan, where the fixed target is scanned at constant speed through the X-ray beam is applied. By inducing additional phase control to this scanning approach it was possible to expose the fixed target at the predefined samples positions. Using this approach, hit rates of up to 90% were achieved.

A certain complication in collecting complete datasets in fixed target experiments arises from preferred orientation of some crystal types on their supports. This is in particular severe for plate- and needle-shaped crystals mounted on flat membranes. The preferred orientation gives a range of reciprocal space that is not sampled for a fixed mounting angle. One approach to mitigate this problem is to use micro-structured sample holders which provide different well shapes in order to harvest the crystals in different orientations [140, 142]. Another approach is rotating the sample holder with respect to the incoming beam so that the crystals are exposed in different directions [139, 145].

### ***5.8.6 Time-Resolved Experiments***

So far only very few time-resolved experiments have been published using fixed target sample delivery methods [114], as this is accompanied with several challenges: for example, for pump probe experiments using laser excitation, the pre-exposure of crystals in the neighboring compartments with laser light. For other time-resolved experiments, such reaction initialization by micro-diffusion, sealing of the chips for example with Mylar foil to prevent the crystals from drying out, represents a major limitation, as the samples are not directly accessible, for example by spraying a substrate or ligand solution on the fixed target. For such experiments an approach with non-sealed chips kept in a humid atmosphere offers much more flexibility, as the samples are directly accessible to all different kind of spraying or microinjection approaches. Avoiding sealing of the chips has also advantages for laser excitation as the pump light has not to pass through any sealing material which in many cases results in scattering or even absorption of the light. In comparison to sample delivery with jets, where the surrounding liquid stream often acts as a lens for the laser light and thereby to undefined illumination conditions, fixed target pump probe experiments—at least in principle—should allow for a well-defined a reproducible illumination scheme.

### ***5.8.7 Summary***

Fixed target approaches for SFX offer an alternative means of delivering sample to fixed target experiments allow high hit rates of up to 90% at X-ray FEL's with

data collection time of less than 10 min and require only very small amounts of sample, which can be as little as 4  $\mu\text{g}$  for a complete SFX structure determination. The complicated machinery can be an obstacle to new users, but once standard in a facility's deployment, the barrier to entry for the crystallographer can be low. Custom chip substrates can be expensive for multiple datasets, but costs may diminish over time. Loading the sample onto the chip substrate can also require skill and practice and can vary from sample to sample. The high machine precision makes rapid scanning fixed target techniques an ideal candidate for high precision optical pump-probe experiments, where variations in flows can diminish high timing precision.

## 5.9 Outlook

The sample delivery methods presented in this chapter are plentiful and constantly evolving. The evolution of sample delivery methods continues to progress as SFX is attempted with new protein crystal systems, which introduce new complications. The serial crystallography sample delivery journey started from largely inefficient methods like aerosol lens stacks, Rayleigh jets and crude fixed target systems. Over the years, gas-focused approaches allowed the generation of smaller jets and increased the sample delivery efficiency with the GDVN, yet the sample consumption remained too high for certain systems. The electrokinetics of electro-spraying were leveraged to create a lower flow rate MESH and modified coMESH injection method. Concurrently, higher viscosity media were explored with reduced sample consumption; the improvement in detector technology and shorter X-ray FEL wavelengths allowed experiments to be performed at ambient conditions. The LCP injector and similar high viscosity extrusion devices have aided in the fight to reduce sample consumption while maintaining compatibility with the persnickety crystallization conditions. The DFFN improved the parameter space available to the GDVN and further improved the stability for troubling systems. Droplet injection systems at SACLA have been developed that match the droplet generation rate to the FEL repetition rate. Fixed targets have had a resurgence in an effort to get higher hit rates and reduced sample consumption, thus maximizing the sample delivery efficiency.

SFX experiments have matured to the point where sufficient preparation can lead to minimal surprises during an experiment and guarantee as successful an experiment as the crystal diffraction permits. Sample sedimentation continues to be an issue that can lead to clogging and diminished data collection. As 3D printing techniques improve, the reproducibility of complex injection nozzles, like the DFFN, GDVN, and mixing variants, are substantially improved, leading to better performance from nozzle to nozzle.

New techniques are being developed to help improve injection and sample preparation. Microfluidic chips [93] are being developed as injection and mixing nozzles and dielectrophoresis can be used to sort crystals based upon size [159].

As these injection methods have been developed for X-ray FELs, goniometer and fixed-target approaches from synchrotrons have been crossed between both former and current generation sources. Serial diffraction techniques have moved to synchrotrons and have proved successful in many instances, using lower flow rate HVE and MESH methods or scanned fixed target holders (Roadrunner), since millisecond exposure times are needed to obtain sufficient scattering signal from the available flux. Nanometer liquid sheets have also been developed for soft X-ray studies and may find a use in serial crystallography [160]. High speed injectors are currently being studied to maximize the efficiency of delivery at higher repetition rate sources [161].

The ability to obtain femtosecond snapshots from protein crystals will eventually lead to the realization of a longtime goal in structural biology and chemistry: to view structural intermediates. The next few years will see an increase in time-resolved studies beyond optical pump–probe. These mixing experiments will require further understanding of the underlying fluid mechanics and will likely be a significant cornerstone of a future text on sample delivery techniques of SFX.

## References

1. Chapman, H. N., Barty, A., Bogan, M. J., Boutet, S., Frank, M., Hau-Riege, S. P., et al. (2006). Femtosecond diffractive imaging with a soft-X-ray free-electron laser. *Nature Physics*, 2(12), 839–843. <https://doi.org/10.1038/nphys461>.
2. Stan, C. A., Milathianaki, D., Laksmono, H., Sierra, R. G., McQueen, T. A., Messerschmidt, M., et al. (2016). Liquid explosions induced by X-ray laser pulses. *Nature Physics*, 12, 966. <https://doi.org/10.1038/nphys3779>.
3. Chapman, H. N., Fromme, P., Barty, A., White, T. A., Kirian, R. A., Aquila, A., et al. (2011). Femtosecond X-ray protein nanocrystallography. *Nature*, 470(7332), 73–77. <https://doi.org/10.1038/nature09750>.
4. Seibert, M. M., Ekeberg, T., Maia, F. R. N. C., Svenda, M., Andreasson, J., Jönsson, O., et al. (2011). Single mimivirus particles intercepted and imaged with an X-ray laser. *Nature*, 470(7332), 78–81. <https://doi.org/10.1038/nature09748>.
5. Bogan, M. J., Benner, W. H., Boutet, S., Rohner, U., Frank, M., Barty, A., et al. (2008). Single particle X-ray diffractive imaging. *Nano Letters*, 8(1), 310–316. <https://doi.org/10.1021/nl072728k>.
6. Awel, S., Kirian, R. A., Wiedorn, M. O., Beyerlein, K. R., Roth, N., Horke, D. A., et al. (2018). Femtosecond X-ray diffraction from an aerosolized beam of protein nanocrystals. *Journal of Applied Crystallography*, 51(1), 133–139. <https://doi.org/10.1107/S1600576717018131>.
7. Hantke, M. F., Hasse, D., Maia, F. R. N. C., Ekeberg, T., John, K., Svenda, M., et al. (2014). High-throughput imaging of heterogeneous cell organelles with an X-ray laser. *Nature Photonics*, 8(12), 943–949. <https://doi.org/10.1038/nphoton.2014.270>.
8. Munke, A., Andreasson, J., Aquila, A., Awel, S., Ayyer, K., Barty, A., et al. (2016). Coherent diffraction of single Rice Dwarf virus particles using hard X-rays at the Linac Coherent Light Source. *Scientific Data*, 3, 160064. <https://doi.org/10.1038/sdata.2016.64>.
9. Rayleigh, L. (1878). On the instability of jets. *Proceedings of the London Mathematical Society*, 1(1), 4 Retrieved from <http://plms.oxfordjournals.org/content/s1-10/1/4.full.pdf>.
10. Rayleigh, L. (1892). XVI. On the instability of a cylinder of viscous liquid under capillary force. *The London, Edinburgh, and Dublin Philosophical Magazine and Journal of Science*, 34(207), 145–154. <https://doi.org/10.1080/14786449208620301>.

11. Faubel, M., Schlemmer, S., & Toennies, J. (1988). A molecular beam study of the evaporation of water from a liquid jet. *Zeitschrift fur Physik D: Atoms, Molecules and Clusters*, 10(2), 269–277 Retrieved from <http://www.springerlink.com/index/X6GXW8Q11QV3R085.pdf>.
12. Weierstall, U., Doak, R., Spence, J. C. H., Starodub, D., Shapiro, D., Kennedy, P., et al. (2008). Droplet streams for serial crystallography of proteins. *Experiments in Fluids*, 44(5), 675–689 Retrieved from <http://www.springerlink.com/index/Q7N2L3278806078U.pdf>.
13. DePonte, D. P., Weierstall, U., Schmidt, K., Warner, J., Starodub, D., Spence, J. C. H., et al. (2008). Gas dynamic virtual nozzle for generation of microscopic droplet streams. *Journal of Physics D: Applied Physics*, 41(19), 195505. <https://doi.org/10.1088/0022-3727/41/19/195505>.
14. White, F., & Corfield, I. (2005). *Viscous fluid flow* (3rd ed.). New York: McGraw-Hill.
15. Eggers, J., & Villermaux, E. (2008). Physics of liquid jets. *Reports on Progress in Physics*, 71(1), 1–79. <https://doi.org/10.1088/0034-4885/71/3/036601>.
16. Gonzalez-Tello, P., Camacho, F., & Blazquez, G. (1994). Density and viscosity of concentrated aqueous solutions of polyethylene glycol. *Journal of Chemical & Engineering Data*, 39(3), 611–614. <https://doi.org/10.1021/je00015a050>.
17. Lee, R. J., & Teja, A. S. (1990). Viscosities of poly(ethylene glycols). *Journal of Chemical & Engineering Data*, 35(4), 385–387. <https://doi.org/10.1021/je00062a003>.
18. Einstein, A. (1905). On the motion of small particles suspended in a stationary liquid, as required by the molecular kinetic theory of heat. *Annalen der Physik*, 322, 549–560. <https://doi.org/10.1002/andp.19053220806>.
19. Probst, R. F. (1994). *Physicochemical hydrodynamics*. New York: Wiley. <https://doi.org/10.1002/0471725137>.
20. Lomb, L., Steinbrener, J., Bari, S., Beisel, D., Berndt, D., Kieser, C., et al. (2012). An anti-settling sample delivery instrument for serial femtosecond crystallography. *Journal of Applied Crystallography*, 45(4), 1–5. <https://doi.org/10.1107/S0021889812024557>.
21. Sierra, R. G., Gati, C., Laksmono, H., Dao, E. H., Gul, S., Fuller, F., et al. (2015). Concentric-flow electrokinetic injector enables serial crystallography of ribosome and photosystem II. *Nature Methods*, 13(1), 59–62. <https://doi.org/10.1038/nmeth.3667>.
22. Johansson, L. C., Arnlund, D., White, T. A., Katona, G., Deponte, D. P., Weierstall, U., et al. (2012). Lipidic phase membrane protein serial femtosecond crystallography. *Nature Methods*, 9(3), 263–265. <https://doi.org/10.1038/nmeth.1867>.
23. Oberthuer, D., Knořka, J., Wiedorn, M. O., Beyerlein, K. R., Bushnell, D. A., Kovaleva, E. G., et al. (2017). Double-flow focused liquid injector for efficient serial femtosecond crystallography. *Scientific Reports*, 7, 44628. <https://doi.org/10.1038/srep44628>.
24. Taylor, G. (1953). Dispersion of soluble matter in solvent flowing slowly through a tube. *Proceedings of the Royal Society of London A: Mathematical, Physical and Engineering Sciences*, 219(1137), 186–203. <https://doi.org/10.1098/rspa.1953.0139>.
25. Taneda, S. (1979). Visualization of separating Stokes flows. *Journal of the Physical Society of Japan*, 46(6), 1935–1942. <https://doi.org/10.1143/JPSJ.46.1935>.
26. Purcell, E. (1976). Life at low Reynolds number. *AIP Conference Proceedings*, 45, 3–11.
27. Rayleigh, L. (1879). On the capillary phenomena of jets. *Proceedings of the Royal Society of London*, 29, 71–97.
28. Frohn, A., & Roth, N. (2000). *Dynamics of droplets*. Berlin, Germany: Springer Science & Business Media.
29. Gañán-Calvo, A. M. (1998). Generation of steady liquid microthreads and micron-sized monodisperse sprays in gas streams. *Physical Review Letters*, 80(2), 285.
30. Lomb, L., Steinbrener, J., Bari, S., Beisel, D., Berndt, D., Kieser, C., et al. (2012). An anti-settling sample delivery instrument for serial femtosecond crystallography. *Journal of Applied Crystallography*, 45(4), 674–678.
31. Weierstall, U., Spence, J. C. H., & Doak, R. B. (2012). Injector for scattering measurements on fully solvated biospecies. *The Review of Scientific Instruments*, 83(3), 035108.

32. Nelson, G., Kirian, R. A., Weierstall, U., Zatsepin, N. A., Faragó, T., Baumbach, T., et al. (2016). Three-dimensional-printed gas dynamic virtual nozzles for x-ray laser sample delivery. *Optics Express*, 24(11), 11515–11530.
33. Wang, D., Weierstall, U., Pollack, L., & Spence, J. (2014). Double-focusing mixing jet for XFEL study of chemical kinetics. *Journal of Synchrotron Radiation*, 21(6), 1364–1366.
34. Weierstall, U., Doak, R. B., & Spence, J. C. H. (2011). A pump-probe XFEL particle injector for hydrated samples. arXiv preprint arXiv:1105.2104.
35. Daurer, B. J., Okamoto, K., Bielecki, J., Maia, F. R. N. C., Muhlig, K., Seibert, M. M., et al. (2017). Experimental strategies for imaging bioparticles with femtosecond hard X-ray pulses. *IUCrJ*, 4(3), 251–262. <https://doi.org/10.1107/S2052252517003591>.
36. Perry, S. L., Guha, S., Pawate, A. S., Bhaskarla, A., Agarwal, V., Nair, S. K., et al. (2013). A microfluidic approach for protein structure determination at room temperature via on-chip anomalous diffraction. *Lab on a Chip*, 13(16), 3183–3187.
37. Zhu, L., Weierstall, U., Cherezov, V., & Liu, W. (2016). Serial femtosecond crystallography of membrane proteins. In I. Moraes (Ed.), *The next generation in membrane protein structure determination* (pp. 151–160). Cham, Switzerland: Springer.
38. Martin-Garcia, J. M., Conrad, C. E., Nelson, G., Stander, N., Zatsepin, N. A., Zook, J., et al. (2017). Serial millisecond crystallography of membrane and soluble protein microcrystals using synchrotron radiation. *IUCrJ*, 4, 439–454. <https://doi.org/10.1107/S205225251700570X>.
39. Tono, K., Nango, E., Sugahara, M., Song, C., Park, J., Tanaka, T., et al. (2015). Diverse application platform for hard X-ray diffraction in SACLA (DAPHNIS): Application to serial protein crystallography using an X-ray free-electron laser. *Journal of Synchrotron Radiation*, 22, 532–537. <https://doi.org/10.1107/S1600577515004464>.
40. Sugahara, M., Mizohata, E., Nango, E., Suzuki, M., Tanaka, T., Masuda, T., et al. (2015). Grease matrix as a versatile carrier of proteins for serial crystallography. *Nature Methods*, 12(1), 61–63.
41. Botha, S., Nass, K., Barends, T. R. M., Kabsch, W., Latz, B., Dworkowski, F., et al. (2015). Room-temperature serial crystallography at synchrotron X-ray sources using slowly flowing free-standing high-viscosity microstreams. *Acta Crystallographica. Section D, Biological Crystallography*, 71(2), 387.
42. Conrad, C. E., Basu, S., James, D., Wang, D., Schaffer, A., Roy-Chowdhury, S., et al. (2015). A novel inert crystal delivery medium for serial femtosecond crystallography. *IUCrJ*, 2(4), 421–430.
43. Sugahara, M., Song, C., Suzuki, M., Masuda, T., Inoue, S., Nakane, T., et al. (2016). Oil-free hyaluronic acid matrix for serial femtosecond crystallography. *Scientific Reports*, 6, 1–6.
44. Kovacsova, G., Grunbein, M. L., Kloos, M., Barends, T. R. M., Schlesinger, R., Heberle, J., et al. (2017). Viscous hydrophilic injection matrices for serial crystallography. *IUCrJ*, 4, 400–410. <https://doi.org/10.1107/S2052252517005140>.
45. Weierstall, U., James, D., Wang, C., White, T. A., Wang, D., Liu, W., et al. (2014). Lipidic cubic phase injector facilitates membrane protein serial femtosecond crystallography. *Nature Communications*, 5, 3309.
46. Zhang, H., Unal, H., Gati, C., Han, G. W., Liu, W., Zatsepin, N. A., et al. (2015). Structure of the angiotensin receptor revealed by serial femtosecond crystallography. *Cell*, 161(4), 833–844.
47. Fenalti, G., Zatsepin, N. A., Betti, C., Giguere, P., Han, G. W., Ishchenko, A., et al. (2015). Structural basis for bifunctional peptide recognition at human delta-opioid receptor. *Nature Structural & Molecular Biology*, 22(3), 265–268.
48. Kang, Y., Zhou, X. E., Gao, X., He, Y., Liu, W., Ishchenko, A., et al. (2015). Crystal structure of rhodopsin bound to arrestin by femtosecond X-ray laser. *Nature*, 523(7562), 561–567.
49. Nogly, P., Panneels, V., Nelson, G., Gati, C., Kimura, T., Milne, C., et al. (2016). Lipidic cubic phase injector is a viable crystal delivery system for time-resolved serial crystallography. *Nature Communications*, 7, 1–9.

50. Batyuk, A., Galli, L., Ishchenko, A., Han, G. W., Gati, C., Popov, P. A., et al. (2016). Native phasing of x-ray free-electron laser data for a G protein-coupled receptor. *Science Advances*, 2(9), e1600292.
51. Fromme, R., Ishchenko, A., Metz, M., Chowdhury, S. R., Basu, S., Boutet, S., et al. (2015). Serial femtosecond crystallography of soluble proteins in lipidic cubic phase. *IUCrJ*, 2(5), 545–551.
52. James, D., Wang, D., White, T. A., Zatsepin, N., Nelson, G., Liu, H., et al. (2015). Lipidic cubic phase serial millisecond crystallography using synchrotron radiation. *IUCrJ*, 2(2), 168–176.
53. Sierra, R. G., Laksmono, H., Kern, J., Tran, R., Hattne, J., Alonso-Mori, R., et al. (2012). Nanoflow electrospinning serial femtosecond crystallography. *Acta Crystallographica. Section D, Biological Crystallography*, 68(11), 1584–1587. <https://doi.org/10.1107/S0907444912038152>.
54. Hattne, J., Echols, N., Tran, R., Kern, J., Gildea, R. J., Brewster, A. S., et al. (2014). Accurate macromolecular structures using minimal measurements from X-ray free-electron lasers. *Nature Methods*, 11(5), 545–548. <https://doi.org/10.1038/nmeth.2887>.
55. Kern, J., Alonso-Mori, R., Hellmich, J., Tran, R., Hattne, J., Laksmono, H., et al. (2012). Room temperature femtosecond X-ray diffraction of photosystem II microcrystals. *Proceedings of the National Academy of Sciences of the United States of America*, 109(25), 9721–9726. <https://doi.org/10.1073/pnas.1204598109>.
56. Kern, J., Tran, R., Alonso-Mori, R., Koroidov, S., Echols, N., Hattne, J., et al. (2014). Taking snapshots of photosynthetic water oxidation using femtosecond X-ray diffraction and spectroscopy. *Nature Communications*, 5, 4371. <https://doi.org/10.1038/ncomms5371>.
57. Young, I. D., Ibrahim, M., Chatterjee, R., Gul, S., Fuller, F. D., Koroidov, S., et al. (2016). Structure of photosystem II and substrate binding at room temperature. *Nature*, 540(7633), 453–457. <https://doi.org/10.1038/nature20161>.
58. Alonso-Mori, R., Kern, J., Gildea, R. J., Sokaras, D., Weng, T.-C., Lassalle-Kaiser, B., et al. (2012). Energy-dispersive X-ray emission spectroscopy using an X-ray free-electron laser in a shot-by-shot mode. *Proceedings of the National Academy of Sciences of the United States of America*, 109(47), 19103. <https://doi.org/10.1073/pnas.1211384109>.
59. Kern, J., Alonso-Mori, R., Tran, R., Hattne, J., Gildea, R. J., Echols, N., et al. (2013). Simultaneous femtosecond X-ray spectroscopy and diffraction of photosystem II at room temperature. *Science*, 340(6131), 491–495. <https://doi.org/10.1126/science.1234273>.
60. Kroll, T., Kern, J., Kubin, M., Ratner, D., Gul, S., Fuller, F. D., et al. (2016). X-ray absorption spectroscopy using a self-seeded soft X-ray free-electron laser. *Optics Express*, 24(20), 22469. <https://doi.org/10.1364/OE.24.022469>.
61. Kubin, M., Kern, J., Gul, S., Kroll, T., Chatterjee, R., Löchel, H., et al. (2017). Soft x-ray absorption spectroscopy of metalloproteins and high-valent metal-complexes at room temperature using free-electron lasers. *Structural Dynamics*, 4(5), 054307. <https://doi.org/10.1063/1.4986627>.
62. Mitzner, R., Rehanek, J., Kern, J., Gul, S., Hattne, J., Taguchi, T., et al. (2013). L-edge X-ray absorption spectroscopy of dilute systems relevant to metalloproteins using an X-ray free-electron laser. *Journal of Physical Chemistry Letters*, 4, 3641–3647. <https://doi.org/10.1021/jz401837f>.
63. Colletier, J.-P., Sawaya, M. R., Gingery, M., Rodriguez, J. A., Cascio, D., Brewster, A. S., et al. (2016). De novo phasing with X-ray laser reveals mosquito larvicide BinAB structure. *Nature*, 539(7627), 43–47. <https://doi.org/10.1038/nature19825>.
64. Fernández de la Mora, J. (2007). The fluid dynamics of Taylor cones. *Annual Review of Fluid Mechanics*, 39(1), 217–243. <https://doi.org/10.1146/annurev.fluid.39.050905.110159>.
65. Gañán-Calvo, A. M., & Barrero, A. (1999). A novel pneumatic technique to generate steady capillary microjets. *Journal of Aerosol Science*, 30(1), 117–125. [https://doi.org/10.1016/S0021-8502\(98\)00029-9](https://doi.org/10.1016/S0021-8502(98)00029-9).
66. Aquila, A., Hunter, M. S., Doak, R. B., Kirian, R. A., Fromme, P., White, T. A., et al. (2012). Time-resolved protein nanocrystallography using an X-ray free-electron laser. *Optics Express*, 20(3), 2706–2716 Retrieved from <http://www.opticsinfobase.org/abstract.cfm?URI=oe-20-3-2706>.

67. Barty, A., Caleman, C., Aquila, A., Timneanu, N., Lomb, L., White, T. A., et al. (2012). Self-terminating diffraction gates femtosecond X-ray nanocrystallography measurements. *Nature Photonics*, 6(1), 35–40. <https://doi.org/10.1038/nphoton.2011.297>.
68. Boutet, S., Lomb, L., Williams, G. J., Barends, T. R. M., Aquila, A., Doak, R. B., et al. (2012). High-resolution protein structure determination by serial femtosecond crystallography. *Science*, 337(6092), 362–364. <https://doi.org/10.1126/science.1217737>.
69. Koopmann, R., Cupelli, K., Redecke, L., Nass, K., DePonte, D. P., White, T. A., et al. (2012). In vivo protein crystallization opens new routes in structural biology. *Nature Methods*, 9(3), 259–262. <https://doi.org/10.1038/nmeth.1859>.
70. Lomb, L., Barends, T. R. M., Kassemeyer, S., Aquila, A., Epp, S., Erk, B., et al. (2011). Radiation damage in protein serial femtosecond crystallography using an x-ray free-electron laser. *Physical Review B*, 84(21), 1–6. <https://doi.org/10.1103/PhysRevB.84.214111>.
71. Garman, E. (1999). Cool data: Quantity AND quality. *Acta Crystallographica, Section D: Biological Crystallography*, 55(10), 1641–1653. <https://doi.org/10.1107/S0907444999008653>.
72. Garman, E. F., & Owen, R. L. (2006). Cryocooling and radiation damage in macromolecular crystallography. *Acta Crystallographica, Section D: Biological Crystallography*, 62(1), 32–47. <https://doi.org/10.1107/S0907444905034207>.
73. Ibrahim, M., Chatterjee, R., Hellmich, J., Tran, R., Bommer, M., Yachandra, V. K., et al. (2015). Improvements in serial femtosecond crystallography of photosystem II by optimizing crystal uniformity using microseeding procedures. *Structural Dynamics*, 2(4), 041705. <https://doi.org/10.1063/1.4919741>.
74. Gañán-Calvo, A. M., & Montanero, J. (2009). Revision of capillary cone-jet physics: Electrospray and flow focusing. *Physical Review E*, 79(6), 1–18. <https://doi.org/10.1103/PhysRevE.79.066305>.
75. Liang, M., Williams, G. J., Messerschmidt, M., Seibert, M. M., Montanez, P. A., Hayes, M., et al. (2015). The coherent X-ray imaging instrument at the Linac Coherent Light Source. *Journal of Synchrotron Radiation*, 22(3), 514–519. <https://doi.org/10.1107/S160057751500449X>.
76. Schlichting, I. (2015). Serial femtosecond crystallography: The first five years. *IUCrJ*, 2, 246.
77. Redecke, L., Nass, K., DePonte, D. P., White, T. A., Rehders, D., Barty, A., et al. (2013). Natively inhibited Trypanosoma brucei cathepsin B structure determined by using an X-ray laser. *Science*, 339, 227–230.
78. Emma, P., Akre, R., Arthur, J., Bionta, R., Bostedt, C., Bozek, J., et al. (2010). First lasing and operation of an ångström-wavelength free-electron laser. *Nature Photonics*, 4, 641–647.
79. Beyerlein, K. R., Adriano, L., Heymann, M., Kirian, R., Knoška, J., Wilde, F., et al. (2015). Ceramic micro-injection molded nozzles for serial femtosecond crystallography sample delivery. *The Review of Scientific Instruments*, 86, 125104.
80. Barends, T. R., Foucar, L., Ardevol, A., Nass, K., Aquila, A., Botha, S., et al. (2015). Direct observation of ultrafast collective motions in CO myoglobin upon ligand dissociation. *Science*, 350, 445–450.
81. Coquelle, N., Sliwa, M., Woodhouse, J., Schirò, G., Adam, V., Aquila, A., et al. (2018). Chromophore twisting in the excited state of a photoswitchable fluorescent protein captured by time-resolved serial femtosecond crystallography. *Nature Chemistry*, 10, 31–37.
82. Pande, K., Hutchison, C. D., Groenhof, G., Aquila, A., Robinson, J. S., Tenboer, J., et al. (2016). Femtosecond structural dynamics drives the trans/cis isomerization in photoactive yellow protein. *Science*, 352, 725–729.
83. Tenboer, J., Basu, S., Zatsepin, N., Pande, K., Milathianaki, D., Frank, M., et al. (2014). Time-resolved serial crystallography captures high-resolution intermediates of photoactive yellow protein. *Science*, 346, 1242–1246.
84. Kupitz, C., Olmos Jr., J. L., Holl, M., Tremblay, L., Pande, K., Pandey, S., et al. (2017). Structural enzymology using X-ray free electron lasers. *Structural Dynamics*, 4(4), 044003.
85. Stagno, J. R., Liu, Y., Bhandari, Y. R., Conrad, C. E., Panja, S., Swain, M., et al. (2017). Structures of riboswitch RNA reaction states by mix-and-inject XFEL serial crystallography. *Nature*, 541, 242–246.

86. Gañán-Calvo, A. M., González-Prieto, R., Riesco-Chueca, P., Herrada, M. A., & Flores-Mosquera, M. (2007). Focusing capillary jets close to the continuum limit. *Nature Physics*, *3*, 737–742.
87. Acero, A. J., Ferrera, C., Montanero, J. M., & Gañán-Calvo, A. M. (2012). Focusing liquid microjets with nozzles. *Journal of Micromechanics and Microengineering*, *22*, 065011.
88. Montanero, J. M., Rebollo-Munoz, N., Herrada, M. A., & Gañán-Calvo, A. M. (2011). Global stability of the focusing effect of fluid jet flows. *Physical Review. E, Statistical, Nonlinear, and Soft Matter Physics*, *83*, 036309.
89. Vega, E. J., Montanero, J. M., Herrada, M. A., & Gañán-Calvo, A. M. (2010). Global and local instability of flow focusing: The influence of the geometry. *Physics of Fluids*, *22*, 064105.
90. Schmidt, M. (2013). Mix and inject: Reaction initiation by diffusion for time-resolved macromolecular crystallography. *Advances in Condensed Matter Physics*, *2013*, 1–10.
91. Calvey, G. D., Katz, A. M., Schaffer, C. B., & Pollack, L. (2016). Mixing injector enables time-resolved crystallography with high hit rate at X-ray free electron lasers. *Structural Dynamics*, *3*, 054301.
92. Chavas, L. M., Gumprecht, L., & Chapman, H. N. (2015). Possibilities for serial femtosecond crystallography sample delivery at future light sources. *Structural Dynamics*, *2*, 041709.
93. Trebbin, M., Krüger, K., DePonte, D., Roth, S. V., Chapman, H. N., & Förster, S. (2014). Microfluidic liquid jet system with compatibility for atmospheric and high-vacuum conditions. *Lab on a Chip*, *14*, 1733–1745.
94. Au, A. K., Huynh, W., Horowitz, L. F., & Folch, A. (2016). 3D-printed microfluidics. *Angewandte Chemie (International Ed. in English)*, *55*, 3862–3881.
95. Moffat, K. (2014). Time-resolved crystallography and protein design: Signalling photoreceptors and optogenetics. *Philosophical Transactions of the Royal Society of London. Series B, Biological Sciences*, *369*, 20130568.
96. Neutze, R. (2014). Opportunities and challenges for time-resolved studies of protein structural dynamics at X-ray free-electron lasers. *Philosophical Transactions of the Royal Society of London. Series B, Biological Sciences*, *369*, 20130318.
97. Neutze, R., & Moffat, K. (2012). Time-resolved structural studies at synchrotrons and X-ray free electron lasers: Opportunities and challenges. *Current Opinion in Structural Biology*, *22*, 651–659.
98. Schlichting, I., & Goody, R. S. (1997). Triggering methods in crystallographic enzyme kinetics. *Methods in Enzymology*, *277*, 467–490.
99. Barends, T., White, T. A., Barty, A., Foucar, L., Messerschmidt, M., Alonso-Mori, R., et al. (2015). Effects of self-seeding and crystal post-selection on the quality of Monte Carlo-integrated SFX data. *Journal of Synchrotron Radiation*, *22*, 644.
100. Brennich, M. E., Nolting, J. F., Dammann, C., Nöding, B., Bauch, S., & Herrmann, H. (2011). Dynamics of intermediate filament assembly followed in micro-flow by small angle X-ray scattering. *Lab on a Chip*, *11*, 708–716.
101. Knight, J., Vishwanath, A., Brody, J., & Austin, R. (1998). Hydrodynamic focusing on a silicon chip: Mixing nanoliters in microseconds. *Physical Review Letters*, *80*, 3863–3866.
102. Park, H. Y., Qiu, X., Rhoades, E., Korlach, J., Kwok, L. W., & Zipfel, W. R. (2006). Achieving uniform mixing in a microfluidic device: Hydrodynamic focusing prior to mixing. *Analytical Chemistry*, *78*, 4465–4473.
103. Pollack, L., & Doniach, S. (2009). Time-resolved X-ray scattering and RNA folding. *Methods in Enzymology*, *469*, 253–268.
104. Pollack, L., Tate, M. W., Darnton, N. C., Knight, J. B., Gruner, S. M., Eaton, W. A., et al. (1999). Compactness of the denatured state of a fast-folding protein measured by submillisecond small-angle x-ray scattering. *Proceedings of the National Academy of Sciences*, *96*, 10115–10117.
105. Zahoor, R., Belšak, G., Bajt, S., Weckert, E., & Hajdu, J. (2018). Simulation of liquid microjet in free expanding high-speed co-flowing gas streams. *Microfluidics and Nanofluidics*, *22*, 87. <https://doi.org/10.1007/s10404-018-2110-0>.

106. Neutze, R., Wouts, R., van der Spoel, D., Weckert, E., & Hajdu, J. (2000). Potential for biomolecular imaging with femtosecond X-ray pulses. *Nature*, *406*, 752–757.
107. Fukuda, Y., Tse, K. M., Nakane, T., Nakatsu, T., Suzuki, M., Sugahara, M., et al. (2016). Redox-coupled proton transfer mechanism in nitrite reductase revealed by femtosecond crystallography. *Proceedings of the National Academy of Sciences of the United States of America*, *113*, 2928–2933.
108. Liu, W., Wacker, D., Gati, C., Han, G. W., James, D., Wang, D., et al. (2013). Serial femtosecond crystallography of G protein–coupled receptors. *Science*, *342*, 1521–1524.
109. Mafuné, F., Miyajima, K., Tono, K., Takeda, Y., Kohno, J. Y., Miyauchi, N., et al. (2016). Microcrystal delivery by pulsed liquid droplet for serial femtosecond crystallography. *Acta Crystallographica, Section D: Biological Crystallography*, *72*(Pt 4), 520–523.
110. Zhou, Q., Lai, Y., Bacaj, T., Zhao, M., Lyubimov, A. Y., Uevirojnangkoom, M., et al. (2015). Architecture of the synaptotagmin–SNARE machinery for neuronal exocytosis. *Nature*, *525*, 62–67.
111. Kupitz, C., Basu, S., Grotjohann, I., Fromme, R., Zatsepin, N. A., Rendek, K. N., et al. (2014). Serial time-resolved crystallography of photosystem II using a femtosecond X-ray laser. *Nature*, *513*, 261–265.
112. Nango, E., Royant, A., Kubo, M., Nakane, T., Wickstrand, C., Kimura, T., et al. (2016). A three dimensional movie of structural changes in bacteriorhodopsin. *Science*, *354*, 1552–1557.
113. Nogly, P., Panneels, V., Nelson, G., Gati, C., Kimura, T., Milne, C., et al. (2016). Lipidic cubic phase injector is a viable crystal delivery system for time-resolved serial crystallography. *Nature Communications*, *7*, 12314.
114. Suga, M., Akita, F., Sugahara, M., Kubo, M., Nakajima, Y., Nakane, T., et al. (2017). Light-induced structural changes and the site of O=O bond formation in PSII caught by XFEL. *Nature*, *543*, 131–135.
115. Sugahara, M., Song, C., Suzuki, M., Masuda, T., Inoue, S., Nakane, T., et al. (2016). Oil-free hyaluronic acid matrix for serial femtosecond crystallography. *Scientific Reports*, *6*, 24484.
116. Sugahara, M., Nakane, T., Masuda, T., Suzuki, M., Inoue, S., Song, C., et al. (2017). Hydroxyethyl cellulose matrix applied to serial crystallography. *Scientific Reports*, *7*, 703.
117. Hope, H. (1988). *Acta Crystallographica. Section B*, *44*, 22–26.
118. Nakane, T., Song, C., Suzuki, M., Nango, E., Kobayashi, J., Masuda, T., et al. (2015). Native sulfur/chlorine SAD phasing for serial femtosecond crystallography. *Acta Crystallographica Section D: Structural Biology*, *71*, 2519–2525.
119. Yamashita, K., Pan, D., Okuda, T., Sugahara, M., Kodan, A., Yamaguchi, T., et al. (2015). An isomorphous replacement method for efficient de novo phasing for serial femtosecond crystallography. *Scientific Reports*, *5*, 14017.
120. Colletier, J. P., Sliwa, M., Gallat, F. X., Sugahara, M., Guillon, V., Schirò, G., et al. (2016). Serial femtosecond crystallography and ultrafast absorption spectroscopy of the photoswitchable fluorescent protein IrisFP. *Journal of Physical Chemistry Letters*, *7*, 882–887.
121. Nakane, T., Hanashima, S., Suzuki, M., Saiki, H., Hayashi, T., Kakinouchi, K., et al. (2016). Membrane protein structure determination by SAD, SIR or SIRAS phasing in serial femtosecond crystallography using a novel iododetergent. *Proceedings of the National Academy of Sciences of the United States of America*, *113*, 13039–13044.
122. Edlund, P., Takala, H., Claesson, E., Henry, L., Dods, R., Lehtivuori, H., et al. (2016). The room temperature crystal structure of a bacterial phytochrome determined by serial femtosecond crystallography. *Scientific Reports*, *6*, 35279.
123. Masuda, T., Suzuki, M., Inoue, S., Song, C., Nakane, T., Nango, E., et al. (2017). Atomic resolution structure of serine protease proteinase K at ambient temperature. *Scientific Reports*, *7*, 45604.
124. Cheng, A., Hummel, B., Qiu, H., & Caffrey, M. (1998). A simple mechanical mixer for small viscous lipid-containing samples. *Chemistry and Physics of Lipids*, *95*, 11–21.
125. Barends, T. R. M., Foucar, L., Botha, S., Doak, R. B., Shoeman, R. L., Nass, K., et al. (2014). De novo protein crystal structure determination from X-ray free-electron laser data. *Nature*, *505*, 244–247.

126. Hunter, M. S., Yoon, C. H., DeMirici, H., Sierra, R. G., Dao, E. H., Ahmadi, R., et al. (2016). Selenium single-wavelength anomalous diffraction de novo phasing using an X-ray-free electron laser. *Nature Communications*, 7, 13388.
127. Nass, K., Meinhart, A., Barends, T. R., Foucar, L., Gorel, A., Aquila, A., et al. (2016). Protein structure determination by single-wavelength anomalous diffraction phasing of X-ray free-electron laser data. *IUCrJ*, 3, 180–191.
128. Thorn, A., & Sheldrick, G. M. (2011). ANODE: Anomalous and heavy-atom density calculation. *Journal of Applied Crystallography*, 44(6), 1285–1287.
129. Stellato, F., Oberthür, D., Liang, M., Bean, R., Gati, C., Yefanov, O., et al. (2014). Room-temperature macromolecular serial crystallography using synchrotron radiation. *IUCrJ*, 1, 204–212.
130. Weierstall, U. (2014). Liquid sample delivery techniques for serial femtosecond crystallography. *Philosophical Transactions of the Royal Society of London. Series B, Biological Sciences*, 369, 20130337.
131. Nakane, T., Joti, Y., Tono, K., Yabashi, M., Nango, E., Iwata, S., et al. (2016). Data processing pipeline for serial femtosecond crystallography at SACLA. *Journal of Applied Crystallography*, 49, 1035–1041.
132. Roessler, C. G., Agarwal, R., Allaire, M., Alonso-Mori, R., Andi, B., Bachega, J. F. R., et al. (2016). Acoustic injectors for drop-on-demand serial femtosecond crystallography. *Structure*, 24, 631–640. <https://doi.org/10.1016/j.str.2016.02.007>.
133. Beyerlein, K. R., Dierksmeyer, D., Mariani, V., Kuhn, M., Sarrou, I., Ottaviano, A., et al. (2017). Mix-and-diffuse serial synchrotron crystallography. *IUCrJ*, 4, 769–777. <https://doi.org/10.1107/S2052252517013124>.
134. Fuller, F. D., Gul, S., Chatterjee, R., Burgie, E. S., Young, I. D., Lebrette, H., et al. (2017). Drop-on-demand sample delivery for studying biocatalysts in action at X-ray free-electron lasers. *Nature Methods*, 14(4), 443–449.
135. Kok, B., Forbush, B., & McGloin, M. (1970). Cooperation of charges in photosynthetic O<sub>2</sub> evolution-I. A linear four step mechanism. *Photochemistry and Photobiology*, 11(6), 457–475. <https://doi.org/10.1111/j.1751-1097.1970.tb06017.x>.
136. Hunter, M. S., Segelke, B., Messerschmidt, M., Williams, G. J., Zatsepin, N. A., Barty, A., et al. (2014). Fixed-target protein serial microcrystallography with an x-ray free electron laser. *Scientific Reports*, 4, 6026.
137. Kimura, T., Joti, Y., Shibuya, A., Song, C., Kim, S., Tono, K., et al. (2014). Imaging live cell in micro-liquid enclosure by X-ray laser diffraction. *Nature Communications*, 5, 3052.
138. Murray, T. D., Lyubimov, A. Y., Ogata, C. M., Vo, H., Uervirojnangkoom, M., Brunger, A. T., et al. (2015). A high-transparency, micro-patternable chip for X-ray diffraction analysis of microcrystals under native growth conditions. *Acta Crystallographica Section D: Biological Crystallography*, 71, 1987–1997.
139. Cohen, A. E., Soltis, S. M., González, A., Aguila, L., Alonso-Mori, R., Barnes, C. O., et al. (2014). Goniometer-based femtosecond crystallography with X-ray free electron lasers. *Proceedings of the National Academy of Sciences of the United States of America*, 111, 17122–17127.
140. Roedig, P., Vartiainen, I., Duman, R., Panneerselvam, S., Stübe, N., Lorbeer, O., et al. (2015). A micro-patterned silicon chip as sample holder for macromolecular crystallography experiments with minimal background scattering. *Scientific Reports*, 5, 10451.
141. Zarrine-Afsar, A., Barends, T. R. M., Müller, C., Fuchs, M. R., Lomb, L., Schlichting, I., et al. (2012). Crystallography on a chip. *Acta Crystallographica Section D: Biological Crystallography*, 68, 321–323.
142. Mueller, C., Marx, A., Epp, S. W., Zhong, Y., Kuo, A., Balo, A. R., et al. (2015). Fixed target matrix for femtosecond time-resolved and in situ serial micro-crystallography. *Structural Dynamics*, 2, 054302.

143. Feld, G. K., Heymann, M., Benner, W. H., Pardini, T., Tsai, C. J., Boutet, S., et al. (2015). Low-Z polymer sample supports for fixed-target serial femtosecond X-ray crystallography. *Journal of Applied Crystallography*, 48(4), 1072–1079.
144. Lyubimov, A. Y., Murray, T. D., Koehl, A., Araci, I. E., Uervirojnangkoorn, M., Zeldin, O. B., et al. (2015). Capture and X-ray diffraction studies of protein microcrystals in a microfluidic trap array. *Acta Crystallographica Section D*, 71(4), 928–940.
145. Roedig, P., Ginn, H. M., Pakendorf, T., Sutton, G., Harlos, K., Walter, T. S., et al. (2017). High-speed fixed-target serial virus crystallography. *Nature Methods*, 14, 805. <https://doi.org/10.1038/nmeth.4335>.
146. Opara, N., Martiel, I., Arnold, S. A., Braun, T., Stahlberg, H., Makita, M., et al. (2017). Direct protein crystallization on ultrathin membranes for diffraction measurements at X-ray free-electron lasers. *Journal of Applied Crystallography*, 50, 909–918.
147. Meents, A., Gutmann, S., Wagner, A., & Schulze-Briese, C. (2009). Origin and temperature dependence of radiation damage in biological samples at cryogenic temperatures. *Proceedings of the National Academy of Sciences*, 107(3), 1094–1099. <https://doi.org/10.1073/pnas.0905481107>.
148. Owen, R. L., Rudiño-Piñera, E., & Garman, E. F. (2006). Experimental determination of the radiation dose limit for cryocooled protein crystals. *Proc Natl Acad Sci USA*, 103(13), 4912–4917.
149. Suga, M., Akita, F., Hirata, K., Ueno, G., Murakami, H., Nakajima, Y., et al. (2015). Native structure of photosystem II at 1.95 Å resolution viewed by femtosecond X-ray pulses. *Nature*, 517(7532), 99–103. <https://doi.org/10.1038/nature13991>.
150. Fraser, J. S., van den Bedemb, H., Samelsova, A. J., Langa, P. T., Holton, J. M., et al. (2011). *Proceedings of the National Academy of Sciences of the United States of America*, 108(39), 16247–16252. <https://doi.org/10.1073/pnas.1111325108>.
151. Coquelle, N., Brewster, A. S., Kapp, U., Shilova, A., Weinhausen, B., Burghammer, M., et al. (2015). Raster-scanning serial protein crystallography using micro- and nano-focused synchrotron beams. *Acta Crystallographica Section D: Biological Crystallography*, 71(Pt 5), 1184–1196. <https://doi.org/10.1107/S1399004715004514> Epub 2015 Apr 25.
152. Sui, S., Wang, Y., Kolewe, K. W., Srajer, V., Henning, R., Schiffman, J. D., et al. (2016). Graphene-based microfluidics for serial crystallography. *Lab on a Chip*, 16(16), 3082–3096. <https://doi.org/10.1039/c6lc00451b>.
153. Kiefersauer, R., Than, M. E., Dobbek, H., Gremer, L., Meler, M., Strobl, S., et al. (2000). *Journal of Applied Crystallography*, 33, 1223–1230.
154. Sanchez Weatherby, J., Bowler, M. W., Huet, J., Gobbo, A., Felisaz, F., Lavault, B., et al. (2009). Improving diffraction by humidity control: A novel device compatible with X-ray beamlines. *Acta Crystallographica. Section D, Biological Crystallography*, 65, 1237–1246.
155. Roedig, P., Duman, R., Sanchez-Weatherby, J., Vartiainen, I., Burkhardt, A., Warmer, M., et al. (2016). Room-temperature macromolecular crystallography using a micro-patterned silicon chip with minimal background scattering. *Journal of Applied Crystallography*, 49, 968–975.
156. Meents, A., Wiedorn, M. O., Srajer, V., Henning, R., Sarrou, I., Bergtholdt, J., et al. (2017). Pink beam serial crystallography. *Nature Communications*, 8, 1281. <https://doi.org/10.1038/s41467-017-01417-3>.
157. Sherrell, D. A., Foster, A. J., Hudson, L., Nutter, B., O’Hea, J., Nelson, S., et al. (2015). A modular and compact portable mini-endstation for high-precision, high-speed fixed target serial crystallography at FEL and synchrotron sources. *Journal of Synchrotron Radiation*, 22, 1372–1378.
158. Owen, R. L., Axford, D., Sherrell, D. A., Kuo, A., Ernst, O. P., Schulz, E. C., et al. (2017). Low-dose fixed-target serial synchrotron crystallography. *Acta Crystallographica Section D: Biological Crystallography*, 73, 373–378.
159. Abdallah, B. G., Zatsepin, N. a., Roy-Chowdhury, S., Coe, J., Conrad, C. E., Dörner, K., et al. (2015). Microfluidic sorting of protein nanocrystals by size for X-ray free-electron laser diffraction. *Structural Dynamics*, 2, 041719. <https://doi.org/10.1063/1.4928688>.

160. Koralek, J. D., Kim, J. B., Brůža, P., Curry, C. B., Chen, Z., Bechtel, H. A., et al. (2018). Generation and characterization of ultrathin free-flowing liquid sheets. *Nature Communications*, 9(1), 1–8. <https://doi.org/10.1038/s41467-018-03696-w>.
161. Wiedorn, M. O., Awel, S., Morgan, A. J., Ayyer, K., Gevorkov, Y., Fleckenstein, H., et al. (2018). Rapid sample delivery for megahertz serial crystallography at X-ray FELs. *IUCrJ*, 5(5), 574–584.